NUMERICAL METHODS FOR ROTATING COMPACT OBJECTS IN MODIFIED GRAVITY THEORIES

by

Andrew Patrick Kyung Sullivan

A dissertation submitted in partial fulfillment
of the requirements for the degree

of

Doctor of Philosophy

in

Physics

MONTANA STATE UNIVERSITY
Bozeman, Montana

April 2020

DEDICATION

I dedicate this to my mom, whose trips to the local library to checkout science books as a child were an enormous inspiration.

ACKNOWLEDGEMENTS

I would like to thank my advisor, Dr. Nicolás Yunes whose support and mentorship has been invaluable. Thank you for always pushing me to be the best researcher I can be. I would like to thank the members of my committee, especially my co-chair Dr. Neil Cornish for the constructive comments on my work. I would like to thank Margaret Jarrett of the MSU Physics department for her help and support. I would like to thank my friends who have supported me along the way especially Dimitry Ayzenberg whose conversations and company helped during the early years of my graduate career. Finally I would like to thank my family; my parents, my brother, and sister whose continual support has been immeasurable.

TABLE OF CONTENTS

TABLE OF CONTENTS – CONTINUED

TABLE OF CONTENTS – CONTINUED

LIST OF TABLES

LIST OF FIGURES

LIST OF FIGURES – CONTINUED

Figure Page

LIST OF FIGURES – CONTINUED

Figure Page

LIST OF FIGURES – CONTINUED

LIST OF FIGURES – CONTINUED

Figure Page

LIST OF FIGURES – CONTINUED

Figure Page

LIST OF FIGURES – CONTINUED

LIST OF FIGURES – CONTINUED

Figure Page

LIST OF FIGURES – CONTINUED

Figure Page

LIST OF FIGURES – CONTINUED

Figure Page

LIST OF FIGURES – CONTINUED

Figure Page

LIST OF FIGURES – CONTINUED

ABSTRACT

Detailed observations of phenomena involving compact objects will provide us with a new avenue to test general relativity in the strong field regime. So as to not bias our analysis of these new experiments, we require knowledge of the spacetimes around these objects both within and beyond general relativity. Here I will describe work that applies two specific methods to solve the modified Einstein's equations that describe the exotic spacetimes beyond general relativity for neutron stars and black holes. The first method is a fourth-order Runge-Kutta-Fehlberg ordinary differential equation numerical integrator method. The second method is a relaxed Newton-Raphson method applied to a system of nonlinear partial differential equations. Using these methods, we solve for the spacetimes of slowly rotating neutron stars in massive bigravity and rotating black holes in scalar Gauss-Bonnet gravity in a theory independent methodology. We validate our numerical methods by applying them to compact objects in general relativity and using them to recover known perturbative solutions. We can then compare the fully nonlinear solutions to these perturbative solutions and comment on their differences. We then use these numerical solutions to calculate the physical observables of these systems and finally construct analytic fitted models that can be used in rapid computation methods that future experiments may use to constrain the free parameters in these theories.

1

INTRODUCTION

Motivation

Einstein's theory of relativity has been one of the most important breakthroughs of understanding the natural world in the modern age. It has changed our understanding of the fundamental nature of absolute space and time and forced us to reasses our epistemological knowledge of geometry [49], namely how we treat the theoretical concepts of geometry with the physical world around us.

Einstein's theory provides a beautiful reinterpretation of motion in the presence of a gravitating body via a force into motion through a curved spacetime and has thus far passed all tests in the weak-field regime [75, 97]. Unfortunately, even given the stellar success of Einstein's theory of general relativity, there are still many pressing questions that remain unanswered. The late time accelerated expansion of the universe [32] and the failed attempts at quantization [28] has turned our attention to modifying general relativity.

Unsurprisingly, modifying general relativity typically increases the complexity of the field equations to such a degree that calculation of physically observable predictions becomes incredibly difficult. Furthermore, the wide range of the tunable coupling parameters of these theories can sometimes mask nonlinear effects when making simplifying assumptions to aid in our calculations such as making weak-coupling approximations. Thus, the need arises to develop a theory independent method to calculate physically observable predictions in these modified gravity theories.

The two attempts to modify general relativity that are relevant to this

dissertation are massive bigravity and scalar Gauss-Bonnet gravity. Massive bigravity is a generalization of massive gravity where the graviton is endowed with a mass. This is done by introducing a second fixed auxiliary metric that interacts with our physical metric. By giving this auxiliary metric dynamics, the additional degree of freedom produces a second graviton and has been aptly named massive bigravity. The second attempt relevant to this thesis is by treating heterotic string theory [50] as an effective field theory [28]. This treatment results in a theory of gravity coupled via a massless scalar field (the dilaton) to the gravitational sector with the Gauss-Bonnet invariant and is commonly referred to as scalar Gauss-Bonnet gravity.

Neutron Stars in Massive Bigravity

Binary systems of pulsars provide a useful laboratory to test general relativity. The long term observations of radio pulses from these systems encode information about the post-Keplerian parameters that characterize the general relativistic gravitational effects on the binary such as the advance of the periastron and the rate of change of the orbital period [89]. By constructing a timing model, it is possible to extract these parameters and relate them to the individual masses of the pulsars [79]. If we then measure at least two of these parameters, we can estimate these masses very precisely; for example, the primary pulsar PSR J0737-3039A has an estimated mass of $(1.337 \pm 0.0037)M_{\odot}$ [65]. Furthermore, future observations of binary pulsar systems may allow for a measurement of the moment of inertia of the primary pulsar to 10% [62]. In a modified gravity theory, these post-Keplerian parameters are also dependent on the coupling constants of the theory, so a measurement of more than two post-Keplerian parameters can be used to place constraints on these parameters [37].

It is also possible to infer the radius of neutron stars from measurements of quiescent low mass X-ray binaries [51]. Measurements of the X-ray spectra of these

systems in combination with the post-Keplerian parameters of the binary can provide an estimate of the neutron star radius which combined with the mass can place constraints on allowed equations of state in the mass-radius relations. Additionally, the recent measurement of the mass and radius of PSR J0030+0451 [70] can provide an alternative method to place these constraints.

Our goal in this work is to take the first step towards the extension of these analyses to massive bigravity by numerically integrating slowly rotating neutron star solutions and producing mass-radius and moment of inertia-mass relations using realistic neutron star equations of state. These results, when combined with a future analysis of the post-Keplerian parameters in massive bigravity could be used to place constraints on the graviton mass and the relative strength of the gravitational constants.

To produce slowly rotating neutron star solutions in massive bigravity, we use a perturbative expansion in slow rotation. To simplify the field equations, we assume the neutron star is isolated and can be modeled as a perfect fluid with a barotropic equation of state obtained numerically from nuclear physics calculations. We have chosen to focus only on equations of state that allow for neutron stars with a maximum mass above the observed PSR J1614-2230 limit of $2.01 M_\odot$ [11] [1] in GR.

Furthermore, we require both the physical and auxiliary metric to be stationary, axisymmetric, and asymptotically flat and assume that the product of the angular velocity and the radius of the neutron star is much smaller than unity. This assumption allows us to expand the modified Tolman-Oppenheimer-Volkoff (TOV) equations of stellar structure about small rotation and the linearized equations become separable. This process gives us two sets of ordinary differential equations, one set to zeroth-order in rotation which models the star in spherical symmetry, and one set

[1] This limit has since been improved to $1.91 M_\odot$ [13] with followup observations.

to first-order in rotation. To solve these equations, we use an adaptive Runge-Kutta-Fehlberg method [47] to fourth order with a fifth order error estimator.

Before numerical integration, we need to determine our boundary conditions through an asymptotic analysis of the field equations at the stellar core and at spatial infinity. By matching order-by-order, we find power series solutions in these two regions where we must specify one free parameter, the central density of the star, which effectively determines the final mass of the star. During this matching, we obtain four additional parameters, two at the core and two at infinity that must be "shot for" by requiring continuity and differentiability of the solution on the stellar surface. The shooting method is as follows:

1. Choose a central density for the neutron star ρ_0.

2. Choose a set of values for the shooting parameters at the core which specifies the initial conditions for numerical integration.

3. Integrate outwards using the Runge-Kutta-Fehlberg method from the core until the pressure of the star becomes sufficiently small that we can define the surface of the star and set the pressure to zero.

4. Choose a set of shooting parameters at infinity to specify the initial conditions for numerical integration.

5. Integrate inwards from infinity until we reach the surface of the star determined from Step 3. Check if the solution is sufficiently continuous and differentiable on the surface. If it is not, we estimate new values for the four shooting parameters using a 4-dimensional Newton-Raphson method and repeat Steps 2-5.

6. Once the solution is sufficiently continuous and differentiable on the stellar surface, we repeat the process from Step 1 upon choosing a different central density.

This gives us a range of spherically symmetric neutron stars with a given equation of state. We then use these solutions to numerically integrate the first-order field equations in an identical manner where our free parameter is now the angular velocity of the star which is assumed to be uniform and we have only 1 shooting parameter that is determined using the same method.

From these solutions, we calculate physical observables like the mass and angular momentum of each star. These are the properties that would be extracted from an analysis of post-Keplerian parameters of binary pulsar systems in massive bigravity. We then create mass-radius and moment of inertia-mass relations for different coupling strengths and different equations of state and also find that the modifications to the mass-radius relation are highly degenerate with the neutron star equation of state though we find evidence that these degeneracies may be resolved by constructing approximate universal relations in massive bigravity which would require an extended calculation to second order in rotation [100, 101, 102].

In summary, we find numerical solutions to neutron stars in spherical symmetry and to first order in slow rotation in massive bigravity. These are obtained through a perturbative expansion in rotation assuming the product of the angular velocity and the radius are much smaller than unity to separate the differential equations. We then analyze the field equations near the core of the star and at spatial infinity to determine initial conditions for numerical integration using an adaptive Runge-Kutta-Fehlberg method and a 4-dimensional shooting method to fix the remaining parameters. We then construct mass-radius and moment of inertia-mass relations for various realistic equations of state and coupling parameters. These solutions lay the

foundation for further experiments to constrain the coupling parameters in massive bigravity.

Black holes in scalar Gauss-Bonnet: Spherical Symmetry

Recently, the Event Horizon Telescope released the first horizon scale pictures of the supermassive black hole at the center of the M87 galaxy that presents a new laboratory to test the strong field regime of general relativity. Specifically, the image taken depends on the location of unstable photon orbits called the photon sphere or light ring around the black hole. In a modified gravity theory, the location of the light ring will shift depending on the coupling constant. Unfortunately, recent work has shown that future measurements of the black hole shadow are unlikely be able to test quadratic gravity theories [16]. Fortunately, the metric of a black hole in modified gravity can also be used to calculate other astrophysical observables, such as electromagnetic emission of accretion disks around black holes [8], or quasinormal modes of black hole mergers [25].

The goal of the second half of my work is to develop a computational infrastructure to find black hole solutions in an arbitrary modified theory of gravity and to produce analytic fitting functions that allow realistic data analysis investigations with Bayesian methods using the solutions. The algorithm presented in this section applies to spherically symmetric scenarios while we extend it to axial symmetry in the next section.

The typical approach to solving a set of ordinary differential equations is to use a Runge-Kutta-Fehlberg method as described in the previous section where one typically begins at some known initial condition and integrates along one dimension, one discrete step at a time until one covers the whole domain. In contrast, a typical procedure to solve a set of nonlinear, coupled, partial differential equations is to apply

a finite difference method which instead discretizes the entire domain simultaneously to approximate the differential operators at each grid point and reduce the system of differential equations on the entire domain as a single linear system of equations that can be solved algebraically. The main difference in the approach of these methods is that the Runge-Kutta-Fehlberg method acts one step at a time, usually requiring a set of initial conditions that specify the function and its derivatives at an initial point while the finite difference method acts within the entire domain and uses a root finding algorithm to relax to the solution with given boundary conditions. In the above section, we used a Runge-Kutta-Fehlberg method to "shoot" for the numerical solution of a neutron star between the stellar core and spatial infinity. In this section we use a finite difference method to iteratively solve for the general solution of a black hole with minimal assumptions on a particular modified theory of gravity.

The basic problem we wish to solve are the modified field equations for the exterior region of a stationary black hole in axial symmetry. To do this, we will formulaically discretize each differential operator of the nonlinear elliptic partial differential equations using a Newton interpolation polynomial on the entire exterior region of the black hole. This discretization introduces a residual and a finite difference error that must be minimized and controlled respectively. To minimize the residual, we use a relaxed Newton-Raphson method to iteratively converge on the desired solution to a specified error tolerance. The Newton-Raphson method will require the calculation of the Jacobian of our discretized system of equations which is done analytically using symbolic manipulation software and then exported into numerically evaluable expressions in the C programming language. We furthermore control the discretization errors using a similar minimization procedure by allowing for an adaptive mesh refinement in our domain.

Our computational infrastructure is general enough that we need only specify

that an event horizon exists and that our spacetime is asympotically flat. To validate and develop this infrastructure we apply it first to static black holes in scalar Gauss-Bonnet gravity in spherical symmetry. We explored the comparison between the two commonly used coupling functions between the massless dilaton and the Gauss-Bonnet invariant: a linear coupling referred here as linear scalar Gauss-Bonnet (linear sGB) and an exponential coupling referred here as Einstein-dilaton-Gauss-Bonnet (EdGB) gravity. We then compare these solutions to known perturbative analytic solutions found using the weak-coupling approximations.

Using the solutions, we then calculate various physical properties of these spacetimes. We calculate the ADM mass and scalar charge of the black holes as well as the location of the innermost stable circular orbit and the light ring. We find that the linear sGB solutions agree very well with the weak-coupling perturbative solutions as expected and that there are large deviations when compared to the EdGB solutions.

We then use these solutions to develop analytic fitting functions constructed through polynomials of the compactified coordinate inspired by the analytic perturbative solution. We verify that the analytic fitting functions reproduce the computed physical observables up to the numerical error.

In summary, we lay the foundations for a computational infrastructure to solve for static, spherically symmetric spacetimes in an arbitrary modified theory of gravity using a relaxed Newton-Raphson finite difference discretization method. Through analytic treatment of the discretized differential equations, we can use this infrastructure to study solutions to a very wide class of modified theories of gravity. Here we focus on black holes in scalar Gauss-Bonnet gravity and we find and compare solutions using various perturbative expansions of the modified Lagrangian. From these solutions we generate analytical fitting functions and use both to calculate and

compare the physical observables of these spacetimes.

Black holes in scalar Gauss-Bonnet: Axial Symmetry

Perturbed black hole spacetimes are intrinsically dissipative due to the emission of gravitational waves. The excited quasinormal modes (QNMs) carry important information about the structure of the black holes as their decay is independent of the source of the perturbation and can be useful laboratories to test general relativity. By solving the equations governing linearized perturbations around the black hole spacetime, one can calculate the expected QNM spectra. In GR, work has been done in spherical symmetry [76] and in the rotating case [91] to obtain the set of differential equations that describe the black hole QNMs but there are no closed form analytic solutions [61]. Recently there has been an effort to extend this analysis to QNMS in modified gravity in spherical symmetry [31, 67] and in axial symmetry [105].

Our goal is to extend the previous numerical infrastructure to rotating black hole solutions in axial symmetry in an effort to provide numerical and analytic fitted models to use as backgrounds to calculate the QNM spectrum of black holes in these modified theories.

The extension of our numerical infrastructure is relatively straightforward. We must now discretize our grid in two dimensions using the same Newton interpolation formula. Importantly, the additional dimension introduces a second discretization error that must be controlled in an identical manner to the error along the original dimension. Mixed partial derivatives are treated by defining a new auxiliary variable that is substituted into each mixed derivative operator and define an additional field equation whose residual is simultaneously minimized with the rest of the differential system. The resulting system of linear equations after discretization is minimized with the same relaxed Newton-Raphson method. We validate this infrastructure by

recovering the Kerr metric in GR as well as numerically solving rotating black holes in the weak-coupling limit without a small rotation approximation. We then compare these solutions to the full nonlinear solutions.

From the numerical solutions, we ccalculate physical observables such as the ADM mass and angular momentum of the black holes for different dimensionless spins and coupling. We find that scalar charge for increasing coupling values is suppressed for larger spins which matches a qualitative effect observed in analytic perturbative solutions in small coupling and rotation. We also again find very good agreement between the perturbative and linear sGB solutions while there are large deviations in the EdGB solutions. We then use these solutions to produce analytic fitting functions and again verify that their calculated physical observables match those from the exact numerical solution.

In summary, we extend our previous numerical infrastructure to find rotating black holes in an arbitrary modified theory of gravity and validated them in GR and rotating, weak-coupling perturbative solutions. We then compared the nonlinear solutions and their calculated physical observables and produced analytical fitted models from the numerical solutions.

Summary

The first aspect of my thesis work uses a finite difference method to solve for slowly rotating neutron stars in massive bigravity by numerically integrating the modified equations of stellar structure in spherical symmetry and to first order in slow rotation. This can help us place constraints on the coupling parameters of the theory with future analysis of the post-Keplerian parameters of binary pulsar systems.

The second aspect of my thesis work develops a numerical infrastructure to solve stationary, axially symmetric black hole spacetimes in an arbitrary modified

theory of gravity. We have done this using a finite difference method to discretize the modified field equations and a relaxed Newton-Raphson method to minimize the resulting residual and converge to the desired solution. We then calculate physical observables from the numerical solutions and produce analytic fitted models that can be used in future studies to calculate the quasinormal ringdown modes of perturbed black holes in these spacetimes.

The outline of this thesis is as follows: Chapter 2 detail my work in the finite difference method solution to slowly rotating neutron stars in massive bigravity. Chapter 3 describes the foundations of the computational infrastructure to find black hole solutions in an arbitrary modified theory of gravity and applies them to static, spherically symmetric black holes in scalar Gauss-Bonnet gravity. Chapter 4 extends the previous work to stationary black holes in axial symmetry. Lastly, in Chapter 5, I conclude the thesis by discussing the overall impact of my work and end with future directions that can be taken.

12

SLOWLY-ROTATING NEUTRON STARS IN MASSIVE BIGRAVITY

Contribution of Authors and Co-Authors

Manuscript in Chapter 2

Author: Andrew Sullivan

Contributions: Performed mathematical analysis of problem, compared results, and wrote the manuscript.

Co-Author: Nicolás Yunes

Contributions: Thought of the problem, helped find errors in the code, helped interpret results, discussed implications, and edited manuscripts.

Manuscript Information Page

Andrew Sullivan and Nicolás Yunes

Classical and Quantum Gravity

Status of Manuscript:

_____Prepared for submission to a peer-reviewed journal

_____Officially submitted to a peer-reviewed journal

_____Accepted by a peer-reviewed journal

__X__Published in a peer-reviewed journal

Published by: Classical and Quantum Gravity

In Volume 35, Issue 4, 15 January 2018

DOI: 10.1088/1361-6382/aaa3ab

Abstract

We study slowly-rotating neutron stars in ghost-free massive bigravity. This theory modifies General Relativity by introducing a second, auxiliary but dynamical tensor field that couples to matter through the physical metric tensor through non-linear interactions. We expand the field equations to linear order in slow rotation and numerically construct solutions in the interior and exterior of the star with a set of realistic equations of state. We calculate the physical mass function with respect to observer radius and find that, unlike in General Relativity, this function does not remain constant outside the star; rather, it asymptotes to a constant a distance away from the surface, whose magnitude is controlled by the ratio of gravitational constants. The Vainshtein-like radius at which the physical and auxiliary mass functions asymptote to a constant is controlled by the graviton mass scaling parameter, and outside this radius, bigravity modifications are suppressed. We also calculate the frame-dragging metric function and find that bigravity modifications are typically small in the entire range of coupling parameters explored. We finally calculate both the mass-radius and the moment of inertia-mass relations for a wide range of coupling parameters and find that both the graviton mass scaling parameter and the ratio of the gravitational constants introduce large modifications to both. These results could be used to place future constraints on bigravity with electromagnetic and gravitational-wave observations of isolated and binary neutron stars.

Introduction

In recent years, the exploration of the accelerated expansion of the universe has led to a renewed interest in modified gravity theories with a massive graviton. It was previously thought that any theory with a massive graviton would introduce an

unphysical ghost-like scalar propagating mode, until it was shown in 2009 [41, 43] that the ghost mode could be removed with a properly generalized action. In the resulting theory (dRGT or massive gravity), a second metric, taken to be flat and non-dynamical, was introduced in order to generate the non-trivial higher order terms in the action that were required to remove the ghost mode. In 2011, it was shown [56] that the dRGT theory could be generalized by removing the requirement that the auxiliary metric be non-dynamical. The resulting theory, aptly named massive bigravity or bimetric gravity [82], is one in which there are two metrics, a physical one that couples to matter and an auxiliary but dynamical one that couples directly to the metric.

Most of the work thus far has been focused on cosmology in massive gravity and massive bigravity. Shortly after this renewed interest it was found [36] that there are no spatially flat or closed Friedman-Lemaître-Robertson-Walker (FLRW) solutions in massive gravity due to a modified Hamiltonian constraint. Although there are cosmological solutions that can explain the present and past observations of the evolution of the universe, many of these solutions suffer from a fine-tuning problem, and many of these exact solutions have been found to be unstable. There have been multiple avenues to address these issues, one of which was to add additional degrees of freedom to the theory by allowing the auxiliary metric in massive gravity to become dynamical, which promoted the initial interest in bimetric gravity. Adding dynamics to the auxiliary metric places it on equal footing with the primary metric and the gravitational force in each metric is mediated by its own graviton, one being massless and one being massive. It was subsequently shown that massive bigravity does admit spatially open, closed, and flat cosmological solutions [94], although cosmology in this theory is still very much an ongoing area of research.

The existence and stability of black holes in massive bigravity is also an active

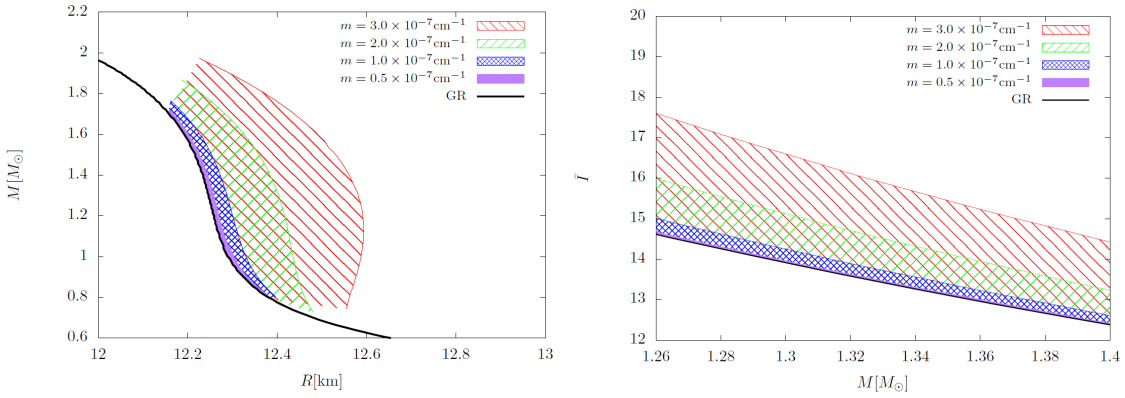

(a) Mass-radius relation

(b) Moment of inertia-mass relation

Figure 2.1: The mass-radius relation (left) and the moment of inertia-mass relation (right) using three realistic equations of state with varying m and all other coupling parameters fixed. The mass of the star M is obtained from the mass function of the physical metric evaluated at the stellar surface defined by radius R. The dimensionless moment of inertia is defined via $\bar{I} = I/M^3$, where $I \equiv |\vec{J}|/\Omega$, with $\vec{J}$ the spin angular momentum and Ω the angular frequency of rotation. The shaded regions represent variability of the relations with the coupling parameter m from $m \in [0, 3.0 \times 10^{-7}\mathrm{cm}^{-1}]$, while keeping all others fixed to $c_3 = 0.48$, $c_4 = 1.71$, and $\eta = \pi/4$, with the solid black lines representing the GR limit, and the different colors representing different equations of state. Observe that the relations smoothly approach the GR relation in the $m \to 0$ limit. Observe also that as the mass of the star increases, the GR modification in the moment of inertia decreases, because the interior matter content of the star increasingly dominates the interaction with the auxiliary metric.

area of research. The first spherically-symmetric, vacuum solutions in ghost-free massive bigravity emerged in 2011 [34] and 2012 [95]. These solutions were organized into two classes: bidiagonal (both metrics are diagonal) and non-bidiagonal (the physical metric is diagonal while the auxiliary one is not) [34]. For the bidiagonal class, perturbative solutions around a Minkowski background were found in [95], as well as full non-linear solutions in [26] shortly after. The simplest case of bidiagonal vacuum solutions where both metrics are Schwarzschild-like is linearly unstable [17]. For the non-bidiagonal class, solutions have been found analytically [34] and they have been shown to be stable [19]. The first study of axially-symmetric vacuum solutions showed the existence of rotating black holes [18] and asymptotically de-Sitter rotating black holes [14]. The simplest case of the former, where both metrics are Kerr-like, is linearly unstable [27].

The first treatment of non-rotating, spherically symmetric stars in massive bigravity was completed assuming a uniform density distribution in 2012 [95] and 2015 [46]. These solutions successfully showed how the Vainshtein mechanism acts to recover GR [95], which was then used to place constraints on the ratio of gravitational constants and the Compton wavelength of the graviton [46]. Shortly after, non-rotating, spherically symmetric stars with matter satisfying a polytropic equation of state were found [12], and were organized into two main classes characterized by the choice of coupling constants. The first class does not allow for regular neutron star solutions above a certain maximum mass, which is much smaller than that in GR. Given that more massive neutron stars have already been observed [11, 64], this class of solutions is observationally ruled out. The second class successfully recovers GR through the Vainshtein mechanism in a range of coupling parameters, thus avoiding this observational constraint. In this paper, we extend these analyses in two main ways: (i) we consider "realistic" nuclear equations of state, and (ii) we extend the

analysis to slowly-rotating neutron stars.

We begin with the Hassan-Rosen action in massive bigravity [56], which depends on two metrics: a "physical" g-metric that couples directly to the matter sector and an auxiliary, dynamical f-metric that couples directly only to the g-metric. The gravitational action is then simply two copies of the Einstein-Hilbert action (one for each metric), plus a set of metric interaction terms that couple the two metrics together. The couplings between metrics and between the g-metric and matter is controlled by various coupling parameters, of which only m, c_3, c_4, and η will be relevant here. The parameter η characterizes the relative strength of the gravitational constants (G and $\mathcal{G}$), which multiply the Einstein-Hilbert terms, and it is bounded by $\eta \in [0, \frac{\pi}{2}]$. The parameter m quantifies the overall strength of all metric interaction terms in the action, and it is closely related to the mass of the graviton in the theory. The parameters c_3 and c_4 quantify the relative strength of the high-order interaction terms in the action, and are scaled to be of order unity. Section 2 provides a more detailed summary of the theory.

We here study slowly-rotating neutron stars in isolation, and thus, we can simplify the field equations significantly. First, we require the physical and auxiliary metrics to be both stationary and axisymmetric with asymptotically flat boundary conditions at spatial infinity. Second, we model the matter stress-energy tensor as a perfect fluid with a barotropic equation of state, obtained numerically from nuclear physics calculations; in particular, we consider the Akmal-Pandharipande-Ravenhall (APR) [9], Lattimer-Swesty (LS220) [63], and Shen et al. [85] equations of state. Third, we solve the field equations in an expansion about small rotation, assuming that the product of the angular velocity and the radius of the star is much smaller than unity. Finally, we simplify the field equations using a tetrad basis decomposition [95] that allows us to obtain modified Tolman-Oppenheimer-Volkoff (TOV) equations at

zeroth-order in rotation, and a set of field equations at first-order in rotation.

The numerical evolution of these equations requires that we choose boundary conditions carefully. We carry out a local analysis of the field equations at the stellar core and at spatial infinity, which allows us to find power-series solutions in these two regimes. We then use these power-series expressions as boundary conditions for the numerical evolution of the field equations order by order in a slow-rotation expansion. We use a shooting method to match all metric functions and their first derivatives at the surface of the star, defined as the radius where the pressure vanishes, thus ensuring continuity and differentiability at the surface.

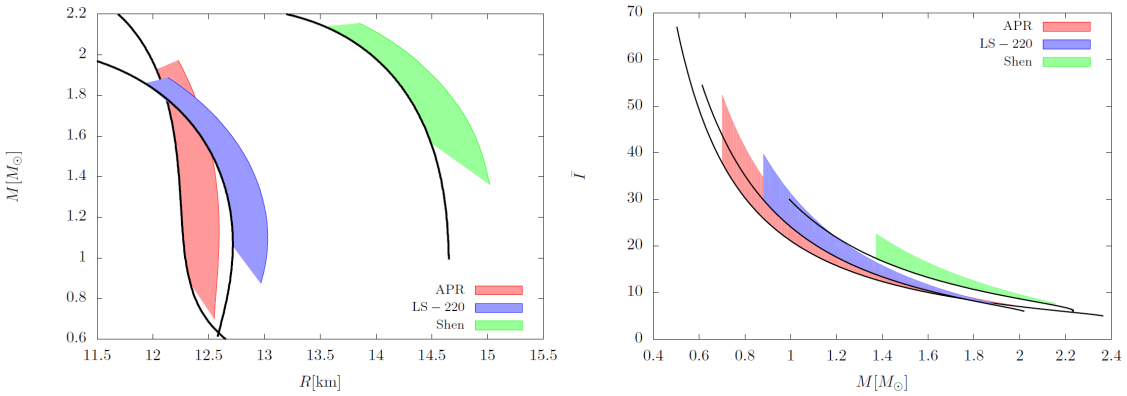

(a) Mass-radius relation

(b) Moment of inertia-mass relation

Figure 2.2: Mass-radius (left) and moment of inertia-mass (right) relations for the APR equation of state for a set of fixed m and varying $\eta \in (0, \pi/2)$. The lower bound on each region corresponds to the GR limit with $\eta = \pi/2$, while the upper bound corresponds to the $\eta = 0$ case and it is determined by the value of m. Observe that the fixed value of m controls the maximum range of variability of these relations.

From the zeroth-order modified TOV equations, we numerically generate spherically-symmetric stellar solutions with which we can calculate observables, such as the mass-radius relations shown in the left panel of Fig. 2.1. As expected, the modified mass-radius relation in bigravity is highly degenerate with the equation of

state, and it has a smooth transition to GR in both the $m \to 0$ and $\eta \to \pi/2$ limit. From the first-order field equations, we numerically generate the linear-in-spin corrections to the metric with which we can calculate other observables, such as the moment-of-inertia-mass curve shown in the right panel of Fig. 2.1. As expected, the modified moment of inertia also has a smooth limit to GR, but in this case notice that as the moment of inertia increases, all curves tend to the GR limit. This is because as the central density increases, the mass increases and the matter interactions dominate over interactions between the auxiliary and physical metrics.

The relations discussed above do not display a very interesting result in massive bigravity for neutron stars: the physical mass function outside the star does not remain constant as expected in GR, but rather it decreases due to interactions with the auxiliary metric (a type of Vainshtein screening). Inside the star, the physical mass m_g increases much more rapidly than the auxiliary mass m_f due to the explicit matter coupling to the physical metric. Outside the star, although the energy-density vanishes, the interaction between the physical and the auxiliary metrics causes the physical mass to decrease and asymptote to a constant that depends on the coupling parameter η. When $\eta = \pi/4$, both gravitational constants have equal strength and the asymptotic physical mass is exactly half of the Arnowit-Deser-Misner (ADM) mass in GR. As $\eta \to \pi/2$, the asymptotic physical mass becomes constant in the exterior spacetime, while as $\eta \to 0$, the asymptotic physical mass decreases until the neutron star mass is entirely screened by the auxiliary metric.

This behavior of the physical mass with η means there are now two distinct limits to GR in this theory, when $m \to 0$ with η fixed and when $\eta \to \pi/2$ with m fixed, as shown in Fig. 2.2. The left panel of this figure presents the mass-radius relation, while the right panel shows the moment of inertia-mass relation, for a single equation of state but varying both m and η. In the $\eta \to 0$ case, the neutron star

mass is entirely screened by the auxiliary metric, and as m increases, the $\eta \to 0$ curve deviates more and more from GR. On the other hand, even for large values of m, when $\eta \sim \pi/2$, one still recovers GR.

We also explored the effects of the two remaining coupling parameters, c_3 and c_4 on the moment of inertia and the metric profiles inside and outside the star. We find that the moment of inertia is not substantially affected by these parameters within the range of values we considered, which are restricted by analytical considerations of scattering amplitudes in massive gravity [33]. Unlike m and η, the primary effect of both c_3 and c_4 appears to be to broaden the I-M curve at each m and η value. As the mass scaling parameter m increases, this broadening effect also increases. The weaker influence of c_3 and c_4 is due to the manner in which these parameters appear in the action. Since they couple to the third and fourth order terms of the action respectively, their effect is inherently subdominant to the leading, second-order term scaled by m and η, unless all interaction terms are non-linearly relevant. The coupling parameters c_3 and c_4 also seem to significantly affect the auxiliary radial coordinate, U, and the auxiliary f_{tt} metric element profiles inside the star; the effect outside the star almost entirely vanishes, since there the auxiliary metric interactions dominate. This supports the conclusion that (c_3, c_4) have a mild effect on the moment of inertia, because the region where they have the largest effect is the region where they are subdominant to matter interactions.

The remainder of this paper presents the details of the calculations and results presented above and it is organized as follows. In Sec. 2, we outline the basics of massive bigravity and introduce the notation we use throughout the paper. In Sec. 2, we present the metric ansatz and the stress-energy tensor we employ, as well as the method to determine the interaction tensor in order to derive the modified TOV equations in massive bigravity. In Sec. 2, we outline the asymptotic expansions used

to obtain the boundary conditions for the numerical integrations, and describe the numerical algorithm we used to solve the modified field equations at both zeroth-order and first-order in spin. In Sec. 2, we describe why the results obtained here are important and how one could use them to compare against observations of isolated and double binary pulsar systems. Throughout this paper, we will use the following conventions: Greek letters denote spacetime indices; capitalized Latin letters denote tetrad indices; both metrics have the spacetime signature $(-,+,+,+)$; unless otherwise stated, geometric units where $G = c = 1$.

Massive Bigravity

The ghost-free action of massive bigravity given by Hassan and Rosen [57] in natural units ($c = \hbar = 1$) is

$$S = M_g^2 \int R\sqrt{-g}\, d^4x + M_f^2 \int \mathcal{R}\sqrt{-f}\, d^4x + 2m^2 M_{\rm eff}^2 \int \mathcal{L}_{\rm int}\sqrt{-g}\, d^4x + S_{\rm mat}[g_{\mu\nu}], \tag{2.1}$$

where R and $\mathcal{R}$ are the Ricci scalars associated with the physical metric $g_{\mu\nu}$ and the auxiliary metric $f_{\mu\nu}$ respectively, with reduced Planck masses $M_g^2 = (8\pi G)^{-1}$ and $M_f^2 = (8\pi\mathcal{G})^{-1}$, and gravitational couplings G and $\mathcal{G}$. All matter degrees of freedom are encoded in $S_{\rm mat}$, which couples directly only to the physical metric.

The physical and auxiliary metrics communicate with each other through the interaction term $\mathcal{L}_{\rm int}$, which can be written as

$$\mathcal{L}_{\rm int} = \sum_{n=0}^{4} \beta_n e_n(\gamma), \tag{2.2}$$

where β_n are dimensionless coupling parameters and $e_n(\gamma)$ are the elementary

symmetric polynomials of the trace of the so-called "square-root matrix," defined by

$$\gamma^{\mu}{}_{\alpha}\gamma^{\alpha}{}_{\nu} = g^{\mu\alpha}f_{\alpha\nu}\,. \tag{2.3}$$

The coupling strength of the interaction term is controlled by the product of an "effective" Planck mass

$$M_{\rm eff}^2 = \left(\frac{1}{M_g^2} + \frac{1}{M_f^2}\right)^{-1}. \tag{2.4}$$

and a continuous scaling parameter m that is related (but not equal) to the mass of the graviton. The latter could be absorbed into the β_n parameters, but we will not do so here so that the β_n parameters are of order unity[1].

Without any loss of generality, the interaction term can be rewritten as

$$\mathcal{L}_{\rm int} = \sum_{n=0}^{4} c_n e_n(K), \tag{2.5}$$

where $K^{\mu}{}_{\nu} = \delta^{\mu}{}_{\nu} - \gamma^{\mu}{}_{\nu}$. This form of the interaction term allows us to easily enforce asymptotic flatness by requiring $c_0 = c_1 = 0$, and to reduce the theory to that of Pauli and Fierz [73] in the linearized limit of a massive spin 2 field by requiring $c_2 = 1$. The mapping from the remaining c_n to β_n is then

$$\beta_n = (-1)^{n+1}\left[\frac{1}{2}(3-n)(4-n) - (4-n)\,c_3 - c_4\right]. \tag{2.6}$$

[1]If one wished to consider a β_n that is larger than order unity, then one could simply increase the scaling parameter m.

With this at hand, the interaction term becomes simply

$$\begin{aligned}\mathcal{L}_{\rm int} &= \frac{1}{2}\left(K^{\mu}{}_{\mu}\right)^2 - \frac{1}{2}K^{\nu}{}_{\mu}K^{\mu}{}_{\nu} \\ &+ \frac{c_3}{3!}\epsilon_{\mu\nu\rho\sigma}\epsilon^{\alpha\beta\gamma\sigma}K^{\mu}{}_{\alpha}K^{\nu}{}_{\beta}K^{\rho}{}_{\gamma} \\ &+ \frac{c_4}{4!}\epsilon_{\mu\nu\rho\sigma}\epsilon^{\alpha\beta\gamma\delta}K^{\mu}{}_{\alpha}K^{\nu}{}_{\beta}K^{\rho}{}_{\gamma}K^{\sigma}{}_{\delta}\,, \end{aligned} \tag{2.7}$$

where $\epsilon^{\alpha\beta\gamma\delta}$ is the Levi-Civita tensor.

One can now obtain the field equations by varying the action with respect to both metrics. Doing so directly, however, is somewhat cumbersome due to the dependence of the interaction term on the square-root metric. Following [95], one can instead introduce two tetrad fields, $e^{\mu}{}_{A}$ and $\omega^{B}{}_{\nu}$, defined via

$$g^{\mu\nu} = \eta^{AB}e^{\mu}{}_{A}e^{\nu}{}_{B} \qquad \text{and} \qquad f_{\mu\nu} = \eta_{AB}\omega^{A}{}_{\mu}\omega^{B}{}_{\nu}. \tag{2.8}$$

By imposing the symmetry condition

$$e^{\mu}{}_{A}\omega_{B\mu} = e^{\mu}{}_{B}\omega_{A\mu}, \tag{2.9}$$

the square-root matrix can then be rewritten as

$$\gamma^{\mu}{}_{\nu} = e^{\mu}{}_{A}\omega^{A}{}_{\nu}. \tag{2.10}$$

With this at hand, one can then vary the action with respect to these tetrad fields to obtain the field equations

$$G^{\mu}{}_{\nu} = 8\pi T^{\mu}{}_{\nu} + m^2\cos^2\eta\; V^{\mu}{}_{\nu}\,, \tag{2.11}$$

$$\mathcal{G}^{\mu}{}_{\nu} = m^2\sin^2\eta\;\mathcal{V}^{\mu}{}_{\nu}. \tag{2.12}$$

where we have introduced the new coupling constant $\eta \in [0, \frac{\pi}{2}]$ via [95]

$$\tan^2 \eta = \frac{\mathcal{G}}{G}. \tag{2.13}$$

The auxiliary reduced Planck mass is then simply $M_f^2 = M_g^2 \cot^2 \eta$, while the reduced effective Planck mass is $M_{\rm eff}^2 = M_g^2 \cos^2 \eta$. The Einstein tensors $G^\mu{}_\nu$ and $\mathcal{G}^\mu{}_\nu$ are those associated with the physical and auxiliary metrics respectively, while $T^\mu{}_\nu$ is the matter stress-energy tensor, which again couples only to the physical metric. The interaction tensors, $V^\mu{}_\nu$ and $\mathcal{V}^\mu{}_\nu$, are defined by

$$V^\mu{}_\nu = \tau^\mu{}_\nu - \delta^\mu{}_\nu \mathcal{L}_{\rm int}, \tag{2.14}$$

$$\mathcal{V}^\mu{}_\nu = -\frac{\sqrt{-g}}{\sqrt{-f}} \tau^\mu{}_\nu, \tag{2.15}$$

with

$$\begin{aligned} \tau^\mu{}_\nu = & -3\,\gamma^\mu{}_\nu + \gamma^\mu{}_\mu \gamma^\nu{}_\nu - \gamma^\mu{}_\alpha \gamma^\alpha{}_\nu \\ & - \frac{c_3}{2} \epsilon_{\nu\rho\lambda\sigma} \epsilon^{\alpha\beta\delta\sigma} \gamma^\mu{}_\alpha K^\rho{}_\beta K^\lambda{}_\delta \\ & - \frac{c_4}{6} \epsilon_{\nu\rho\lambda\sigma} \epsilon^{\alpha\beta\chi\delta} \gamma^\mu{}_\alpha K^\rho{}_\beta K^\lambda{}_\chi K^\sigma{}_\delta \,. \end{aligned} \tag{2.16}$$

The effective mass of the graviton μ is determined from a linear analysis of the field equations about flat spacetime [40]

$$\mu = m \left[\frac{(1 + \cot^2 \eta\, \xi_c^2)^{1/2}\, \Gamma_c^{1/2}}{\cot \eta\, \xi_c} \right], \tag{2.17}$$

where $\Gamma_c \equiv \beta_1 \xi_c + 4\beta_2 \xi_c^2 + 6\beta_3 \xi_c^3$ and ξ_c is the critical value of the ratio of the cosmological scale factor associated with the auxiliary metric to that associated with the physical metric when the cosmological matter energy density asymptotes to zero.

One can show that ξ_c is a solution to the polynomial equation [40]

$$\begin{aligned} 0 = &\frac{\beta_1}{\cot^2\eta\,\xi_c} + \left(\frac{6\beta_2}{\cot^2\eta} - \beta_0\right) + \left(\frac{18\beta_3}{\cot^2\eta} - 3\beta_1\right)\xi_c \\ &+ \left(\frac{24\beta_4}{\cot^2\eta} - 6\beta_2\right)\xi_c^2 - 6\beta_3\xi_c^3, \end{aligned} \tag{2.18}$$

Thus, the effective graviton mass is a function of all 4 coupling parameters. We see that η does not completely control the mass of the graviton, but rather this is really determined by all coupling parameters, and in particular the scaling mass m.

The field equations also lead to certain conservation relations. Taking the g- and f-metric covariant divergences of Eqs. (2.11) and (2.12), we find

$$8\pi\ {}_{(\mathrm{g})}\nabla^\nu T^\mu{}_\nu = -m^2\cos^2\eta\ {}_{(\mathrm{g})}\nabla^\nu V^\mu{}_\nu\,, \tag{2.19}$$

$${}_{(\mathrm{f})}\nabla^\nu \mathcal{V}^\mu{}_\nu = 0\,, \tag{2.20}$$

where the Bianchi identities require that ${}_{(\mathrm{g})}\nabla^\nu G^\mu{}_\nu = 0 = {}_{(\mathrm{f})}\nabla^\nu \mathcal{G}^\mu{}_\nu$. The diffeomorphism invariance of the action, however, guarantees that the matter stress-energy tensor is independently conserved [94]

$${}_{(\mathrm{g})}\nabla^\nu T^\mu{}_\nu = 0\,, \tag{2.21}$$

which then implies that

$${}_{(\mathrm{g})}\nabla^\nu V^\mu{}_\nu = 0\,. \tag{2.22}$$

Slowly-rotating Neutron stars in Massive Bigravity within the Hartle-Thorne Approximation

In this section, we first introduce our choice of metric ansatzes, following the Hartle and Thorne approximation [54, 55], and then we describe our choice of stress-energy tensors to model neutron stars. We conclude this section with a derivation of the field equations in a slow-rotation expansion and a recasting of them into a form amenable to numerical integration.

Metric Tensors for Slowly-Rotating Spacetimes

Following the approach of Hartle and Thorne [54, 55], we begin with the following metric ansatzes

$$ds_{\rm g}^2 = -e^{2\nu}dt^2 + e^{2\lambda}dr^2 + r^2\left[d\theta^2 + \sin^2\theta\,(d\phi - \omega dt)^2\right], \tag{2.23}$$

$$ds_{\rm f}^2 = -e^{2\alpha}dt^2 + e^{2\beta}dr^2 + U^2\left[d\theta^2 + \sin^2\theta\,(d\phi - w dt)^2\right], \tag{2.24}$$

where each metric function ν, λ, α, β, U, ω, and w are functions of r and θ only. The above metric ansatzes are the result of an expansion in slow rotation to second order of the most general, stationary and axisymmetric metric. We make here a *symmetric* choice of ansatzes: we choose the same functional form for the g- and the f-metrics. This is a choice because, although the g-metric must take the form above when imposing stationarity and axisymmetry, the f-metric could in principle take a different form. We will see below that this symmetric choice is sufficient to find consistent solutions.[2]

[2]Relaxing this assumption for vacuum solutions where the physical metric ansatz is diagonal while the auxiliary metric is not can produce vacuum solutions that are Schwarzschild-(anti) de Sitter [95]. Thus there may also exist solutions of this type for neutron stars but they will not be considered here.

Neutron Star Stress-Energy Tensor

We model the matter field as a perfect fluid that is uniformly rotating with angular velocity Ω. The matter stress-energy tensor for such a fluid is

$$T^{(\mathrm{m})\mu}{}_{\nu} = (p+\rho)\, u^{\mu} u_{\nu} + p\, g^{\mu}{}_{\nu}, \tag{2.25}$$

with density ρ, pressure p and four-velocity

$$u^{\mu} = \left[u^{t}, 0, 0, \Omega\, u^{t}\right]. \tag{2.26}$$

The component u^t is obtained from the normalization condition $u^{\mu}u_{\mu} = -1$,

$$u^{t} = \frac{1}{e^{\nu}} + \frac{1}{2}\frac{r^{2}\sin^{2}\theta}{e^{3\nu}}\left(\omega^{2} - 2\omega\Omega + \Omega^{2}\right) + \mathcal{O}\left(\Omega^{4}\right). \tag{2.27}$$

Ignoring terms of $\mathcal{O}\left(\Omega^{2}\right)$, the stress-energy tensor in matrix form is then

$$T^{(\mathrm{m})\mu}{}_{\nu} = \begin{pmatrix} -\rho & 0 & 0 & \frac{r^{2}\sin^{2}\theta}{e^{2\nu}}\left(\Omega-\omega\right)\left(p+\rho\right) \\ 0 & p & 0 & 0 \\ 0 & 0 & p & 0 \\ -\Omega\left(p+\rho\right) & 0 & 0 & p \end{pmatrix}. \tag{2.28}$$

In order to close our system of equations we require a relationship between the pressure and the density. We here only consider barotropic equations of state, namely $p = p(\rho)$, that are obtained numerically by solving certain systems of equations in nuclear physics. In particular, we focus on the Akmal-Pandharipande-Ravenhall (APR) [9], Lattimer-Swesty (LS220) [63], and Shen et al. [85] equations of state. APR uses a variational chain summation method combined with a leading-order

relativistic correction and three-nucleon interactions. LS220 uses a compressible liquid-drop model for nuclei and includes multiple additional nuclear interactions. Shen is constructed from relativistic mean field theory over a wide range of baryon mass densities, temperatures, and proton fractions. These equations of state allow for neutron stars with masses above the PSR J1614-2230 limit (above $2.01M_\odot$ [11]) in GR.[3]

Interaction Tensor

Before we can find the modified field equations, we must first evaluate the interaction tensors, which in turn require the calculation of the square-root matrix. Let us then begin with the latter, using Eq. (2.3) and an axisymmetric choice for the tetrad fields e^μ_A and ω^A_μ:

$$\begin{aligned} e^\mu_t &= [M,0,0,K]\,, & \omega^t_\mu &= [m,0,0,k]\,,\\ e^\mu_r &= [0,B,0,0]\,, & \omega^r_\mu &= [0,b,0,0]\,,\\ e^\mu_\theta &= [0,0,C,0]\,, & \omega^\theta_\mu &= [0,0,c,0]\,,\\ e^\mu_\phi &= [X,0,0,Y]\,, & \omega^\phi_\mu &= [x,0,0,y]\,. \end{aligned} \tag{2.29}$$

[3]We will assume this value as our constraint for a maximum mass in massive bigravity.

where $(M, K, B, C, X, Y, m, k, b, c, x, y)$ are arbitrary functions of (r, θ). Using Eqs. (2.8) and (2.10), we then find

$$g^{\mu\nu} = \begin{pmatrix} -M^2 + Y^2 & 0 & 0 & -M\,K + X\,Y \\ 0 & B^2 & 0 & 0 \\ 0 & 0 & C^2 & 0 \\ -M\,K + X\,Y & 0 & 0 & -K^2 + X^2 \end{pmatrix}, \tag{2.30}$$

$$f_{\mu\nu} = \begin{pmatrix} -m^2 + y^2 & 0 & 0 & -m\,k + x\,y \\ 0 & b^2 & 0 & 0 \\ 0 & 0 & c^2 & 0 \\ -m\,k + x\,y & 0 & 0 & -k^2 + x^2 \end{pmatrix}, \tag{2.31}$$

$$\gamma^{\mu}{}_{\nu} = \begin{pmatrix} Mm + Yy & 0 & 0 & Mk + Yx \\ 0 & Bb & 0 & 0 \\ 0 & 0 & Cc & 0 \\ Km + Xy & 0 & 0 & Kk + Xx \end{pmatrix}. \tag{2.32}$$

Comparing the above metric tensors to the metric ansatzes in Eqs. (2.23) and (2.24), and comparing the square-root matrix above to that obtained from Eq. (2.3) computed with the metric ansatzes of Eqs. (2.23) and (2.24), the only solution that is spherically symmetric in the non-rotating limit [95] is

$$\begin{aligned} M &= e^{-\nu}, & K &= \omega\, e^{-\nu}, \\ X &= (r\sin\theta)^{-1}, & Y &= 0, \\ m &= a, & k &= 0, \\ x &= U\sin\theta, & y &= -wU\sin\theta. \end{aligned} \tag{2.33}$$

With this solution, we can use the tetrad symmetry condition in Eq. (2.9) to show that $\omega = w$, i.e. frame dragging is identical in both spacetimes. With the basis solution found above, the square-root matrix is

$$\gamma^{\mu}{}_{\nu} = \begin{pmatrix} e^{\alpha-\nu} & 0 & 0 & 0 \\ 0 & e^{\beta-\lambda} & 0 & 0 \\ 0 & 0 & U/r & 0 \\ \omega\left(e^{\alpha-\nu} - U/r\right) & 0 & 0 & U/r \end{pmatrix}. \tag{2.34}$$

With the square-root matrix in hand, we can now calculate the full interaction tensors, $V^{\mu}{}_{\nu}$ and $\mathcal{V}^{\mu}{}_{\nu}$, from Eqs. (2.14) and (2.15):

$$\begin{aligned} V^{t}_{\ t} &= \kappa_1 \frac{e^{\beta}}{e^{\lambda}} + \kappa_2, \\ V^{r}_{\ r} &= \kappa_1 \frac{e^{\alpha}}{e^{\nu}} + \kappa_2, \\ V^{\theta}_{\ \theta} = V^{\phi}_{\ \phi} &= -\frac{e^{\alpha}}{e^{\nu}}\left(\kappa_3 \frac{e^{\beta}}{e^{\lambda}} + \kappa_4\right) - \kappa_4 \frac{e^{\beta}}{e^{\lambda}} + \kappa_5, \\ V^{\phi}_{\ t} &= \omega\left(\frac{U}{r} - \frac{e^{\alpha}}{e^{\nu}}\right)\left(\kappa_3 \frac{e^{\beta}}{e^{\lambda}} + \kappa_4\right), \\ \mathcal{V}^{t}_{\ t} &= \kappa_6 \frac{e^{\lambda}}{e^{\beta}} + \kappa_7, \\ \mathcal{V}^{r}_{\ r} &= \kappa_6 \frac{e^{\nu}}{e^{\alpha}} + \kappa_7, \\ \mathcal{V}^{\theta}_{\ \theta} = \mathcal{V}^{\phi}_{\ \phi} &= -\frac{e^{\nu}}{e^{\alpha}}\left(\kappa_8 \frac{e^{\lambda}}{e^{\beta}} + \kappa_9\right) - \kappa_9 \frac{e^{\lambda}}{e^{\beta}} + \kappa_{10}, \\ \mathcal{V}^{\phi}_{\ t} &= \omega\left(\frac{e^{\nu}}{e^{\alpha}} - \frac{r}{U}\right)\left(\kappa_8 \frac{e^{\lambda}}{e^{\beta}} + \kappa_9\right), \end{aligned} \tag{2.35}$$

where

$$
\begin{aligned}
\kappa_1 &= 3 - 3c_3 - c_4 + (4c_3 + 2c_4 - 2)\frac{U}{r} - (c_3 + c_4)\frac{U^2}{r^2}, \\
\kappa_2 &= -6 + 4c_3 + c_4 - (6c_3 + 2c_4 - 6)\frac{U}{r} + (2c_3 + c_4 - 1)\frac{U^2}{r^2}, \\
\kappa_3 &= 1 - 2c_3 - c_4 + (c_3 + c_4)\frac{U}{r}, \\
\kappa_4 &= -3 + 3c_3 + c_4 - (2c_3 + c_4 - 1)\frac{U}{r}, \\
\kappa_5 &= -6 + 4c_3 + c_4 - (3c_3 + c_4 - 3)\frac{U}{r}, \\
\kappa_6 &= -c_3 - c_4 + (4c_3 + 2c_4 - 2)\frac{r}{U} - (3c_3 + c_4 - 3)\frac{r^2}{U^2}, \\
\kappa_7 &= c_4 - (2c_3 + 2c_4)\frac{r}{U} + (2c_3 + c_4 - 1)\frac{r^2}{U^2}, \\
\kappa_8 &= 1 - 2c_3 - c_4 + (3c_3 + c_4 - 3)\frac{r}{U}, \\
\kappa_9 &= c_3 + c_4 - (2c_3 + c_4 - 1)\frac{r}{U}, \\
\kappa_{10} &= c_4 - (c_3 + c_4)\frac{r}{U}.
\end{aligned}
\tag{2.36}
$$

Modified Field Equations

Combining the above results we can write the equations of stellar structure for a neutron star in massive bigravity. The approach is similar to that in GR, so let us begin by deriving the field equations to zeroth-order in slow-rotation. Making the familiar GR substitution

$$
e^{2\lambda} = \left(1 - \frac{2m_g}{r}\right)^{-1}, \tag{2.37}
$$

where m_g is a new function of r only, the (t,t) and (r,r) component of the g-metric field equations become

$$
\frac{dm_g}{dr} = 4\pi r^2 \rho - \frac{1}{2} m^2 \cos^2\eta \, r^2 V^t_t \,, \tag{2.38}
$$

$$
\frac{d\nu}{dr} = \frac{4\pi r^3 p + m_g}{r\,(r - 2m_g)} + \frac{1}{2}\frac{m^2 \cos^2\eta \, r^2 V^r_r}{r - 2m_g}. \tag{2.39}
$$

Notice that as $m \to 0$ or $\eta \to \pi/2$, $m_g(r)$ becomes the GR total enclosed mass of the neutron star inside radius r.

We can express the f-metric equations in a similar manner. Using the substitution

$$e^{2\beta} = U'^2 \left(1 - \frac{2m_f}{U}\right)^{-1}, \tag{2.40}$$

where m_f is a new function of r only and $U' = dU/dr$, the (t,t) and (r,r) components of the f-metric field equations become

$$\frac{dm_f}{dr} = -\frac{1}{2} m^2 \sin^2\eta \; U^2 \; U' \; \mathcal{V}^t_{\ t}, \tag{2.41}$$

$$\frac{d\alpha}{dr} = U' \left[\frac{m_f}{U\,(U-2m_f)} + \frac{1}{2}\frac{m^2 \sin^2\eta U^2 \mathcal{V}^r_{\ r}}{U-2m_f}\right]. \tag{2.42}$$

We have so far obtained four equations for the four metric function unknowns (ν, m_g, α, m_f), but we still need equations for (p, ρ, U). The equation of state provides a relation between p and ρ. Conservation of the matter stress-energy tensor, Eq. (2.21), leads to the equation

$$\frac{dp}{dr} = -\,(p+\rho)\,\frac{d\nu}{dr}. \tag{2.43}$$

Conservation of the $V^{\mu}_{\ \nu}$ tensor, Eq. (2.22), leads to the equation

$$\kappa_1 \frac{e^\alpha}{e^\nu}\frac{d\alpha}{dr} = \frac{2}{r}\left(\kappa_3 \frac{e^\alpha}{e^\nu} + \kappa_4\right) U' + \left[\kappa_1 \frac{d\nu}{dr} - \frac{2}{r}\left(\kappa_3 \frac{e^\alpha}{e^\nu} + \kappa_4\right)\right] \sqrt{\frac{U\,(r-2m_g)}{r\,(U-2m_f)}} U', \tag{2.44}$$

which then closes our system of ordinary differential equations at zeroth-order in spin.

Let us now consider the modified field equations to first-order in slow-rotation. To this order, ω is the only free metric function, and thus, we only need a single differential equation. Investigating the (t,ϕ) component of the g-metric field equation,

we find

$$\frac{\partial^2\omega}{\partial r^2}+\frac{4}{r}\left[1-\frac{\pi r^3\left(p+\rho\right)}{r-2m_g}-\frac{m^2\cos^2\eta\, r^3}{8\left(r-2m_g\right)}\left(V^r_{\ r}-V^t_{\ t}\right)\right]\frac{\partial\omega}{\partial r}$$
$$+\frac{16\pi r\left(p+\rho\right)}{r-2m_g}\left(\Omega-\omega\right)+\frac{1}{r\left(r-2m_g\right)}\left(\frac{\partial^2\omega}{\partial\theta^2}+3\frac{\cos\theta}{\sin\theta}\frac{\partial\omega}{\partial r}\right)$$
$$+\frac{1}{2}\frac{m^4\cos^4\eta\, r^4 V^r_{\ r}\left(V^t_{\ t}-V^r_{\ r}\right)}{\left(r-2m_g\right)^2}\omega-m^2\cos^2\eta$$
$$\times\left[\frac{r\left(V^r_{\ r}-V^t_{\ t}\right)}{\left(r-2m_g\right)^2}\left(4\pi r^3p+m_g\right)+\frac{r^2}{r-2m_g}\frac{dV^r_{\ r}}{dr}+\frac{2r}{r-2m_g}\left(V^r_{\ r}+V^{\phi}_{\ \phi}\right)\right]\omega=0. \tag{2.45}$$

Following [54], we use a vector spherical harmonic decomposition

$$\omega(r,\theta)=\sum_{l=1}^{\infty}\omega_l(r)\left(-\frac{1}{\sin\theta}\frac{dP_l(\cos\theta)}{d\theta}\right), \tag{2.46}$$

where $P_l(\cos\theta)$ are Legendre polynomials, to decouple this equation. The polar term becomes

$$\frac{\partial^2\omega}{\partial\theta^2}+3\frac{\cos\theta}{\sin\theta}\frac{\partial\omega}{\partial\theta}=-\left(l+2\right)\left(l-1\right)\omega. \tag{2.47}$$

By imposing regularity at the neutron star core and asymptotic flatness, all ω_l must vanish except for the $l=1$ term, as expected. Equation (2.45) then becomes

$$\frac{\partial^2\omega}{\partial r^2}+\frac{4}{r}\left[1-\frac{\pi r^3\left(p+\rho\right)}{r-2m_g}-\frac{m^2\cos^2\eta\, r^3}{8\left(r-2m_g\right)}\left(V^r_{\ r}-V^t_{\ t}\right)\right]\frac{\partial\omega}{\partial r} \tag{2.48}$$
$$+\frac{16\pi r\left(p+\rho\right)}{r-2m_g}\left(\Omega-\omega\right)+\frac{1}{2}\frac{m^4\cos^2\eta\, r^4 V^r_{\ r}\left(V^t_{\ t}-V^r_{\ r}\right)}{\left(r-2m_g\right)^2}\omega-m^2\cos^2\eta$$
$$\times\left[\frac{r\left(V^r_{\ r}-V^t_{\ t}\right)}{\left(r-2m_g\right)^2}\left(4\pi r^3p+m_g\right)+\frac{r^2}{r-2m_g}\frac{dV^r_{\ r}}{dr}+\frac{2r}{r-2m_g}\left(V^r_{\ r}+V^{\phi}_{\ \phi}\right)\right]\omega=0. \tag{2.49}$$

Recasting of Modified Field Equations

The equations of stellar structure presented thus far are not ideal for numerical integration in their present form. We here follow the approach of [95] to recast the differential equations into a simpler form. First, we substitute Eq. (2.42) into (2.44), causing each U' to cancel exactly from the latter. We then use Eq. (2.39) to solve for the quantity $e^{(\alpha-\nu)}$ in the resulting expression. The right-hand side of this expression is lengthy and will be denoted as the function F that depends on the metric functions m_g, m_f, r, and U and the coupling parameters m, c_3, c_4, and η:

$$\frac{e^{\alpha}}{e^{\nu}} = F\left[r, m_g, m_f, U, m, c_3, c_4, \eta\right] \tag{2.50}$$

This expression allows us to simplify our differential system because α and ν only appear in this particular combination. Thus, we insert Eq. (2.50) into Eq. (2.39) and (2.42), to eliminate ν and α from our differential system.

To further simplify the equations, we insert Eqs. (2.37) and (2.40) into the V_t^t term of Eq. (2.38) (and similarly in the $\mathcal{V}_t^t$ term of Eq. (2.41)). This separates the equations into two terms: one that is proportional to U' and one that is independent of U'. Each of these terms are lengthy and will be denoted as separate functions $F_k = F_k\left[r, m_g, m_f, U, m, c_3, c_4, \eta\right]$ with $k \in (1, 6)$; such that our simplified differential system is

$$\frac{dm_g}{dr} = F_1 \frac{dU}{dr} + F_2 \tag{2.51}$$

$$\frac{dm_f}{dr} = F_3 \frac{dU}{dr} + F_4 \tag{2.52}$$

$$\frac{d\nu}{dr} = F_5 \tag{2.53}$$

$$\frac{d\alpha}{dr} = F_6 \frac{dU}{dr}. \tag{2.54}$$

A few of the F_k functions are given explicitly in Appendix A to show an example of their structure.

To close the system, we now need an equation for the evolution of U. Taking a total derivative of both sides of Eq. (2.50) and substituting Eqs. (2.51) — (2.54), one can solve for dU/dr to find

$$\frac{dU}{dr} = \frac{\frac{\partial F}{\partial r} + \frac{\partial F}{\partial m_g} F_2 + \frac{\partial F}{\partial m_f} F_4 + F\, F_5}{F\, F_6 - \frac{\partial F}{\partial U} - \frac{\partial F}{\partial m_g} F_1 - \frac{\partial F}{\partial m_f} F_3}, \tag{2.55}$$

provided the denominator does not vanish. The numerical problem then reduces to simultaneously solving Eqs. (2.51), (2.52), and (2.55). Once this is done, one can insert (m_g, m_f, U) in the right-hand sides of Eqs. (2.53) and (2.54) to solve for (α, ν). Alternatively, once we have solved for α (or ν), we can use Eq. (2.50) to find ν (or α).

Numerical Construction of Neutron Stars in Massive Bigravity

In this section, we describe how to numerically evolve the differential system obtained in the previous section, beginning with the system at zeroth-order in rotation and continuing with the first-order in rotation system. In general, we will use a shooting method to solve the equations:

(i) choose boundary conditions at a small radius (close enough to the neutron star core) and at a very large radius (close enough to spatial infinity),

(ii) numerically integrate from the small radius out to the surface and from the large radius in to the surface,

(iii) check whether the solutions are continuous and differentiable at the surface, and

(iv) if they are, declare this our solution; if they are not, choose different boundary conditions and repeat.

This shooting method then requires that we specify boundary conditions both at the core and at a large radius, which we do through a local analysis about $r = 0$ and $r = \infty$, as we will describe below. The key point of this method is that the boundary conditions will depend on integration constants that must be iterated over (or "shot for") to ensure continuity and differentiability.

Zeroth-Order in Rotation

Local analysis at $r = 0$ and $r = \infty$ At $r = 0$, we Taylor expand m_g, m_f, ν, α, p, ρ, and U, insert the Taylor expansions into the differential system of the previous

section, and equate coefficients of equal power in r to find

$$
\begin{aligned}
U_{r\to 0} &= ur + \mathcal{O}(r^3),\\
m_{g_{r\to 0}} &= \frac{4}{3}\pi r^3\rho_0 + \frac{1}{3}m^2\cos^2\eta\, r^3\,(u-1)\\
&\quad\times\left[(c_3+c_4)\,u^2 - \left(\frac{5}{2}c_3 + c_4 + \frac{3}{2}\right)u + 4c_3 + \frac{1}{2}c_4 + 3\right] + \mathcal{O}(r^4),\\
m_{f_{r\to 0}} &= -\frac{1}{6}m^2\sin^2\eta\, r^3\,(u-1)\left[-c_4u^2 + (3c_3+2c_4)\,u - 3c_3 - c_4 + 3\right] + \mathcal{O}(r^4),\\
\nu_{r\to 0} &= \nu_0 + \frac{1}{2}r^2\left(4\pi p_0 + \frac{4}{3}\pi\rho_0\right) + \frac{1}{2}m^2\cos^2\eta\, r^2\Bigg\{-\frac{1}{6}(c_3+c_4)\,u^3\\
&\quad - \frac{1}{2}(3c_3+c_4-3)\,u + \frac{1}{3}(4c_3+c_4-6) +\\
&\quad + \left[\frac{1}{2}(c_3+c_4)\,u^2 - (2c_3+c_4-1)\,u + \frac{1}{2}(3c_3+c_4-3)\right]\frac{e^{\alpha_0}}{e^{\nu_0}}\Bigg\} + \mathcal{O}(r^3),\\
\alpha_{r\to 0} &= \alpha_0 + \frac{1}{4u}m^2\sin^2\eta\, r^2\Bigg\{\frac{4}{3}c_4u^3 - 3(c_3+c_4)\,u^2 + 2(2c_3+c_4-1)\,u - c_3 - \frac{1}{3}c_4 +\\
&\quad + 1 + u\left[-(c_3+c_4)\,u^2 + (4c_3+2c_3-2)\,u - 3c_3 - c_4 + 3\right]\frac{e^{\nu_0}}{e^{\alpha_0}}\Bigg\} + \mathcal{O}(r^3),\\
\rho_{r\to 0} &= \rho_0 + \mathcal{O}(r^2),\\
p_{r\to 0} &= p_0 + \mathcal{O}(r^2).
\end{aligned}
\tag{2.56}
$$

The quantity ρ_0 is the central density, i.e. the density at the neutron star core, and it is a free parameter that effectively determines the mass of the star. Given ρ_0, the quantity p_0 is obtained from the equation of state, $p_0 = p[\rho_0]$. The quantities u and ν_0 are constants that must be shot for in order to guarantee continuity and differentiability of the solutions at the stellar surface. Given all of this, the quantity α_0 is obtained from Eq. (2.50).

At $r = \infty$, we take a slightly different approach. If we insisted on a regular Taylor expansion of the metric functions, we would find that this ansatz does not satisfy the field equations. Instead, the field equations require a series expansion

with a non-trivial controlling factor. This can be proved by parameterizing the local behavior of the metric functions via

$$\begin{aligned} U_{r\to\infty} &= r + \delta\, U_\infty, \\ m_{g_{r\to\infty}} &= \delta\, m_{g_\infty}, \\ m_{f_{r\to\infty}} &= \delta\, m_{f_\infty}, \\ \nu_{r\to\infty} &= \delta\, \nu_\infty, \\ \alpha_{r\to\infty} &= \delta\, \alpha_\infty, \end{aligned} \tag{2.57}$$

which ensures asymptotic flatness, where U_∞, m_{g_∞}, m_{f_∞}, ν_∞, and α_∞ are functions of r and $\delta \ll 1$. Plugging the above into the field equations and keeping only terms of $\mathcal{O}(\delta)$ gives

$$\begin{aligned} \frac{d}{dr}U_\infty &= \frac{m_{g_\infty} - m_{f_\infty}}{r} + 2\frac{m_g - m_f}{m^2 r^3}, \\ \frac{d}{dr}m_{g_\infty} &= m^2 \cos^2\eta\, r\, U_\infty + \cos^2\eta \frac{m_{g_\infty} - m_{f_\infty}}{r}, \\ \frac{d}{dr}m_{f_\infty} &= -m^2 \sin^2\eta\, r\, U_\infty - \sin^2\eta \frac{m_{g_\infty} - m_{f_\infty}}{r}, \\ \frac{d}{dr}\nu_\infty &= \frac{m_{g_\infty}}{r^2} + \cos^2\eta \frac{m_{g_\infty} - m_{f_\infty}}{r^2}, \\ \frac{d}{dr}\alpha_\infty &= \frac{2m_{f_\infty} - m_{g_\infty}}{r^2} + \cos^2\eta \frac{m_{g_\infty} - m_{f_\infty}}{r^2}. \end{aligned} \tag{2.58}$$

Solving this system of equations gives the asymptotic behavior,

$$\begin{aligned} U_{r\to\infty} &= r + \frac{m^2 r^2 + mr + 1}{m^2 r^2} B e^{-mr}, \\ m_{g_{r\to\infty}} &= A \sin^2\eta - B\cos^2\eta\,(mr+1)\, e^{-mr}, \\ m_{f_{r\to\infty}} &= A \sin^2\eta + B\sin^2\eta\,(mr+1)\, e^{-mr}, \\ \nu_{r\to\infty} &= -\frac{A\sin^2\eta}{r} + \frac{2B\cos^2\eta}{r} e^{-mr}, \\ \alpha_{r\to\infty} &= -\frac{A\sin^2\eta}{r} - \frac{2B\sin^2\eta}{r} e^{-mr}, \end{aligned} \tag{2.59}$$

where A and B are constants that are to be shot for by requiring continuity and differentiability of the solution at the stellar surface.

Numerical Solutions Combining the above results, we can then solve for non-rotating neutron star solutions. The procedure is as follows. First, we specify a central density and choose an initial guess of the 4 matching parameters (u, ν_0, A, B). Second, using the boundary conditions at the neutron star core, we integrate outwards until the pressure vanishes, which denotes the surface of the star. Third, using the boundary conditions at infinity, we integrate inwards until the neutron star surface is reached. All integrations are carried out with an adaptive Runge-Kutta-Fehlberg algorithm with an error tolerance of 10^{-4}. Finally, we compare the metric functions at the surface to determine whether the solutions are continuous and differentiable also to a tolerance of 10^{-4}. If they are not, we use a four-dimensional Newton-Raphson method to estimate a new guess for the 4 matching parameters, until the solutions are continuous and differentiable at the surface to the tolerance required.

The double-shooting, numerical procedure used here is different from that used in GR. The exterior solution to the Einstein equations is known analytically, so in GR it is sufficient to integrate from the stellar core to the surface, and then match this numerical solution and its first derivative to the analytical exterior solution. In massive bigravity, however, the exterior solution is not known analytically. Therefore, it is standard to shoot from "both ends" when carrying out the numerical integration of the field equations [53], which is typically referred to as "shooting to a fitting point" [74].

When solving for non-rotating neutron stars numerically, we must choose the region in coupling parameter space (m, η, c_3, c_4) that we wish to explore. We here choose the range of η to be its entire domain $(0, \pi/2)$ and the range of (c_3, c_4) to be

approximately that used in [33], which was obtained from analytic considerations of scattering amplitudes in massive gravity. This choice is made so as to get a clear sense of the effect of bigravity modifications to GR, but clearly some range in (m, η, c_3, c_4) is already disallowed by observations [42]. Solar System observations of the precession of Mercury place the bound $\mu < 10^{-23}$eV [96], while constraints on the dispersion relation of the gravitational wave signal GW150914 place the bound $\mu < 10^{-22}$eV [7]. Since μ is related to (m, η, c_3, c_4) via Eq. (2.17), values of η close to $\pi/2$ are not yet ruled out.

We should note, however, that we were unable to numerically produce stars in this entire (c_3, c_4) subregion. In fact, we were only able to find solutions in the shaded region shown in Fig. 2.3. This region grows in size slightly for larger values of m. The most common cause of numerical issues is the denominator of Eq. (2.55) becoming very small at a rate faster than the numerator. Whether this is due to a numerical limitation of our methods or whether it points to a deeper theoretical issue in massive bigravity is currently unclear and requires further study.

We present the non-rotating solutions for various couplings in Figs. 2.4 and 2.5. All five metric profiles m_g, m_f, U, ν, and α are shown as functions of radius for different coupling parameters (m, η, c_3, c_4). The top left panel of Fig. 2.4 shows both the physical and the auxiliary mass functions versus radius. Observe that both increase monotonically from the core to the surface, with m_g increasing much more rapidly than m_f due to its direct matter coupling. Outside the star, the density term in Eq. (2.38) vanishes and the physical (auxiliary) mass monotonically decreases (increases) until it reaches its asymptotic value $m_g = A \sin^2 \eta$, determined by Eq. (2.59). Thus, the observable mass sufficiently far away from the star is determined by the matching parameter A, and the ratio of gravitational couplings $\tan^2 \eta = \mathcal{G}/G$. The parameter η controls this asymptotic value, while the primary

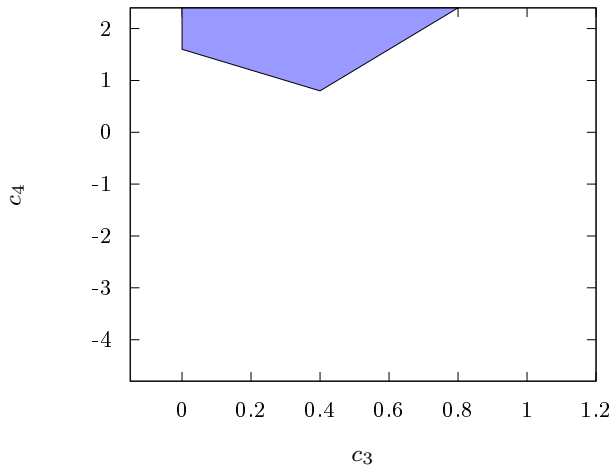

Figure 2.3: Numerical region of the expolored (c_3, c_4) space. The figure is bounded by an estimate of the constrained region determined in [33]. The shaded region shows the subregion in which we were able to numerically produce neutron stars solutions using the APR equation of state, with $\rho_0 = 7.9 \times 10^{14}\text{g/cm}^3$, $m = 1.0 \times 10^{-7}\text{cm}^{-1}$, and $\eta = \pi/4$.

effect of m is to determine how far from the surface both mass functions become effectively identical, i.e. it controls the Vainshtein radius. Both c_3 and c_4 appear to broaden each profile rather than influence the asymptotic observable.

This panel also shows some interesting limiting behavior of the mass functions as one varies the coupling parameters. As $\eta \to \pi/2$, the g-metric in Eq. (2.11) decouples from the auxiliary metric and one recovers the Einstein field equation in GR. Therefore, in this limit, m_g approaches the ADM mass at spatial infinity, $A = M_{\text{ADM}}$. Moreover, in this limit the auxiliary gravitational constant $\mathcal{G} \to \infty$ and the auxiliary Planck mass $M_f^2 \to 0$, recovering GR with an arbitrary decoupled auxiliary metric. On the other hand, in the limit as $\eta \to 0$, the auxiliary gravitational constant $\mathcal{G} \to 0$ and the Plank mass $M_f^2 \to \infty$. In this limit, the auxiliary metric becomes flat from Eq. (2.12) and one recovers dRGT massive gravity. We have indeed been able to replicate the results of [95], where these general metric properties were first presented

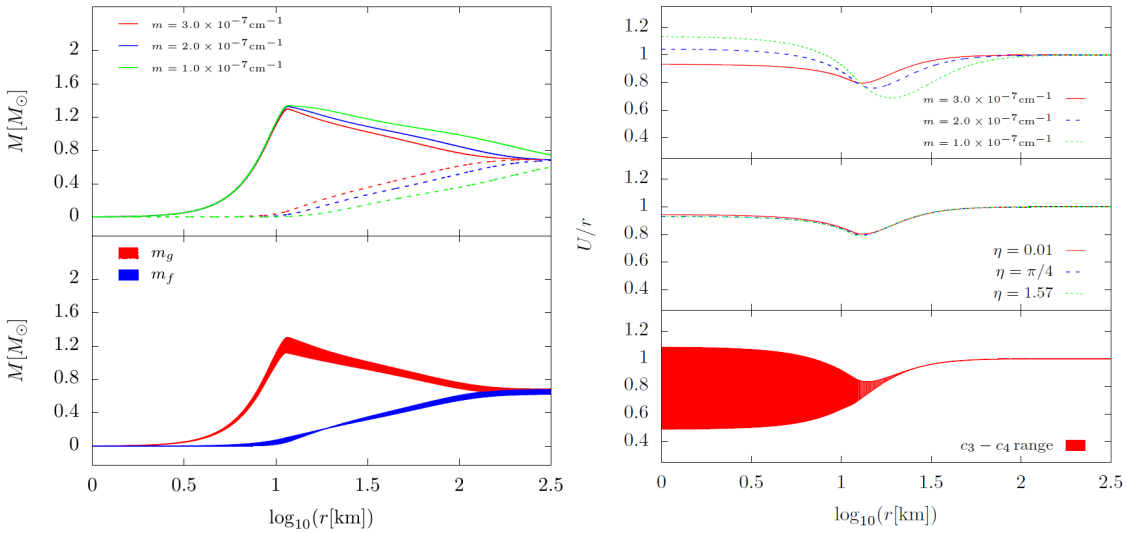

(a) Mass profiles (b) Auxiliary radial coordinate U

Figure 2.4: Numerical solutions at zeroth-order in rotation as a function of radius for different choices of coupling parameters using the APR equation of state. In each subfigure, the parameter denoted in the caption is varied while all remaining parameters are set to a fixed value ($c_3 = 0.48$, $c_4 = 1.71$, $\eta = \pi/4$, $m = 3.0 \times 10^{-7}\mathrm{cm}^{-1}$, $\rho_0 = 7.9 \times 10^{14}\mathrm{g/cm}^3$ where applicable). In the top two subfigures, we vary m and η for fixed (c_3, c_4) through different color lines, while in the bottom subfigure we vary c_3 and c_4 for fixed (m, η) through red or blue shaded regions. Left: Primary, m_g, and auxiliary, m_f, metric mass functions versus r. Outside the star, the primary metric decouples from matter and the mass decreases to some asymptotic value unlike in GR. The parameter η has the largest effect on this asymptotic value, while m only alters the distance away from the stellar surface where both masses become equal, in accordance to the Vainshtein radius. Both c_3 and c_4 only broaden each mass profile curve, and so, they have the smallest effect on the asymptotic mass and radius observables. Right: The auxiliary radial coordinate, U, versus r. Although the variation of α with c_3 and c_4 inside the star is large, this variation quickly approaches its asymptotic value at the surface of the star. Thus, the effect of α is subdominant to matter interactions in the region where it is present and it disappears in the region outside the star where the bimetric interactions dominate.

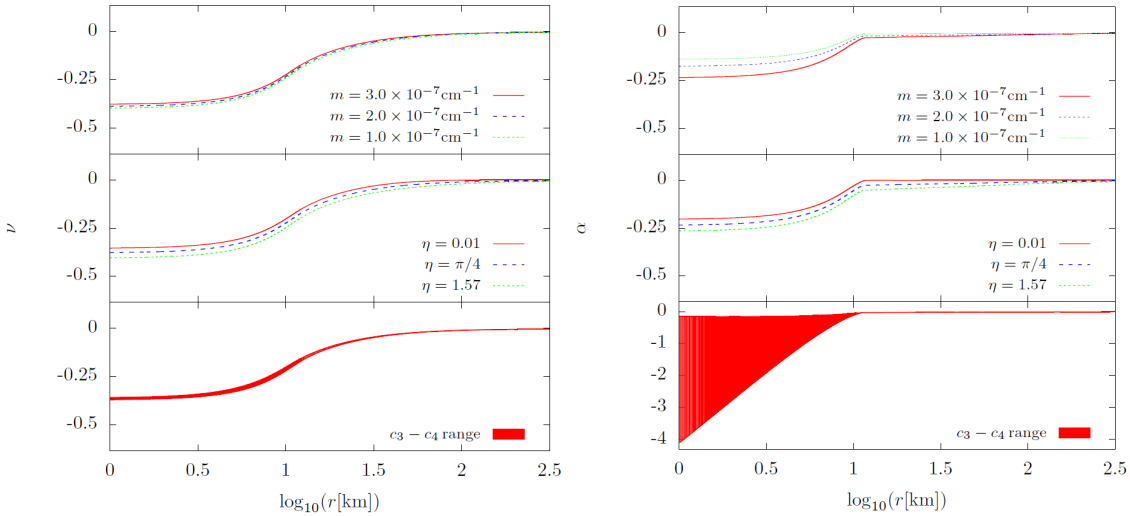

(a) Primary metric function ν (b) Auxiliary metric function α

Figure 2.5: Numerical solutions at zeroth-order in rotation as a function of radius for different choices of coupling parameters using the APR equation of state. In each subfigure, the parameter denoted in the caption is varied while all remaining parameters are set to a fixed value ($c_3 = 0.48$, $c_4 = 1.71$, $\eta = \pi/4$, $m = 3.0 \times 10^{-7}\text{cm}^{-1}$, $\rho_0 = 7.9 \times 10^{14}\text{g/cm}^3$ where applicable). In the top two subfigures, we vary m and η for fixed (c_3, c_4) through different color lines, while in the bottom subfigure we vary c_3 and c_4 for fixed (m, η) through red or blue shaded regions. Left: The primary $(t-t)$ metric function, ν, versus r. In contrast to the m_g and m_f metric functions, the deviation of ν from GR only appears small because of the $1/r$ suppression of ν and α in Eq. (2.37). Right: The auxiliary $(t-t)$ metric function, α, versus r. Although the variation of α with c_3 and c_4 inside the star is large, this variation quickly approaches its asymptotic value at the surface of the star. Thus, the effect of α is subdominant to matter interactions in the region where it is present and it disappears in the region outside the star where the bimetric interactions dominate.

for $c_3 = 0 = c_4$.

The top right panel of Fig. 2.4 shows the auxiliary radial function, U, normalized to the primary radial function, r, as a function of radius. In this case, η has a very small effect, while c_3 and c_4 have a very large impact inside the star. The parameter m has a noticeable influence both inside and outside the star. Since the interactions with the auxiliary metric dominate outside the star where matter vanishes, the parameter m dominates the behavior of U outside the star.

The bottom left panel of Fig. 2.4 shows the $(t-t)$ component function of the primary metric, ν, as a function of radius. The bigravity modifications to ν are much less pronounced than the modifications to the mass m_g. This is because the definition of m_g in Eq. (2.37) introduces a $1/r$ suppression in the metric function itself (λ in this case). Were we to compare the original $(r-r)$ metric function λ (instead of m_g) to the $(t-t)$ component ν, the modification would be similarly less pronounced.

The bottom right panel of Fig. 2.4 shows the auxiliary $(t-t)$ component function, α, as a function of radius. In this case, c_3 and c_4 have a dramatic effect inside the star but this is almost entirely eliminated beyond the surface. This magnified effect inside the star is also evidenced by the sharp jump to its asymptotic value at the surface, shown in the top two portions of this panel. Once the stellar surface is reached, α immediately reaches its expected asymptotic value of 0. This is peculiar because outside the star, absent of any dominant matter effects, the evolution of the system is driven by the interactions with the auxiliary metric. If α does not vary outside the star, then it cannot strongly influence these interactions.

First-Order in Rotation

Local Analysis at $r = 0$ and $r = \infty$ The numerical approach at first-order in spin is identical to that used at zeroth-order. The metric function we solve for is the

first-order frame-dragging function ω. After a Taylor expansion of Eq. (2.48) about $r = 0$ and equating coefficients in powers of r, the behavior of ω at the core of the star is identical to that in GR,

$$\omega_{r\to 0} = \omega_0 - \frac{8\pi}{5} r^2 \left(\rho_0 + p_0\right)\left(\Omega - \omega_0\right) + \mathcal{O}(r^3). \tag{2.60}$$

Just like ρ_0 determines the mass of the star, the constant Ω determines how fast the star is rotating and must be specified before integration. The constant ω_0 must be shot for by requiring the solution to be continuous and differentiable at the stellar surface.

At $r = \infty$ we again cannot choose a simple Taylor expansion. Instead, let us propose a solution of the form

$$\omega_{r\to\infty} = \omega_{\rm GR} + \delta\, \omega_\infty, \tag{2.61}$$

where again $\delta \ll 1$. The resulting equation to $\mathcal{O}(\delta^0)$ is the same as in GR

$$\frac{d^2\omega_{\rm GR}}{dr^2} + \frac{4}{r}\frac{d\omega_{\rm GR}}{dr} = 0, \tag{2.62}$$

whose solution is

$$\omega_{\rm GR} = \Omega - \frac{2J}{r^3}, \tag{2.63}$$

after choosing a proper integration constant and enforcing asymptotic flatness, where J is the spin angular momentum of the rotating star; this must also be shot for by requiring the solution to be continuous and differentiable at the stellar surface. The

equation at $\mathcal{O}(\delta)$ is

$$\frac{d^2\omega_\infty}{dr^2} + \frac{4}{r}\frac{d\omega_\infty}{dr} + \frac{JB\cos^2\eta}{e^{mr}}\left(\frac{m^2}{r^4} - \frac{14m}{r^5} - \frac{14}{r^6}\right). \tag{2.64}$$

Solving the above equation gives

$$\omega_\infty = -JB\cos^2\eta\frac{m^4}{4}\mathrm{Ei}(mr) + \frac{JB\cos^2\eta}{e^{mr}}\left(\frac{m^3}{4r} - \frac{m^2}{4r^2} + \frac{m}{2r^3} - \frac{7}{2r^4}\right), \tag{2.65}$$

where $\mathrm{Ei}(mr)$ is the exponential integral function. After expanding the exponential integral function about $r = \infty$ and combining the result with Eq. (2.63), the behavior of ω as $r \to \infty$ is

$$\omega_{r\to\infty} = \Omega - \frac{2J}{r^3} - \frac{JB\cos^2\eta}{e^{mr}}\left[\frac{2}{r^4} + \frac{6}{mr^5} + \mathcal{O}\left(\frac{1}{r^6}\right)\right]. \tag{2.66}$$

Numerical Solution We can now use these boundary conditions on ω to obtain slowly rotating neutron star solutions. The procedure is identical to that in the non-rotating case. We make an initial guess for ω_0 and J and integrate from the core and from spatial infinity to the surface of the star. Then, we use a two-dimensional Newton-Raphson method to estimate a new guess for ω_0 and J until we find a solution that is continuous and differentiable at the surface to the same tolerance as in the zeroth-order in rotation case. An example is presented in Fig. 2.6 where we show the first-order frame dragging function ω and its derivative. As before, we independently vary m, η, and c_3 and c_4 but we find no noticeable trends from each of these parameters effects.

Once the rotating star is constructed, the moment of inertia can be obtained from the definition,

$$I \equiv \frac{J}{\Omega}. \tag{2.67}$$

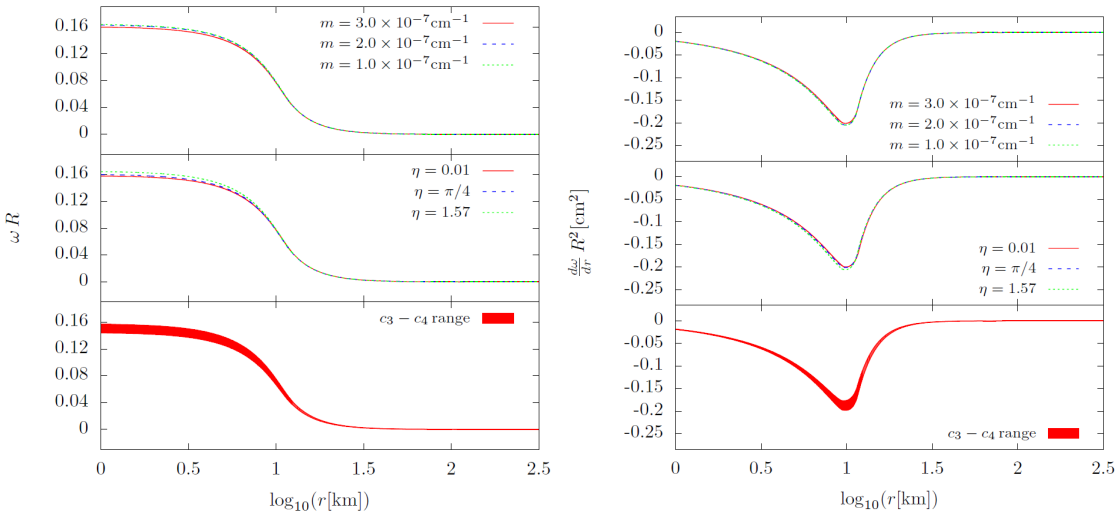

(a) Primary metric function ω (b) Derivative of ω

Figure 2.6: The first-order in rotation functions for both metrics, $\omega\, R$ (left) and $d\omega/dr R^2$ (right), versus radius. The format of this figure is identical to that of Fig. 2.4. All four parameters seem to have a minimal effect on the first-order metric functions, unlike in the zeroth-order in rotation case. Observe that since $\omega = w$ from the symmetry condition in Eq. (2.9) this is the first-order solution for both metrics.

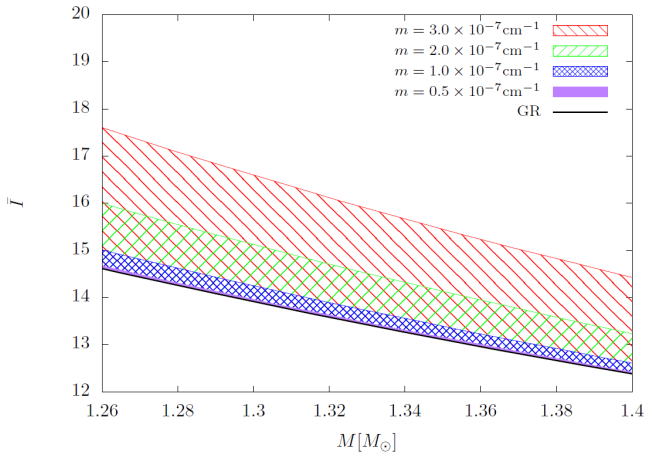

Figure 2.7: Moment of inertia-mass relation with the APR equation of state for various c_3 and c_4. Each shaded region represent families of curves for a fixed value of m and $\eta = \pi/4$. Although the broadening introduced by these couplings scales with m, they remain sub-dominant to variation in η.

For convenience, we also define the dimensionless moment of inertia $\bar{I} \equiv I/M^3$, where M is the mass function of the g-metric evaluated at the stellar surface. Figure 2.7 shows this dimensionless moment of inertia as a function of mass with the APR equation of state for various (c_3, c_4) and m values. Observe that the dimensionless moment of inertia is mostly controlled by m, with (c_3, c_4) introducing a broadening in the curve; the larger m, the larger the broadening effect. With these solutions, we can generate mass-radius and moment-of-inertia-mass relations which are presented and discussed in Section 4.

Conclusions and Future Directions

We have constructed slowly-rotating neutron stars in massive bigravity with various realistic equations of state and a range of coupling parameters. From these solutions, we have explored the mass-radius and the moment-of-inertia-mass relations in some detail. We have found that the bigravity coupling parameters m and η have the strongest impact on these relations, with significant deviations from GR arising when $m > 10^{-7}\text{cm}^{-1}$ and $\eta < \pi/2$. The results obtained here can thus serve as the foundations for an experimental study of bigravity in light of binary pulsar observations and low-mass X-ray binary observations.

The fitting of a timing model to the observation of a sequence of radio pulses from binary pulsars allows one to extract a measure of certain post-Keplerian parameters [79], like the rate of change of the orbital period and the Shapiro time delay parameter. These measurements can then be combined to infer the masses of the binary stars up to a given observational error. For example, for PSR J0737-3039A, fits to the timing model suggest that the primary pulsar PSR J0737-3039A has a mass of $(1.337 \pm 0.0037)M_\odot$ [65]. In a modified gravity theory, the post-Keplerian parameters are not only a function of the masses of the binary components, but also of other

parameters in the theory. Thus, the measurement of more than two post-Keplerian parameters yields a test of GR [37].

In bigravity, we have seen that the mass of an individual star is not constant outside its radius. Rather, the mass function rises inside the star up to the stellar radius and then it *decays* in the exterior spacetime until it approaches a certain asymptotic value. This then means that the gravitational field of a neutron star in its exterior is not simply given by the typical GR parameterization with a constant mass. A proper analysis of binary pulsar data to place constraints on bigravity would then require that (i) one calculate numerically the dependence of the post-Keplerian parameters on the bigravity coupling constants, and then that (ii) one find the set of bigravity parameters and binary masses that are allowed given the measurements of the post-Keplerian parameters from the timing model.

Measurements of quiescent low mass X-ray binaries can also allow one to infer the radius of neutron stars [51]. The pure hydrogen environment of the neutron star surface producing thermal emission can be modeled which, when combined with an inferred mass from the evolution of the post-Keplerian binary parameters, can be used to infer the radius of the neutron star. Such a measurement can eliminate degeneracies introduced by our ignorance of the equation of state of supranuclear matter in mass-radius relations. In bigravity, the decay of the mass function outside the star will introduce a coupling dependence on the thermal emission models when carrying out the fits to the data.

An extended and precise observation of relativistic binary pulsars may also allow the extraction of the moment of inertia of the stars. This comes about because the timing model is sensitive to the orbital motion of the stars, and the latter depends on the spin angular momentum of the binary components due to spin-orbit precession. Future observations of PSR J0737-3039 may allow for a measurement of the moment

of inertia of the primary pulsar to 10% [62]. If such a future measurement is possible, then one could draw an error ellipse in the moment of inertia-mass plane. In GR, this error ellipse will provide a measure of the equation of state of the neutron star. In bigravity, the error ellipse will place a combined constraint on the equation of state and the coupling parameters of the modified theory.

In addition to the extensions and applications discussed above, another possibility is to consider whether combined gravitational wave and binary pulsar observations can allow for stronger constraints on bigravity. This could be achieved by using the approximately universal relations between the moment of inertia of neutron stars and their Love number found recently in GR [100, 101, 102]. Such tests of bigravity would require the construction of such universal relations in this modified theory, which in turn would require the calculation of neutron stars to second-order in a slow-rotation expansion.

A different avenue to explore is to consider the stability of the stellar solutions found here. This would require the study of perturbations of the numerical solution, which in turn would require the linearization of the modified field equations about these numerical background and an eigenmode analysis for the frequencies of the perturbations. Such an analysis is interesting because of the possibility of super-radiant instabilities in rotating solutions. Indeed, modified theories of gravity with massive fields tend to introduce a potential barrier to perturbations, which then source a super-radiant instability that destroys what at first appears as stationary axisymmetric solutions. If this is the case for massive bigravity for all values of the coupling parameters, then serious doubt would be cast on the theoretical viability of the theory.

Acknowledgments

N.Y. thanks the hospitality of the Yukawa Institute for Theoretical Physics, where this project was started. We thank Takahiro Tanaka, Paolo Pani, Thomas Sotiriou, and Fawad Hassan, for helpful discussions and comments. We are also grateful for the computational support of the Hyalite High-Performance Computing System, operated and supported by University Information Technology Research Cyberinfrastructure at Montana State University. N.Y. acknowledges support from the NSF CAREER grant PHY-1250636 and NASA grant NNX16AB98G.

NUMERICAL BLACK HOLE SOLUTIONS IN MODIFIED GRAVITY THEORIES: SPHERICAL SYMMETRY CASE

Contribution of Authors and Co-Authors

Manuscript in Chapter 3

Author: Andrew Sullivan

Contributions: Performed mathematical analysis of problem, compared results, and wrote the manuscript.

Co-Author: Nicolás Yunes

Contributions: Thought of the problem, helped find errors in the code, helped interpret results, discussed implications, and edited manuscripts.

Co-Author: Thomas Sotiriou

Contributions: Thought of the problem, helped find errors in the code, helped interpret results, discussed implications, and edited manuscripts.

Manuscript Information Page

Andrew Sullivan, Nicolás Yunes, and Thomas Sotiriou

Physical Review D

Status of Manuscript:

_____Prepared for submission to a peer-reviewed journal

_____Officially submitted to a peer-reviewed journal

_____Accepted by a peer-reviewed journal

__X__Published in a peer-reviewed journal

Published by: APS Physics

In Volume 101, Issue 4, 13 February 2020

DOI: 10.1103/PhysRevD.101.044024

Abstract

Detailed observations of phenomena involving black holes, be it via gravitational waves or more traditional electromagnetic means, can probe the strong field regime of the gravitational interaction. The prediction of features in such observations requires detailed knowledge of the black hole spacetime, both within and outside of General Relativity. We present here a new numerical code that can be used to obtain stationary solutions that describe black hole spacetimes in a wide class of modified theories of gravity. The code makes use of a relaxed Newton-Raphson method to solve the discretized field equations with a Newton's polynomial finite difference scheme. We test and validate this code by considering static and spherically symmetric black holes both in General Relativity, as well as in scalar-Gauss-Bonnet gravity with a linear (linear scalar-Gauss-Bonnet) and an exponential (Einstein-dilaton-Gauss-Bonnet) coupling. As a by-product of the latter, we find that analytic solutions obtained in the small coupling approximation are in excellent agreement with our fully non-linear solutions when using a linear coupling. As expected, differences arise when using an exponential coupling. We then use these numerical solutions to construct a fitted analytical model, which we then use to calculate physical observables such as the innermost stable circular orbit and photon sphere and compare them to the numerical results. This code lays the foundation for more detailed calculations of black hole observables that can be compared with data in the future.

Introduction

The recent discovery of gravitational waves [1, 2, 3, 4, 5, 6] has inaugurated a new era of multi-messenger astrophysics that opens up an entirely new avenue to test Einstein's theory of General Relativity (GR) in the extreme gravity regime [103]. GR

is thus far in excellent agreement with experiments and observations. However, this statement does rely on the assumption that dark matter or dark energy do not signal a deviation from GR. Moreover, GR has so far resisted quantisation attempts. These considerations have provided motivation for exploring modified theories of gravity.

Unsurprisingly, modified theories typically increase the complexity of the field equations to such a degree that the calculation of observable predictions becomes incredibly difficult and sometimes even seemingly impossible if working analytically. Historically, experimental tests that probe the weak-field regime prompted the calculation of solutions and observables through perturbation theory [97], and more recently, this has been further justified through effective field theory arguments [28, 29, 35]. A by-product of assuming that GR modifications are small relative to GR predictions is that analytical calculations become tractable again. But once one begins to probe the extreme gravity regime, perturbative techniques need not be well-justified, as they typically eliminate strong-field instabilities that could have observational consequences. The typical example of this is spontaneous scalarization, a process through which large modifications to GR arise in a class of scalar-tensor theories when considering non-linear solutions for neutron stars above a certain compactness [39, 81] or black holes within a certain mass range [45, 86].

The need for more precise solutions and observable predictions without the use of perturbation theory then becomes clear, and we here take steps in this direction. We present a numerical infrastructure to produce exact solutions that describe stationary black holes in a wide class of modified theories of gravity. This paper focuses on describing the numerical setup and applying it in the simplest case of spherically symmetric solutions that can act as a benchmark. By "exact" we mean solutions obtained numerically and without the use of perturbative techniques, including small coupling expansions. The code is computationally efficient, converging to an answer

of prescribed accuracy within only a few iterations, and thus allowing for calculations in laptop-class computers. We validate this infrastructure against known analytic solutions in General Relativity, as well as in a specific member of the class of modified theories to which this infrastructure is applicable.

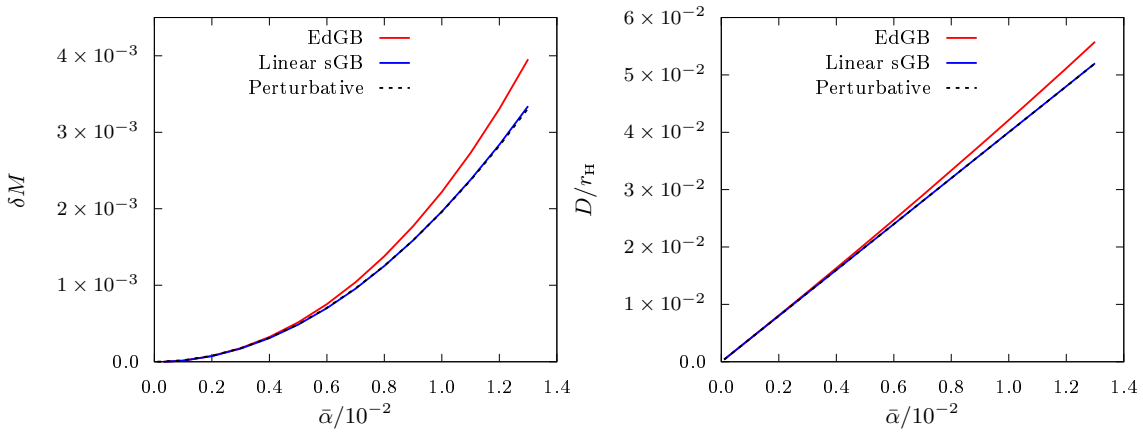

(a) Mass correction (b) Scalar charge

Figure 3.1: Relative fractional correction to the ADM mass (left) and the dimensionless scalar monopole charge as a function of the dimensionless sGB coupling parameter $\bar{\alpha}$. The solid red and blue lines correspond to our numerical solutions using an exponential coupling (EdGB) and a linear coupling (linear sGB) respectively, while the black dashed line corresponds to the analytical perturbative solution. Observe that the perturbative approximation agrees very well with both solutions for small $\bar{\alpha}$, and in fact, it agrees well with the numerical linear sGB solution for *all* $\bar{\alpha}$ explored. However, the perturbative approximation differs from the numerical EdGB solution for $\bar{\alpha} \gtrsim 10^{-3}$, showing the breakage of the small-coupling approximation.

The basic problem our numerical infrastructure solves is that of finding the solution to an elliptic system of nonlinear and coupled differential equations. The typical approach to solve this problem numerically is to discretize the differential equations through a finite difference scheme. This leads to a residual error on the solution of the system of equations that one wishes to minimize. Our algorithm employs a Newton polynomial method to discretize the equations, which appropriately

allows for an easier analytical evaluation of the Jacobian of the system. By minimizing the residual, we can then iteratively converge to the true solution using a root-finding algorithm, such as the Newton-Raphson method. Our code uses an additional relaxation factor to improve convergence, as well as compactified coordinates to properly set boundary conditions, and adaptive mesh refinement near the boundaries. With all of this machinery, our code typically converges to the user prescribed tolerance in 1–3 iterations.

After constructing this numerical infrastructure, we implement it in a few different scenarios. We begin by validating the algorithm through a simple toy problem whose analytic solution is known, and then through the calculation of the Schwarzschild solution in GR. Since in both cases an analytic solution is known, we can easily compare it to our numerical solutions point-wise in the entire domain. We find that our code converges to the correct (analytically known) solution in one and three iterations respectively to within the tolerance we specified.

With the validation complete, we then construct stationary and spherically symmetric black hole solutions in scalar-Gauss-Bonnet (sGB) gravity, a well motivated modified theory that is a member of the quadratic gravity class [20, 24, 103]. Ours is of course not the first study of compact objects in sGB gravity. Mathematically, the theory evades the no-hair theorems of GR, allowing black holes to have non-trivial scalar hair [30, 58, 68, 87, 88, 104], while preventing neutron stars from having a monopole scalar charge [99], thus making it extremely difficult to place constraints with binary pulsar observations.

Compact objects in scalar-Gauss-Bonnet gravity are typically studied under two forms of the action which depend on the coupling function between the massless scalar field and the Gauss-Bonnet invariant. When the scalar field is coupled through an exponential to the Gauss-Bonnet invariant this is commonly referred to as Einstein-

dilaton-Gauss-Bonnet (EdGB) gravity. In the regime where the scalar field is small, one can approximate the exponential as a linear coupling to the Gauss-Bonnet invariant which is commonly referred to as the linear scalar-Gauss-Bonnet gravity. This is the terminology that will be used throughout this paper namely: 'linear sGB' to refer to the linear coupling function and 'EdGB' to refer to the exponential coupling function.

Stationary black holes have been found in linear sGB analytically using the small coupling limit approximation, both in spherical symmetry [87, 88, 104] and in axisymmetry using a slow-rotation approximation [15, 30, 66, 69, 72]. Reference [88] also studied numerical non-perturbative spherically symmetric black holes in linear sGB. In EdGB, numerical solutions are known in spherical symmetry [10, 52, 58, 71, 92] and in axisymmetry [60], but typically these numerical solutions are obtained from a proprietary code that has not been tested for black hole problems of this kind. It is also worth mentioning that, dynamical evolution of black holes and binaries in sGB gravity has also received attention recently [22, 23, 78, 98].

Our numerical infrastructure is general enough to allow the tackling of any coupling function between the massless dilaton and the Gauss-Bonnet term in the action, and we here explore both the linear sGB and EdGB coupling functions. In the linear case, we find that the exact numerical solution agrees spectacularly well with the perturbative analytic solution that assumes weak-coupling, while differences arise in the exponential coupling case for large enough coupling. An example of this is shown in Fig. 3.1, where we present the relative fractional correction to the ADM mass (left) and the scalar monopole charge (right) as a function of the dimensionless sGB coupling parameter $\bar{\alpha} = \alpha/r_{\rm H}^2$. Although the differences between the EdGB and linear sGB solutions appears large for large $\bar{\alpha}$, the deviation is actually only appreciable near the horizon, as we will show later.

With these exact numerical solutions at hand, we construct analytical fitted models to allow for the rapid computation of physical observables, such as the location of the innermost stable circular orbit (ISCO) and the light ring. The fitting coefficients are available online though we provide a few examples in Appendix C. Figure 3.2 shows the fractional change in the location of the ISCO (left) and the light ring (right). We again find comparatively very good agreement between the analytic perturbative result and the exact numerical result of linear sGB for all $\bar{\alpha}$s considered, and some disagreement with the exact numerical result of EdGB for large $\bar{\alpha}$. Observe also that the observables computed with the exact numerical solution agree extremely well with those computed with our analytical fitted models.

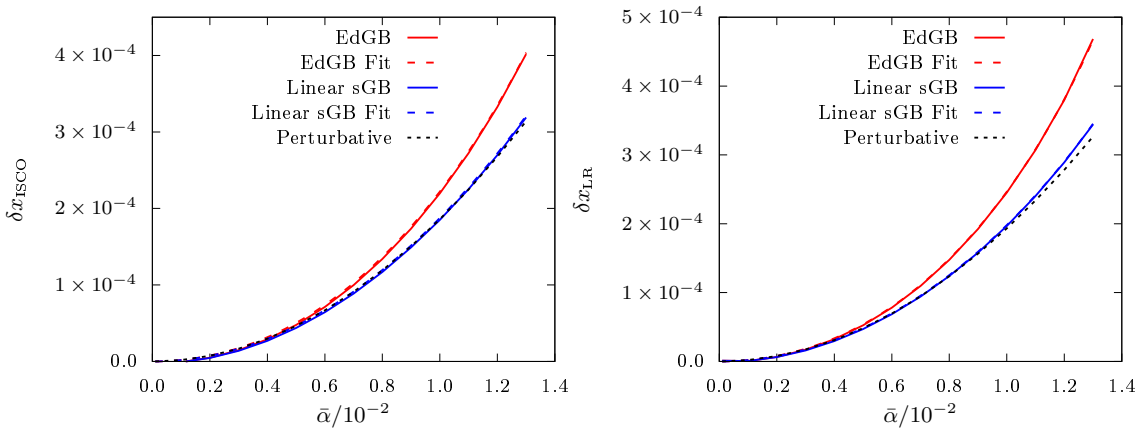

(a) Innermost stable circular orbit (b) Light ring

Figure 3.2: Relative fractional correction to the location of the innermost stable circular orbit (left) and the light ring (right). The red and blue lines correspond to these observables computed for EdGB or linear sGB respectively. The solid lines correspond to the observables computed with our exact numerical solution, the dashed lines use our analytical fitted model, and the black dotted lines use the analytical perturbative solution to linear order in the coupling.

Our paper differs from previous work in that its goal is not to study a particular theory of gravity, but rather to develop a computational infrastructure that is (i)

free and open to the public, (ii) computationally accurate and efficient, (iii) taylor-made for finding black hole solutions in modified theories of gravity with vector or scalar non-minimal couplings, and (iv) able to provide enough accurate data to compute analytical fitted models. The algorithm presented here applies to spherically symmetric scenarios, but extensions to axisymmetry are straightforward and under way. The algorithm developed here can thus be used to calculate certain astrophysical observables, such as electromagnetic emission of accretion disks around black holes [8], shadows of black holes [16], or quasinormal modes of black hole mergers [25] on the fly and with high precision, allowing for realistic data analysis investigations with Bayesian methods.

The remainder of this paper is organized as follows. Section 4 briefly outlines the numerical algorithm. Section 4 validates the algorithm through a simple toy problem and a Schwarzschild black hole. Section 4 applies the algorithm to sGB gravity and derives the results described above. Section 4 constructs a fitted analytical model from the numerical solutions and compares physical observables determined by the numerical solutions and the fits. Finally, Section 4 summarizes our results and points to future directions. For the remainder of this paper we use the following conventions: Greek letters denote spacetime indices; the metric has the spacetime signature $(-,+,+,+)$; we use geometric units where $G = 1 = c$.

Numerical Methods

Our numerical infrastructure extends the method presented in [83] to build a partial differential equation solver that finds exact black hole solutions in an arbitrary modified theory of gravity. A brief overview is described here with a more in-depth application to a general system of equations in Appendix B. The algorithm is split into three main parts: the relaxed Newton-Raphson method, the discretization method,

and the discretization error estimation.

The Newton-Raphson method is a root-finding algorithm that iteratively solves for the approximate zeros of a single-valued real function by calculating the x-intercept of the tangent line at points sufficiently close to the roots. It can be easily generalized to multiple dimensions as shown in App. B which outlines the application to a general function in the continuum limit. The discretization method employs a Newton interpolation polynomial (See App. B) to provide a continuous local representation of a discrete function which is utilized to discretize the partial differential equations on a finite grid. The discretization naturally introduces errors which are estimated by exploiting the difference between higher order Newton polynomials shown in App. B. These discretization errors must then be controlled by ensuring the correction on the solution due to these errors are below a specified tolerance detailed in App. B. With the errors under control, we carry out the Newton-Raphson iterations with a relaxation factor until we have sufficiently converged to the desired solution. In the next section, we will validate this numerical infrastructure with a simple ordinary differential equations and then the Schwarzschild solution in GR.

Validation

In this section we describe the steps we have taken to validate our algorithm. We first consider a simple ordinary differential equation. This toy problem is a useful example to demonstrate the structure of the Jacobian and to describe the detailed steps involved in applying the Newton-Raphson method. We then move on to GR and consider static, spherically symmetric vacuum solutions to the Einstein equations. This demonstrates how the algorithm handles nonlinear coupled ordinary differential equations that represent black holes with coordinate singularities at the location of the horizon.

Toy Problem

Consider a simple second order ordinary differential equation in the operator notation of Eq. (B.1)

$$\mathcal{D}u^* = \left[\frac{d^2}{dx^2} + 2\frac{d}{dx} + 1\right] u^* = 0. \tag{3.1}$$

The general solution to this differential equation can be found analytically to be

$$u^*(x) = c_1 e^{-x} + c_2 x e^{-x}. \tag{3.2}$$

If we choose the boundary conditions, $u^*(0) = 1$ and $u^*(1) = 0$, the solution becomes

$$u^*(x) = e^{-x} - x e^{-x}. \tag{3.3}$$

Let us now apply our computational infrastructure to this simple problem. The system is a single ordinary differential equation (M=1) that we wish to solve on a uniform discretized grid of $N = 101$ points. Let us choose the following initial guess for our generic vector u:

$$u^{(0)}(x) = 1 - x, \tag{3.4}$$

where the superscript (0) stands for the iteration number, i.e. the initial guess is the $n = 0$ iteration. The residual vector b on the right-hand side of Eq.(B.2) can be analytically evaluated to

$$b^{(0)} = \mathcal{D}u^{(0)} = -1 - x, \tag{3.5}$$

which clearly does not vanish anywhere in the x domain, i.e. in $x \in [0, 1]$.

Since the residual does not vanish, we must correct the initial guess by some amount Δu in the next (first) iteration. In order to find this correction, however, we

must first find a discrete representation of $u(x)$ in terms of a Newton polynomial on a uniform grid at points $\{x_i\}$ with $i \in [0, 100]$. For this toy problem, we pick a Newton polynomial of order $r = 2$, and use a centralized stencil $s_j = (I, I+1, I-1)$, where I is the counter of the element x_I that is closest to the value of x. With this at hand, Eq. (B.20) yields

$$u_d(x) = u_{s_0} w_{s_0,s_0} P_{s_0}(x) + \sum_{k=0}^{1} u_{s_k} w_{s_k,s_1} P_{s_1}(x) + \sum_{k=0}^{2} u_{s_k} w_{s_k,s_2} P_{s_2}(x). \tag{3.6}$$

The basis $P_{s_j}(x)$ is defined in Eq. (B.22), and since the order of the polynomial here is $r = 2$, the only basis that contribute are

$$\begin{aligned} P_{s_0} &= 1\,, \qquad P_{s_1} = (x - x_{s_0})\,, \\ P_{s_2} &= (x - x_{s_0})\,(x - x_{s_1})\,. \end{aligned} \tag{3.7}$$

The coefficients $u_{s_i} = u^{(n)}(x_{s_i})$, while the weighting factors that contribute at this polynomial order are

$$\begin{aligned} w_{s_0,s_0} &= 1\,, \\ w_{s_0,s_1} &= (x_{s_0} - x_{s_1})^{-1}\,, \\ w_{s_1,s_1} &= (x_{s_1} - x_{s_0})^{-1}\,, \\ w_{s_0,s_2} &= [(x_{s_0} - x_{s_1})\,(x_{s_0} - x_{s_2})]^{-1}\,, \\ w_{s_1,s_2} &= [(x_{s_1} - x_{s_0})\,(x_{s_1} - x_{s_2})]^{-1}\,, \\ w_{s_2,s_2} &= [(x_{s_2} - x_{s_0})\,(x_{s_2} - x_{s_1})]^{-1}\,. \end{aligned} \tag{3.8}$$

Putting all of this together, we then have the discrete representation of $u(x)$ shown below in Eq. (3.10).

The Newton polynomial representation of order $r = 2$ is the second-order, discrete Taylor expansion of the function about the point $x = x_I$. In practice, the only values that x can take are in the set $\{x_i\}$. Since this is a closed-form representation of the u as a function of x, we can evaluate the function and all derivatives at a point x_i straightforwardly

$$\begin{aligned} u_d(x_i) &= u^{(n)}(x_I), \\ \partial_x u_d(x_i) &= \frac{u^{(n)}(x_{I+1}) - u^{(n)}(x_{I-1})}{2\Delta x}, \\ \partial_{xx} u_d(x_i) &= \frac{u^{(n)}(x_{I+1}) - 2u^{(n)}(x_I) + u^{(n)}(x_{I-1})}{\Delta x^2}, \end{aligned} \tag{3.9}$$

where $\Delta x = x_{I+1} - x_I = x_I - x_{I-1}$, as must be the case since Eq. (3.10) is a discrete Taylor expansion.

$$\begin{aligned} u_d(x) = u^{(n)}(x_I) &+ \left[\frac{u^{(n)}(x_I)}{x_I - x_{I+1}} + \frac{u^{(n)}(x_{I+1})}{x_{I+1} - x_I}\right](x - x_I) \\ &+ \left[\frac{u^{(n)}(x_I)}{(x_I - x_{I+1})(x_I - x_{I-1})} + \frac{u^{(n)}(x_{I+1})}{(x_{I+1} - x_I)(x_{I+1} - x_{I-1})} + \frac{u^{(n)}(x_{I-1})}{(x_{I-1} - x_I)(x_{I-1} - x_{I+1})}\right] \\ &\times (x - x_I)(x - x_{I+1}). \end{aligned} \tag{3.10}$$

With this representation, we can now evaluate the discretized residual b_d, which is simply given by

$$b_d(x_i) = \mathcal{D} u_d(x_i). \tag{3.11}$$

Using the above expressions for the analytic derivatives of the discretized function u,

we then have that for the discretized residual at iteration n

$$b_d^{(n)}(x_i) = \frac{u^{(n)}(x_{I+1}) - 2u^{(n)}(x_I) + u^{(n)}(x_{I-1})}{\Delta x^2} + 2\frac{u^{(n)}(x_{I+1}) - u^{(n)}(x_{I-1})}{2\Delta x} + u^{(n)}(x_I), \tag{3.12}$$

and at the boundaries

$$\begin{aligned} b_d^{(n)}(x_0) &= u^{(n)}(x_0) - 1, \\ b_d^{(n)}(x_{100}) &= u^{(n)}(x_{100}) - 0. \end{aligned} \tag{3.13}$$

With the discretized residual, we can now evaluate the Jacobian. From Eq. (B.43), we have that

$$J_{i,j} = \frac{\partial b_d^{(n)}(x_i)}{\partial u^{(n)}(x_j)} \tag{3.14}$$

in our toy problem, whose only non-vanishing components are

$$\begin{aligned} J_{0,0} &= 1, \\ J_{I,I-1} &= \frac{1}{\Delta x^2} - \frac{1}{\Delta x}, \\ J_{I,I} &= -\frac{2}{\Delta x^2} + 1, \\ J_{I,I+1} &= \frac{1}{\Delta x^2} + \frac{1}{\Delta x}, \\ J_{100,100} &= 1, \end{aligned} \tag{3.15}$$

which is a tridiagonal matrix. Given this, the discretization error calculated from Eq. (B.37) is

$$\begin{aligned} D_e(x_i) = 2 &\left(\frac{u^{(n)}(x_{I+1}) - u^{(n)}(x_{I-1})}{6\Delta x} - \frac{u^{(n)}(x_{I+2}) - u^{(n)}(x_{I-2})}{12\Delta x} \right) \\ &- \frac{u^{(n)}(x_I)}{2\Delta x^2} + \frac{u^{(n)}(x_{I+1}) + u^{(n)}(x_{I-1})}{3\Delta x^2} - \frac{u^{(n)}(x_{I+2}) + u^{(n)}(x_{I-2})}{12\Delta x^2}, \end{aligned} \tag{3.16}$$

with a slightly modified formula near the boundary.

With all of these quantities calculated, we now apply the Newton-Raphson method to invert Eq. (B.43). Let us then return to vector notation and re-introduce

$$b_{d,i}^{(n)} := b_d^{(n)}(x_i)\,, \qquad \Delta u_{d,i}^{(n)} := \Delta u_d^{(n)}(x_i)\,, \tag{3.17}$$

such that Eq. (B.43) becomes

$$J_{i,j}^{(n)} \Delta u_{d,i}^{(n)} = -b_{d,i}^{(n)}. \tag{3.18}$$

The inversion of this equation then yields the correction to our nth solution, namely $u_{d,i}^{(n+1)} = u_{d,i}^{(n)} + \Delta u_{d,i}^{(n)}$. Applying this algorithm, we find that our computational infrastructure converges to the tolerance required in a single iteration. In fact, after a single iteration, $\|b_{d,i}\| \approx \mathcal{O}\left(10^{-12}\right)$ even after only requiring the tolerance of Eq. (B.49). Although the algorithm efficiently minimizes the residual of the system, the residual does not directly correlate with the error between the numerical solution and the exact solution. This is due to the additional errors that are introduced during the discretization procedure described in Sec. B. Therefore, the "true" error between the numerical solution and the exact solution is determined by a combination of the discretized residual and the discretization error.

In this toy problem, although the residual was minimized to $\mathcal{O}(10^{-12})$, the relative discretization error is still $\mathcal{O}(10^{-5})$ from Eq. (B.41), so the "true" error after 1 iteration is still limited to $\mathcal{O}(10^{-5})$ (see the bottom left panel of Fig. 3.3). This implies that even though the residual converges far below our desired tolerance, the "true" error is only just below the desired tolerance because the "true" error is also indirectly influenced by the discretization error. The solution, error, and the residual are shown in Fig. 3.3.

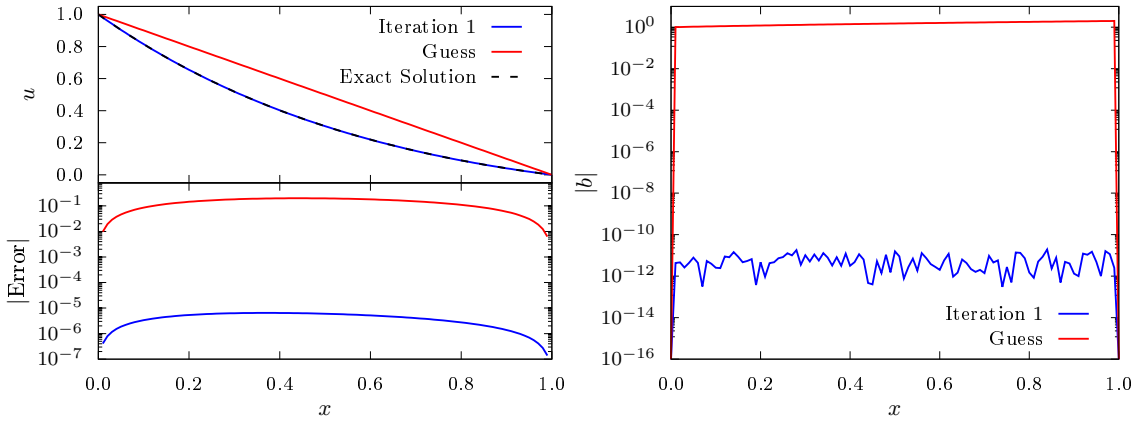

(a) Solution error (b) Residual

Figure 3.3: Numerical solution to the toy problem (top left), true error between numerical and exact solution (bottom left), and residual (right). The red line, blue line, and black dashed line is the initial guess, the numerical solution after 1 iteration, and the exact solution respectively. Observe how the residual drops to 10^{-12} after the first iteration, even though the required tolerance was set to only 10^{-5}. Observe also the discrepancy between the true error and the residual after 1 iteration.

Schwarzschild Black Hole

In the previous section we solved a simple ordinary differential equation using the method described in Sec. 4. We would now like to apply it to solving the elliptic differential equations that arise from the vacuum Einstein equations in spherical symmetry and stationarity. The solution is the well-known Schwarzschild metric to which we can compare our numerical results. We therefore use this example as a benchmark of the performance of our algorithm.

The Einstein-Hilbert action in General Relativity in a vacuum is given by

$$S = \frac{1}{16\pi} \int d^4x \sqrt{-g}\, R, \tag{3.19}$$

where R is the Ricci scalar and g is the determinant of the metric $g_{\mu\nu}$. Varying the

action with respect to the metric gives the vacuum Einstein field equations

$$G_{\mu\nu} = 0\,, \tag{3.20}$$

where $G_{\mu\nu}$ is the Einstein tensor.

Let us now consider a spherically symmetric and stationary metric ansatz in isotropic coordinates

$$ds^2 = -f(\rho)\,dt^2 + m(\rho)\left[d\rho^2 + \rho^2 d\Omega^2\right], \tag{3.21}$$

where ρ is the isotropic radial coordinate, which is related to the Schwarzschild radial coordinate by

$$r = \rho[1 + r_{\rm H}/(4\rho)]^2\,, \tag{3.22}$$

where $r_{\rm H} = 2M_0$ is the horizon radius in Schwarzschild coordinates and M_0 is the mass.

With this ansatz, the coupled system of ($M = 2$ in our computational infrastructure notation) differential equations that we wish to solve can be found from the (t,t) and (ρ,ρ) components of the Einstein tensor. These components are

$$G_{tt} = -\frac{f\,m''}{m^2} + \frac{3f\,(m')^2}{4m^3} - \frac{2f\,m'}{\rho\,m^2}, \tag{3.23}$$

$$G_{\rho\rho} = \frac{(m')^2}{4m^2} + \frac{m'f'}{2fm} + \frac{m'}{\rho\,m} + \frac{f'}{\rho\,f}, \tag{3.24}$$

with primes standing for radial derivatives.

The Schwarzschild solution to these equations in these coordinates is

$$f_{\rm GR} = \left(\frac{1-\frac{r_{\rm H}}{4\rho}}{1+\frac{r_{\rm H}}{4\rho}}\right)^2, \qquad m_{\rm GR} = \left(1+\frac{r_{\rm H}}{4\rho}\right)^4. \tag{3.25}$$

The event horizon in isotropic coordinates is located at $\rho = \rho_{\rm H} = r_{\rm H}/4$, as found from the condition $g_{tt}|_{\rho=\rho_{\rm H}} = f_{\rm GR}|_{\rho=\rho_{\rm H}} = 0$.

The boundary conditions at the event horizon and at spatial infinity are determined by regularity and smoothness. At the event horizon we must have

$$f_{\rm GR}|_{\rho=\rho_{\rm H}} = 0, \qquad m_{\rm GR}|_{\rho=\rho_{\rm H}} = 16, \tag{3.26}$$

which follows from evaluation of the analytic solution at $\rho = \rho_{\rm H}$. At spatial infinity, asymptotic flatness requires that

$$f_{\rm GR}|_{\rho\to\infty} = 1, \qquad m_{\rm GR}|_{\rho\to\infty} = 1. \tag{3.27}$$

Our computational infrastructure allows us to not only find the numerical solution to Eq. (4.12), but also to find some observable global quantities that characterize the black hole spacetime. Asymptotically near spatial infinity, the leading order terms of the fields decay as

$$\begin{aligned} f_{\rm GR} &= 1 - \frac{2M}{\rho} + \mathcal{O}\left(\frac{1}{\rho^2}\right), \\ m_{\rm GR} &= 1 + \frac{2M}{\rho} + \mathcal{O}\left(\frac{1}{\rho^2}\right), \end{aligned} \tag{3.28}$$

where M is the Arnowit-Deser-Misner (ADM) mass. Therefore, the ADM mass can be found from the coefficient of the $1/\rho$ expansion of the numerical solution near spatial infinity. Because of the high Newton polynomial order we use, we can interpolate our numerical solutions very close to spatial infinity to a high degree of accuracy, which allows us to extract the ADM mass from our numerical solutions easily.

The extraction of the ADM mass and the imposition of boundary conditions becomes more precise through the use of a compactified coordinate. We therefore

introduce the coordinate x, defined by

$$x = \frac{1 - r_{\rm H}/4\rho}{1 + r_{\rm H}/4\rho}, \tag{3.29}$$

and perform a coordinate transformation prior to solving our differential system. This changes our domain of integration from $\rho \in [r_{\rm H}/4, \infty)$ to the finite domain $x \in [0, 1]$. In these compactified isotropic coordinates, the Schwarzschild solution has the form

$$f_{\rm GR} = x^2, \qquad m_{\rm GR} = \frac{16}{(1+x)^4}. \tag{3.30}$$

With the differential system in compactified coordinates, we then solve the problem numerically as specified in Sec. 4. We begin by replacing each function and differential operator with a discretized Newton polynomial representation of order $r = 12$ on a grid of $N = 101$ points. We then initialize the numerical solver with a initial guess that is a small perturbation away from the Schwarzschild metric and that vanishes at the boundaries[1]

$$\begin{aligned} u_0^{(0)} &= f_{\rm GR}\left[1 + \delta\ x\ (1-x)\right], \\ u_1^{(0)} &= m_{\rm GR}\left[1 + \delta\ x\ (1-x)\right], \end{aligned} \tag{3.31}$$

where $\delta = 0.1$. One can adjust δ to improve or worsen the initial guess, which in turn affects the number of iterations required to converge to a solution within the tolerance required.

Applying this algorithm, we find that our computational infrastructure converges to the desired tolerance in 3 iterations. The number of iterations is related to the initial guess, which in this case is controlled by the value of δ. In the limit as $\delta \to 0$

[1]For this toy problem, we know the exact analytic solution *a priori*, so we could initialize our solver with it. Doing so, however, would prevent us from validating our computational infrastructure.

the initial guess becomes the exact solution, and the initial residual decreases below tolerance to within numerical precision.

Unlike in the toy problem from the previous section, the "true" error between the numerical solution and the exact solution is now of comparable order to the residual $\mathcal{O}(10^{-12})$. This is due to the closed polynomial form of the Schwarzschild solution in compactified isotropic coordinates, which are very well approximated by our Newton polynomial. The comparison between the toy problem and the Schwarzschild application suggests that in problems where we do not have the exact solution to compute the "true" error we cannot use the residual as a direct measure of the error. In other words, even if we have a minimized residual far below the desired tolerance, the solution must be assumed to only be accurate to the desired tolerance. The numerical solution and residuals are shown in Fig. 3.4.

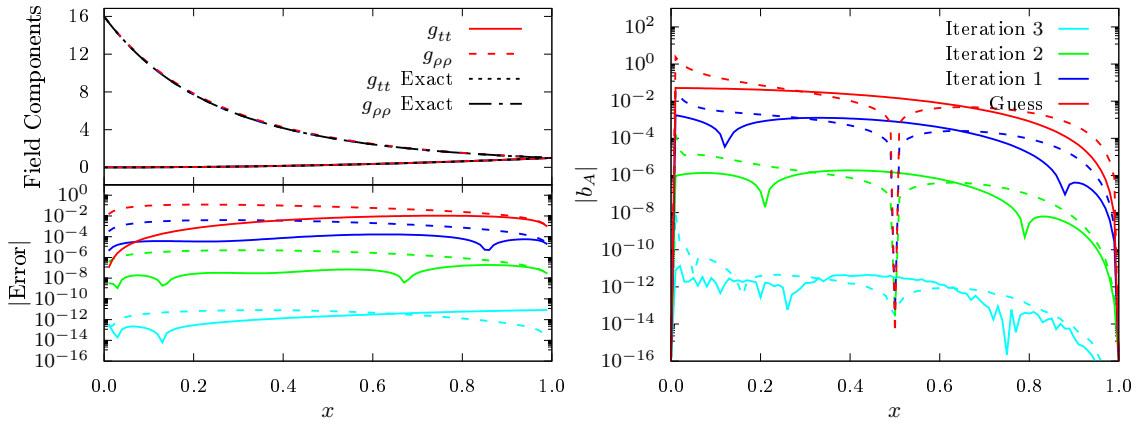

(a) Solution error (b) Residual

Figure 3.4: Numerical solution (top left), error between the numerical solution and the exact solution (bottom left), and residual (right) per iteration for the vacuum Einstein equations in spherical symmetry. The solid and dashed lines indicate the g_{tt} and $g_{\rho\rho}$ component of the metric respectively. Different colors indicate iteration number. Observe that the numerical solution converges to the Schwarzschild metric within three iterations and that the residual does closely mirror the error in this example.

Spherically Symmetric Black Holes in Scalar-Gauss-Bonnet Gravity

In this section we solve the modified Einstein field equations in sGB gravity with both a linear coupling and an exponential coupling function, assuming a vacuum spacetime that is also spherical symmetric and stationary.

Action and Field equations

The action in scalar-Gauss-Bonnet gravity in a vacuum is given by

$$S = \frac{1}{16\pi}\int d^4x\sqrt{-g}\left[R - \beta\,\nabla_\mu\psi\nabla^\mu\psi + 2\,\alpha F(\psi)\mathcal{G}\right], \tag{3.32}$$

where R is the Ricci scalar and g is the determinant of the metric $g_{\mu\nu}$. The real dimensionless scalar field ψ is coupled through a coupling constant α which has dimensions of length squared and a function of the scalar field $F(\psi)$ to the Gauss-Bonnet invariant $\mathcal{G}$

$$\mathcal{G} = R^2 - 4R^{\mu\nu}R_{\mu\nu} + R^{\mu\nu\rho\sigma}R_{\mu\nu\rho\sigma}. \tag{3.33}$$

We keep the coupling constant β around in this section, but in all computation we set $\beta = 1$, as it can be eliminated through a redefinition of the scalar field ψ and the coupling constant α. Note this form of the action differs from that introduced in [103] by a factor of $\kappa = (16\pi)^{-1}$ such that $\tilde{\beta} = 2\,\kappa\beta$ and $\tilde{\alpha} = 2\,\kappa\alpha$.

By varying the action with respect to the metric and the scalar field we obtain two field equations. Variation with respect to the metric field yields

$$G_{\mu\nu} - \beta\,T_{\mu\nu} + \alpha\,K_{\mu\nu} = 0, \tag{3.34}$$

where the scalar field stress-energy tensor is

$$T_{\mu\nu} = \nabla_\mu\psi\nabla_\nu\psi - \frac{1}{2}g_{\mu\nu}\nabla^\gamma\psi\nabla_\gamma\psi, \tag{3.35}$$

and

$$K_{\mu\nu} = \left(g_{\rho\mu}g_{\delta\nu} + g_{\rho\nu}g_{\delta\mu}\right)\nabla_\sigma\left[\epsilon^{\gamma\delta\alpha\beta}\epsilon^{\rho\sigma\lambda\eta}R_{\lambda\eta\alpha\beta}\nabla_\gamma F(\psi)\right]. \tag{3.36}$$

Variation with respect to the scalar field yields

$$\beta\Box\psi + \alpha\frac{\partial F}{\partial\psi}\mathcal{G} = 0. \tag{3.37}$$

The scalar field is subject to the following boundary conditions: it must be asymptotically flat, and its first derivative must vanish on the horizon in isotropic coordinates,[2] namely

$$\frac{\partial\psi}{\partial\rho}|_{\rho\to\rho_{\rm H}} = 0, \qquad \psi|_{\rho\to\infty} = 0. \tag{3.38}$$

Utilizing the spherically symmetric metric ansatz in isotropic coordinates from before, the Einstein tensor is still given by Eqs. (3.23) and (3.24), and the two new sets of terms in the field equations are:

$$\begin{aligned} T_{tt} &= \frac{f}{2m}\left(\psi'\right)^2, \qquad T_{\rho\rho} = \frac{1}{2}\left(\psi'\right)^2, \\ T_{\theta\theta} &= -\frac{\rho^2}{2}\left(\psi'\right)^2, \qquad T_{\phi\phi} = \sin^2\theta\, T_{\theta\theta}, \end{aligned} \tag{3.39}$$

where the primes denote derivatives with respect to the ρ coordinate, e.g. $f' = \frac{df}{d\rho}$ and $K_{\mu\nu}$ is given below in Eq. (3.41).

Let us end this subsection with a discussion of the coupling function $F(\psi)$. In full EdGB gravity, the coupling function is $F(\psi) = \exp(\psi)$, but in the regime where ψ

[2] This follows from the regularity condition on the horizon [58, 87, 88].

is small, we can Taylor expand the coupling function as $F(\psi) = 1+\psi+\mathcal{O}(\psi^2)$. The ψ-independent term in this expansion is irrelevant as it leads to a theory that is identical to GR due to the Gauss-Bonnet invariant being a topological invariant. In this paper, we focus on numerical calculations for sGB gravity with both an exponential coupling and a linear coupling, namely for theories defined by

$$\begin{aligned} F(\psi) &= \psi \quad \leftrightarrow \text{ linear sGB}\,, \\ F(\psi) &= e^{\psi} \ \leftrightarrow \text{ EdGB}\,. \end{aligned} \tag{3.40}$$

We consider each of these cases separately in the next subsections.

$$\begin{aligned} K_{tt} &= F''\left[\frac{2f}{m^4}\left(m'\right)^2 + \frac{8f}{m^3\rho}\left(m'\right)\right] \\ &\quad + F'\left[\frac{4f}{m^4}\left(m''\right)\left(m'\right) - \frac{5f}{m^5}\left(m'\right)^3 + \frac{8f}{m^3\rho}\left(m''\right) - \frac{8f}{m^4\rho}\left(m'\right)^2 + \frac{8f}{m^3\rho^2}\left(m'\right)\right], \\ K_{\phi\phi} &= \sin^2\theta\, K_{\theta\theta}, \\ K_{\rho\rho} &= F'\left[-\frac{3}{f\,m^3}\left(f'\right)\left(m'\right)^2 - \frac{12}{f\,m^2\rho}\left(f'\right)\left(m'\right) - \frac{8}{f\,m\rho^2}\left(f'\right)\right], \\ K_{\theta\theta} &= F''\left[-\frac{2\rho^2}{f\,m^2}\left(f'\right)\left(m'\right) - \frac{4\rho}{f\,m}\left(f'\right)\right] \\ &\quad + F'\Bigg[-\frac{2\rho^2}{f\,m^2}\left(m''\right) + \frac{4\rho^2}{f\,m^3}\left(f'\right)\left(m'\right)^2 - \frac{2\rho^2}{f\,m^2}\left(f''\right)\left(m'\right) + \frac{\rho^2}{f^2m^2}\left(f'\right)^2\left(m'\right) \\ &\quad + \frac{2\rho}{f\,m^2}\left(f'\right)\left(m'\right) - \frac{4\rho}{f\,m}\left(f''\right) + \frac{2\rho}{f^2m}\left(f'\right)^2\Bigg]. \end{aligned} \tag{3.41}$$

Linear Scalar-Gauss-Bonnet Gravity

In the linear coupling theory, we can find an analytical perturbative solution to the field equations assuming the small-coupling limit, i.e. $\bar{\alpha} := \alpha/r_{\rm H}^2 \ll 1$ because $r_{\rm H}$ is of the order of the curvature length of the system under consideration and we introduce the dimensionless coupling constant $\bar{\alpha}$. Let us then use a deformed-

Schwarzschild ansatz for the metric tensor

$$ds^2 = -\left(f_0 + \epsilon f_1 + \epsilon^2 f_2\right) dt^2 + \left(m_0 + \epsilon m_1 + \epsilon^2 m_2\right) \left[d\rho^2 + \rho^2 d\Omega^2\right], \tag{3.42}$$

where $\epsilon \ll 1$ is a book-keeping parameter and $\bar{\alpha}$ is $\mathcal{O}(\epsilon)$, and the following ansatz for the scalar field

$$\psi = \psi_0 + \epsilon\psi_1 + \epsilon^2\psi_2. \tag{3.43}$$

Both of these ansatz are assumed valid up to $\mathcal{O}(\epsilon^3)$.

Inserting the ansatz in the field equations, we can analytically solve for the metric and the scalar field order by order in ϵ, imposing regularity on the horizon and asymptotic flatness at spatial infinity to fix any integration constants. At $\mathcal{O}(\epsilon^0)$, f_0 and m_0 are just the Schwarzschild metric in isotropic coordinates of Eq. (3.25), while the scalar field vanishes $\psi_0 = 0$ due to asymptotic flatness. At $\mathcal{O}(\epsilon)$, we find the metric perturbations vanish, while the scalar field perturbation is

$$\begin{aligned} f_1 &= 0, \qquad m_1 = 0, \\ \psi_1 &= \frac{4\bar{\alpha}}{\beta\rho\, r_{\rm H}^2} \frac{\left(1 + \frac{3r_{\rm H}}{2\rho} + \frac{23r_{\rm H}^2}{24\rho^2} + \frac{3r_{\rm H}^3}{32\rho^3} + \frac{r_{\rm H}^4}{256\rho^4}\right)}{\left(1 + r_{\rm H}/4\rho\right)^6}. \end{aligned} \tag{3.44}$$

At $\mathcal{O}(\epsilon^2)$, we find the first nontrivial correction to the metric tensor and we find that the scalar field perturbation at this order vanishes. Both are given below in isotropic coordinates in Eq. (3.45). We can then further express these analytic solutions in compactified coordinates for later use which are shown in Eq. (3.46). These results agree exactly with those found in [104] and [88] after performing the coordinate transformation from Schwarzschild to isotropic and compactified isotropic

coordinates.

$$
\begin{aligned}
f_2(\rho) &= \frac{\bar{\alpha}^2}{\beta\,(1+r_{\rm H}/4\rho)^{14}}\Bigg[-\frac{49r_{\rm H}}{5\rho}-\frac{49r_{\rm H}^2}{2\rho^2}-\frac{1637r_{\rm H}^3}{60\rho^3}-\frac{929r_{\rm H}^4}{96\rho^4}+\frac{16753r_{\rm H}^5}{3840\rho^5}+\frac{18893r_{\rm H}^6}{3840\rho^6}\\
&\quad-\frac{5573r_{\rm H}^7}{1920\rho^7}+\frac{146549r_{\rm H}^8}{430080\rho^8}+\frac{188761r_{\rm H}^9}{6881280\rho^9}-\frac{579r_{\rm H}^{10}}{917504\rho^{10}}-\frac{2231r_{\rm H}^{11}}{9175040\rho^{11}}\\
&\quad-\frac{6553r_{\rm H}^{12}}{48442112\rho^{12}}-\frac{6553r_{\rm H}^{13}}{19377684480\rho^{13}}\Bigg],\\
m_2(\rho) &= \frac{\bar{\alpha}^2}{\beta\,(1+r_{\rm H}/4\rho)^{8}}\Bigg[\frac{49r_{\rm H}}{5\rho}+\frac{499r_{\rm H}^2}{20\rho^2}+\frac{1345r_{\rm H}^3}{48\rho^3}+\frac{889r_{\rm H}^4}{64\rho^4}-\frac{11r_{\rm H}^5}{640\rho^5}-\frac{28787r_{\rm H}^6}{7680\rho^6}\\
&\quad+\frac{4689r_{\rm H}^7}{71680\rho^7}+\frac{4303r_{\rm H}^8}{57344\rho^8}+\frac{4727r_{\rm H}^9}{458752\rho^9}+\frac{20011r_{\rm H}^{10}}{27525120\rho^{10}}+\frac{35149r_{\rm H}^{11}}{1211105280\rho^{11}}\\
&\quad+\frac{2383r_{\rm H}^{12}}{484421120\rho^{12}}\Bigg],\\
\psi_2(\rho) &= 0,
\end{aligned}
\tag{3.45}
$$

$$
\begin{aligned}
f_2(x) &= \frac{\bar{\alpha}^2}{\beta}\frac{2\,x\,(-1+x^2)}{1155}(2383+154x+55594x^3-102410x^5+83094x^7\\
&\quad-32956x^9+5460x^{11}),\\
m_2(x) &= \frac{\bar{\alpha}^2}{\beta}\frac{64\,x\,(1-x)}{1155\,(1+x)^4}(-2383+25337x+25337x^2-37033x^3-37033x^4+,\\
&\quad+27031x^5+27031x^6-10094x^7-10094x^8+1610x^9+1610x^{10}),\\
\psi_1(x) &= \frac{\bar{\alpha}}{\beta}\frac{2\,(1-x^2)}{3}\left(11-7x^2+2x^4\right).
\end{aligned}
\tag{3.46}
$$

From these solutions we can obtain the ADM mass and scalar charge from an

expansion as $\rho \to \infty$, namely

$$\begin{aligned} M &= \frac{r_{\text{H}}}{2}\left(1 + \frac{49}{5}\frac{\bar{\alpha}^2}{\beta}\right) + \mathcal{O}(\alpha^3), \\ D &= \frac{4\bar{\alpha}}{\beta} + \mathcal{O}(\alpha^3), \end{aligned} \tag{3.47}$$

where $r_{\text{H}} = 2\,M_0$ and M_0 is the bare mass of the black hole that appears in the background (Schwarzschild) metric. Just as the ADM mass M is related to the coefficient of the $1/\rho$ term in an expansion of the metric about spatial infinity, the charge D is related to the same coefficient but in the expansion of the scalar field about spatial infinity.

With this analysis in hand, let us now focus on numerically solving the field equations, Eqs. (4.35) and (4.38), simultaneously for both metric functions g_{tt} and $g_{\rho\rho}$ and the scalar field ψ without any approximations. In order to do so, we employ the computational infrastructure described in detail in Sec. 4. In particular, we choose an initial grid of $N = 101$ points and a Newton polynomial order $r = 12$. For the actual computation, we set $r_{\text{H}} = 1$ which sets the bare mass of the black hole to $M_0 = 1/2$. Different black hole masses can be obtained by scaling the radial coordinate appropriately. Note this renders our equations dimensionless and the correct units can be restored through a similar rescaling. The desired tolerance of the solution is tol $= 10^{-5}$ which is both placed on the residual and on the relative tolerance of the discretization correction in Eq. (B.41). The tolerance in the iterative linear solvers described in Sec. B is $\text{LS}_{\text{tol}} = 10^{-12}$ and places a lower bound on our numerical accuracy. We will also employ the compactified coordinate system defined in Eq. (3.29) to change our domain of integration to the finite domain $x \in [0, 1]$. In these compactified isotropic coordinates, the perturbative corrections of Eq.(3.45) are shown below in Eq. (3.46). These corrections are used as our initial guess and

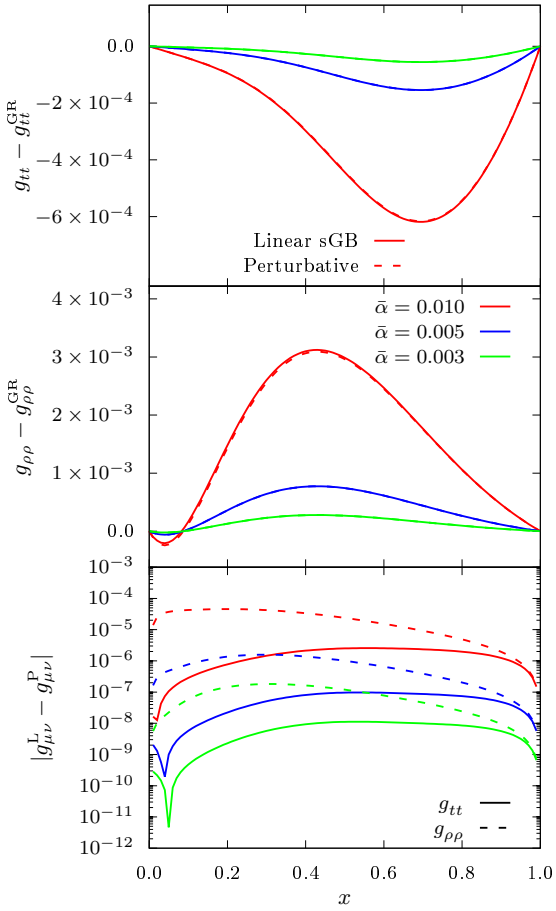

Figure 3.5: Linear scalar-Gauss-Bonnet correction to g_{tt} (top) and $g_{\rho\rho}$ (middle), and difference (bottom) between the numerical and the analytic perturbative solutions as a function of the compactified coordinate x and for different $\bar{\alpha}$ indicated by color. In the top two panels, the solid lines indicate the g_{tt} or $g_{\rho\rho}$ component numerical solution and the dashed lines indicate the analytic perturbative solution. Conversely, in the bottom panel, the solid lines indicate the g_{tt} and dashed lines indicate the $g_{\rho\rho}$ component difference with the same color scheme in the top two panels. The analytic perturbative solution agrees very well with the full numerical solution, with differences that grow only to $\mathcal{O}(10^{-5})$.

convergence typically occurs within 1 to 3 iterations. Note that for $\bar{\alpha} < 5 \times 10^{-4}$, we find that the perturbative initial guess itself satisfies the field equations to below our specified tolerance. This suggests that below this minimum coupling value, our numerical solution is indistinguishable from the perturbative solution.

We can now compare the analytic perturbative solutions to the full non-linear solutions. The top and middle panels of Fig. 3.5 show the sGB corrections to the metric components as a function of the compactified coordinate for different choices of the coupling constant $\bar{\alpha}$. Observe that the numerical solution is almost indistinguishable from the analytic perturbative solution everywhere in the domain. The agreement is so remarkable that it is worthwhile exploring the difference between the analytic and the numerical solution, which we do in the bottom panel of Fig. 3.5. Observe that the difference is indeed very small, ranging from $\mathcal{O}(10^{-10})$ to almost $\mathcal{O}(10^{-4})$ depending on the metric component one studies, and it increases as the coupling strength is increased as expected. We have verified that the residual is always orders of magnitude smaller than this difference in our numerical solutions.

We observe similar behavior in the scalar field. The top panel of Fig. 3.6 shows the scalar field solved numerically and the analytic perturbative solution both as a function of the compactified x coordinate. Observe again that the curves are right on top of each other. The difference between these curves is shown in the bottom panel of this figure, where we see clearly that the difference ranges from $\mathcal{O}(10^{-10})$ to $\mathcal{O}(10^{-4})$ for the largest couplings we considered. As before, we have verified that the residual of the scalar field equation of motion is smaller than this difference for all cases considered. Observe, however, that this time the difference between the numerical solution and the analytic perturbative solution is much larger than it was for either metric component. This makes sense because the modified field equations depend on the scalar field through its stress-energy tensor, which is quadratic in the

scalar field. Thus, we expect a difference of $\mathcal{O}(10^{-a})$ for some $a \in \mathbb{R}_{>0}$ to contribute a difference of $\mathcal{O}(10^{-2a})$ to the metric components.

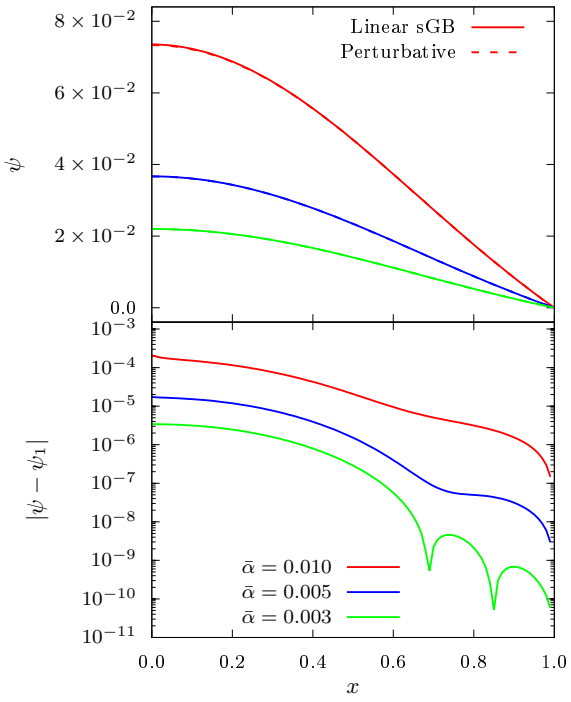

Figure 3.6: Scalar field ψ (top) and difference between the numerical and the analytic perturbative solution (bottom) as a function of the compactified coordinate x in linear sGB. Solid lines indicate the numerical solution with linear coupling and dashed lines indicate the analytic perturbative solution, color coded for different coupling strengths $\bar{\alpha}$.

From these comparisons we can extract a few useful conclusions. Perhaps most importantly, we see that the non-linear corrections to the solution are truly small everywhere in the domain. This is sensible because the scalar field itself is small and the values of $\bar{\alpha}$ that we explore are small, so the corrections to GR can be treated perturbatively. Another interesting observation is that the largest deviations from GR manifest somewhere in the middle of the domain. This is in part due to the boundary conditions: at spatial infinity the metric must be asymptotically flat so

the GR deformation must vanish at a suitable fall-off rate; near the horizon, the GR deformation must be regular, but due to its asymptotic form near the horizon, it must also vanish there. Our choice of quantities to compare also plays an important role. Note that we compare metric coefficients at different physical locations, as $x = 0$ at the horizon by definition and the horizon can be at a different location in the two metrics we are comparing. It is also worth pointing out that observables may depend on derivatives of the metric or even integrals of combinations of metric functions in the spatial domain and, hence, agreement between metric coefficients in part of the domain does not necessarily imply that observables in linear sGB will be close to those in GR. We have seen this already in Fig. 3.1, and will return to this point in Sec. 4.

Einstein-dilaton-Gauss-Bonnet Gravity

Let us now consider the case of an exponential coupling function. The resulting field equations are Eqs. (4.35) and (4.38) with $F(\psi) = e^{\psi}$. In this case, a perturbative solution in small coupling $\bar{\alpha}$ does not exist, but we can still compare any numerical solutions to the small coupling approximation for the linear theory of the previous subsection. We find a numerical solution using the computational infrastructure of Sec. 4, with the same choices for the grid spacing, Newton polynomial order, etc as in the previous subsection. Note that we also use the perturbative initial guess from the previous subsection and we find that the minimum coupling for numerical distinguishability is $\bar{\alpha} < 8 \times 10^{-5}$. This suggests that for problems in modified gravity where we do not have analytic solutions, there should be a regime in parameter space where deviations away from GR (or in this case a closely related theory) are small enough that the GR solution itself can act as a sufficient initial guess for convergence. If this is the case, then we can use these small coupling solutions as initial guesses for

higher coupling solutions and successively build solutions in this manner.

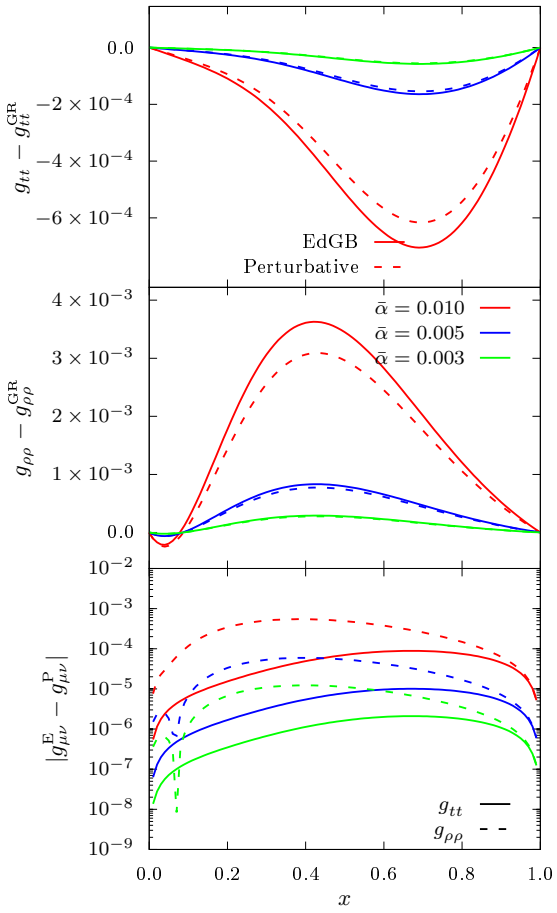

Figure 3.7: Same as Fig. 3.5 but for Einstein-dilaton-Gauss-Bonnet. In contrast to the differences between the linear and perturbative solution in Fig. 3.5, the differences between the numerical solution in the exponential coupling case and perturbative analytic solution in the linear coupling case are much more prominent, growing to $\mathcal{O}(10^{-5})$ for the highest couplings explored.

The top and middle panels of Fig. 3.7 show the EdGB corrections to the metric components as a function of the compactified coordinate x for different choices of the coupling constant $\bar{\alpha}$. In contrast to the linear sGB results of Fig. 3.5, in EdGB the corrections to the metric are immediately noticeable. When comparing the difference between the analytic and numerical solutions in the bottom panel of Fig. 3.5, we see

they range from 10^{-5} to 10^{-3}, whereas the difference in the linear coupling case ranged from 10^{-10} to 10^{-4}. The results of this comparison are not very surprising because the analytic perturbative solution was found exclusively in the linear coupling case.

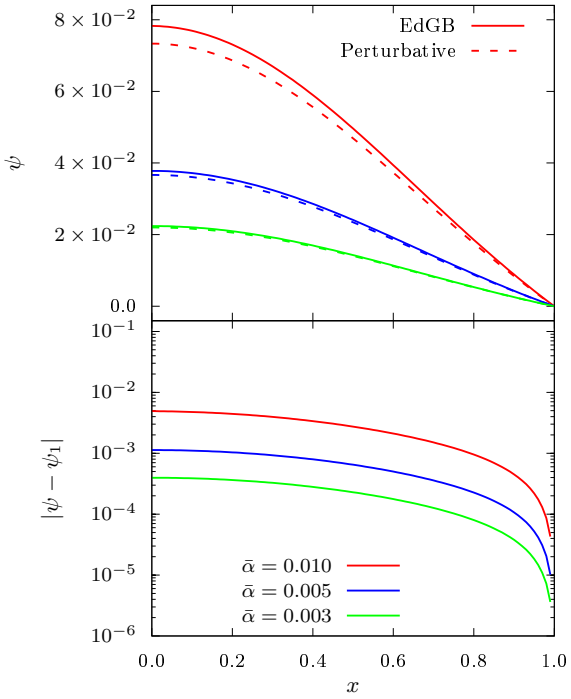

Figure 3.8: Same as Fig. 3.6 but for EdGB. Observe that this time the numerical solution of the exponential coupling theory differs significantly from the analytic perturbative solution of the linear coupling theory.

These same features can also be seen in the scalar field solution, as shown on the left panel of Fig. 3.8. The differences, shown on the right panel of this figure, range from $\mathcal{O}(10^{-5})$ to $\mathcal{O}(10^{-2})$, while for comparison the differences in the linear coupling case ranged from 10^{-10} to 10^{-4}.

From these comparisons we can also extract a few useful conclusions. Unlike in the linear sGB case, we see here that the analytic perturbative solution found in that case does not agree with the fully nonlinear solution. This is expected. Perturbing in the coupling constant and perturbing in the scalar will formally yield the same field

equations. This can be understood by the fact that one can always absorb the coupling constant in a scalar field redefinition. The range of validity of the two expansions, and hence their physical interpretation, can be different. Nonetheless, this argument clearly implies that the perturbative solution will provide a better approximation to the linear coupling than the exponential one. Finally, as in the linear sGB case, we find that the metric corrections vanish near the horizon and compactified infinity, and both deviations asymptote to each other near infinity, but derivatives of the metric potentials can be large.

Properties of Solution

In this section we explore the physical properties of the numerical solutions found in the previous section. We begin by finding analytical models that we fit to the data to provide accurate, closed-form expressions that allow for the rapid computation of physical observables. We then use these fitted models and the numerical results to calculate the location of the innermost stable circular orbit and the light ring, and compare them with each other and with the analytical perturbative solutions.

Fitting Function

In the compactified coordinate system introduced in Eq. (3.29), the full nonlinear solutions can be expressed as

$$\begin{aligned} f(x) &= f_{\rm GR} + f_2(x) + f_{\rm nonlin}(x), \\ m(x) &= m_{\rm GR} + m_2(x) + m_{\rm nonlin}(x), \\ \psi(x) &= \psi_1(x) + \psi_{\rm nonlin}(x), \end{aligned} \tag{3.48}$$

where $f_2(x)$, $m_2(x)$, and $\psi_1(x)$ are the analytical perturbed solutions of Eqs. (3.46) in the compactified coordinates and $f_{\rm nonlin}(x)$, $m_{\rm nonlin}(x)$, $\psi_{\rm nonlin}(x)$ are nonlinear

corrections that we wish to find.

Using the analytical perturbed solutions as an ansatz, we propose best fit models for the non-linear corrections of the form

$$
\begin{aligned}
f_{\rm nonlin}(x) &= x\left(-1+x^2\right)\left(\sum_i\sum_j a_{i,j}\bar{\alpha}^i x^j\right),\\
m_{\rm nonlin}(x) &= \frac{x\left(1-x\right)}{\left(1+x\right)^4}\left(\sum_i\sum_j b_{i,j}\bar{\alpha}^i x^j\right),\\
\psi_{\rm nonlin}(x) &= \left(1-x^2\right)\left(\sum_i\sum_j c_{i,j}\bar{\alpha}^i x^j\right),
\end{aligned}
\tag{3.49}
$$

where we have set $\beta = 1$. We then fit these models to our numerical solutions to determine the constants $(a_{i,j}, b_{i,j}, c_{i,j})$ on the grid domain $x \in [0,1]$ and $\bar{\alpha} \in [1\times 10^{-4}, 0.013]$. For $\bar{\alpha} < 1\times 10^{-4}$ the analytical perturbative solution is indistinguishable from the full nonlinear solution to our specified tolerance. For $\bar{\alpha} > 0.013$ we find pathologies in the numerical solution that we will describe in Sec. 3. The fitting order of our models is determined by systematically increasing the polynomial order of each function until the residual between the numerical solution and the model saturates. Some of the best-fit coefficients $(a_{i,j}, b_{k,l}, c_{m,n})$ are included in Appendix C Table D.1, C.2, and C.3 respectively, but they are available in a `Mathematica` file upon request.

A comparison between the numerical data and the analytical fitted models is presented in Fig. 3.9. Here we plot the field components (properly rescaled to fit all in the same figure) in each top plot and their corresponding residuals as a function of the compactified coordinate x in each bottom plot for both the linear sGB and EdGB solutions and for two coupling values of $\bar{\alpha}$. We find that the residual between the numerical data and the analytical fitted model is always below our desired tolerance on the numerical solution of $\mathcal{O}(10^{-5})$. With this caveat, the fitted models can be

treated as "exact" for practical applications (up to the accuracy mentioned above).

ISCO

The inner edge of accretion disks around black holes are typically characterized by the innermost stable circular orbit (ISCO) of massive test-particles [8]. For our spherically symmetric ansatz, the marginal stable circular orbits are determined by solving for circular timelike geodesics for massive test-particles [21, 77] orbiting the black hole. This is equivalent to requiring conditions on the effective potential, $\dot{r}^2 = V_{\text{eff}}$, where this potential is given by

$$V_{\text{eff}} = \frac{1}{m(\rho)}\left(-1 - \frac{L^2}{m(\rho)\rho^2} + \frac{E^2}{f(\rho)}\right), \tag{3.50}$$

where E and L are the energy and angular momentum per unit mass (for massive particles) respectively, defined from the conserved quantities corresponding to the temporal and azimuthal Killing vectors in a stationary and spherically symmetric spacetime.

As in Newtonian gravity, a stable or an unstable circular orbit occurs at local minima or maxima of the effective potential, such that $\dot{r} = V_{\text{eff}} = 0$ and $V'_{\text{eff}} = 0$. In the Schwarzschild metric, there is both an unstable and a stable circular orbit, such that the unstable orbit is closer to the horizon, and the distance between these orbits is determined by the angular momentum L. The innermost stable circular orbit is equivalent to finding the value of the angular momentum where these stable and unstable orbits coincide (because the unstable orbit will always be closer to the horizon than the stable orbit). By analogy, requiring these orbits coincide is equivalent to finding the saddle points of the effective potential, which are located at $V''_{\text{eff}} = 0$.

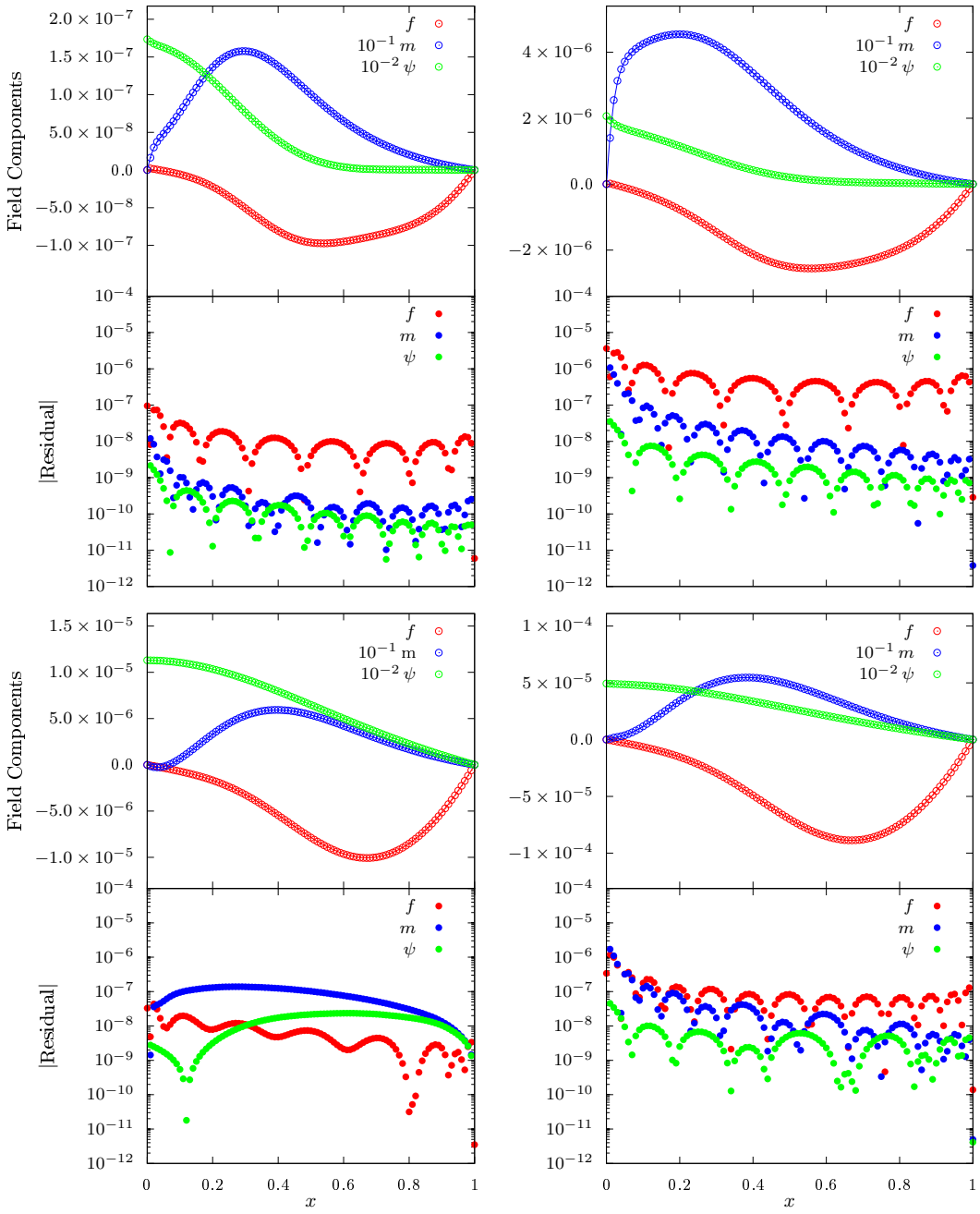

Figure 3.9: Comparison of the fitted models to the linear coupling solution (top) and the exponential coupling solutions (bottom) for $\alpha = 0.005$ (left) and $\alpha = 0.010$ (right). Included are the rescaled numerical solution and fits (top) and the resulting fit residual (bottom). Color indicates the field component and the solid line indicates the analytical fitted model, whereas dots indicate numerical data points. The field components have been properly rescaled, as indicated in the legend. Note that for both coupling strengths the model fit residual is below our desired tolerance throughout the entire x domain.

By combining these three conditions, we find the generalized equation

$$\left(\frac{1}{f(\rho)}\right)'\left(\frac{1}{\rho^2 m(\rho)}\right)'' - \left(\frac{1}{\rho^2 m(\rho)}\right)'\left(\frac{1}{f(\rho)}\right)'' = 0, \tag{3.51}$$

the solutions (there may be multiple) of which give the locations of the marginal stable circular orbits of the spacetime. The smallest of these solutions is identified as the ISCO.

In our compactified isotropic coordinates, the location of the ISCO in GR is $x^{\rm GR}_{\rm ISCO} = \sqrt{6}/3$ which corresponds to the familiar $r^{\rm GR}_{\rm ISCO} = 3\,r_{\rm H} = 6\,M_0$ when transformed to Schwarzschild coordinates. In sGB gravity, the ISCO location is shifted from this Schwarzschild value. We can find the ISCO shift using the perturbative solution of Eq. (3.46) to find

$$x_{\rm ISCO} = x^{\rm GR}_{\rm ISCO}\left[1 + \frac{\bar{\alpha}^2}{\beta}\left(\frac{427634}{841995} + \frac{2383}{13860}\sqrt{6}\right)\right], \tag{3.52}$$

which is identical to that of [104] when converted to Schwarzschild coordinates. We can also find the ISCO shift for the numerical metric solving Eq. (3.51) with a Newton-Raphson algorithm. By taking the location of the ISCO in GR as our initial guess, we ensure that the converged root is the desired root, as we expect deviations to be comparably small.

We presented these results already on the left panel of Fig. 3.2 in Sec. 4, where we saw that the ISCO shift is typically smaller than 10^{-4}. We also saw there that the shift computed with the analytic perturbative solution in the linear sGB case [Eq. (3.52)] agrees well the shift computed with the numerical solution in linear sGB but disagrees in EdGB. Interestingly, the shift computed with the fitted models agree extremely well with the numerical solution in both cases.

Light Ring

The light ring or photon sphere is the surface generated by all unstable circular null geodesics of photons. The location of the light ring around black holes is important for observations with the Event Horizon Telescope [44], which is imaging the black hole shadow of Sagittarius A*, i.e. the electromagnetically dark region caused by photons that cross the light ring and fall into the event horizon. Future observations of black hole shadows may be able to place constraints on the location of the light ring in other quadratic gravity theories [16].

Similar to the ISCO calculation, the light ring can be found by requiring certain conditions on the effective potential. For massless particles, there is only a single unstable circular orbit and there are no stable circular orbits. Thus to find the unstable circular orbit, we need only require $V_{\text{eff}} = 0$ and $V'_{\text{eff}} = 0$, which leads to the equation

$$f(\rho)\left(\frac{1}{f(\rho)}\right)' - \rho^2 m(\rho)\left(\frac{1}{\rho^2 m(\rho)}\right)' = 0. \tag{3.53}$$

As before, the smallest solution to this equation returns the location of the light ring around the black hole.

The location of the light ring in GR is simply $x_{\text{LR}}^{\text{GR}} = \sqrt{3}/3$, which reduces to $r_{\text{LR}} = 1.5\, r_{\text{H}} = 3\, M_0$ in Schwarzschild coordinates. As in the ISCO case, the location of the light ring is shifted in sGB gravity. We can calculate this shift with the perturbative analytic solution to find

$$x_{\text{LR}} = x_{\text{LR}}^{\text{GR}}\left[1 + \frac{\bar{\alpha}^2}{\beta}\left(-\frac{189328}{841995} + \frac{2383}{3465}\sqrt{3}\right)\right], \tag{3.54}$$

a result that to the best of our knowledge had not appeared in the literature previously. In the full non-linear case, we must solve Eq. (3.53) numerically using a Newton-Raphson method with the GR shift as our initial guess.

The light-ring shift was already presented on the right panel of Fig. 3.2. The shift is comparable to the shift of the ISCO, typically smaller than 10^{-4}. Interestingly, we do find a noticeable disagreement between the analytic perturbative solution and the linear coupling case for higher values of $\bar{\alpha}$, which was not present in the other calculated observables. The comparison between these two solutions in Fig. 3.5 shows that the largest differences between them occur closer to the horizon. Therefore this difference is larger in the region around the location of the light ring ($x_{\rm LR}^{\rm GR} \approx 0.57$) than in both the region around the location of the ISCO ($x_{\rm ISCO}^{\rm GR} \approx 0.82$) and asymptotically far away ($x \approx 1$). Thus it is expected that an observable calculated in this region should have a comparatively magnified discrepancy between the analytic perturbative solution and the numerical linear sGB solution. We also find that the fitted models agree extremely well with the numerical solutions for both coupling cases.

Naked Singularity

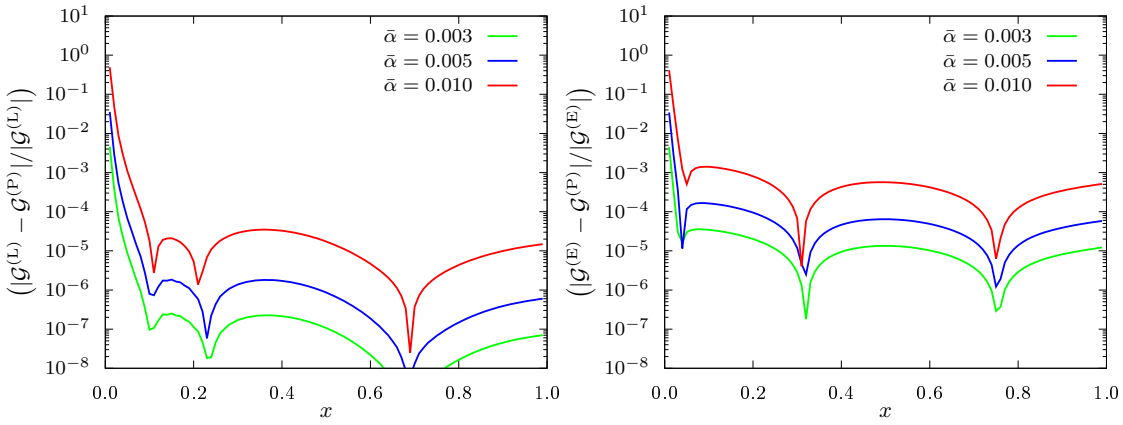

(a) Linear GB invariant difference (b) Exponential GB invariant difference

Figure 3.10: Logarithm of normalized difference between the Gauss-Bonnet curvature invariant computed with the analytical perturbative (superscript "P") solution and the numerical solution in the linear coupling theory (left panel) and the exponential coupling theory (right panel).

Spherically symmetric black holes in sGB gravity have been shown to possess a minimum size for a given $\bar{\alpha}$ in both EdGB [58] and linear sGB [88]. This results from a consistency condition on the field equations, obtained by requiring the scalar field to be regular on the horizon. Physically, as one increases the coupling strength $\bar{\alpha}$, the location of the curvature singularity inside the horizon grows while the location of the event horizon shrinks, until at some critical value of $\bar{\alpha}$ the two coincide. For values of $\bar{\alpha}$ larger than this critical value, the curvature singularity is outside the event horizon, leading to a naked singularity. Requiring that the latter do not exist yields a maximum value of the coupling strength (and a minimum size of the event horizon) for which sGB black hole solutions can exist.

Our numerical solutions confirm these results. In our numerical calculations, we impose boundary conditions on the horizon using compactified coordinates at $x = 0$. The transformation from Schwarzschild to compactified coordinates absorbs the horizon shift, so that physically the horizon is always located at $x = 0$ in our numerical grid. This then implies that there is a maximum value of $\bar{\alpha}$ above which black hole solutions should not exist in our numerical code. Indeed, we find that for values of $\bar{\alpha}$ larger than roughly $\bar{\alpha}^{\star} \approx 0.0131$ on our grid of $N = 101$ points, our code ceases to converge to the required tolerance. This is because a curvature singularity sufficiently near (or inside) the computational domain induces large errors in the Newton polynomial representation of the solution near the horizon boundary, which then propagates through the entire domain in each iteration, preventing the algorithm from converging.

This is indeed what we see in our numerical calculations as we increase $\bar{\alpha}$: the estimated discretization error on the horizon ($x = 0$) begins to grow as the location of the curvature singularity approaches the event horizon boundary. Eventually, the curvature singularity is close enough to the horizon radius that the discretization

error near the horizon becomes too large for the specified tolerance. In order to ensure that these results are not a numerical artifact, we implemented adaptive step size refinement on the computational grid that is triggered if the discretization error becomes too large. Even with this adaptive measure in place, the discretization error still grows near the horizon for sufficiently large $\bar{\alpha}$, preventing the code from converging.

In order to further support these conclusions, we have computed the Gauss-Bonnet curvature invariant for different values of $\bar{\alpha}$ in both the linear sGB and EdGB theories. Figure 3.10 shows this invariant as a function of the compactified coordinate x. Observe that as $x \to 0$ (near the horizon) the curvature invariant begins to grow to ever larger values as $\bar{\alpha}$ is increased. Observe that as $\bar{\alpha}$ increases, the correction to $\mathcal{G}$ at orders larger than $\mathcal{O}(\alpha^2)$ begin to quickly approach the correction at $\mathcal{O}(\alpha^2)$ where this effect is not present.

Conclusions

We have here developed a new numerical framework to solve for stationary and spherically-symmetric spacetimes that represent black holes in a wide class of modified theories of gravity. This framework uses a Newton polynomial representation for the discretized functions, it then recasts the differential system as a linear algebra problem, and then solves the latter through a relaxed Newton-Raphson iterative method. Through the successive minimization of the residual, our framework is capable of controlling the maximum error in the final numerical solution. We have validated this framework through a toy problem consisting of a simple differential equation, through the Schwarzschild metric and by investigating black holes in sGB gravity.

With the sGB solutions at hand, we then investigated a series of physical

properties of these spacetimes. First, we verified that the differences between exact numerical solutions and analytic perturbative solutions are very small when the coupling is linear. We then also verified that the exact numerical solutions in linear sGB differ quite significantly from those in EdGB. These similarities and differences manifest themselves not only through the metric tensor, but also through physical observables like the ADM mass, the scalar charge, the location of the ISCO, and that of the light-ring. We finally verified that sGB black holes do not exist beyond a critical value of the sGB coupling, as beyond this value a naked curvature singularity arises.

We then concluded our analysis by developing analytic fitting functions for the numerical solutions. These fitting functions are constructed through a combination of controlling factors (inspired by the analytic perturbative solution) and polynomials in the compactified coordinate. We verified that the fitting functions agree with the numerical solutions up to the numerical error in the latter. We then computed physical observables, like the ADM mass, the location of the ISCO and that of the light ring with the fitting functions and found excellent agreement between these results and those obtained from the exact numerical solutions.

The work we did here now opens the door to several further studies. The fitting functions described above, for example, could be used as the analytical background on which to study polar and axial perturbations. Such perturbations would then reveal the quasi-normal mode spectrum of sGB black holes for arbitrary values of the coupling. The quasi-normal mode frequencies could then be used to carry out spectroscopic tests of GR with gravitational wave observations of merging black holes (provided the merger remnant has very small final spin).

Another interesting direction for future research is the extension of the methods developed here to axisymmetric black holes. The computational infrastructure we

presented here is easily extendable to this case. The system of equations of course becomes more complicated not only because new metric functions must be solved for, but also because these functions will depend on both radius and polar angle. We have already extended the work presented in this paper to a two-dimensional grid that is capable of solving for the Kerr metric in GR, and thus, we expect that extensions to modified gravity at this point should be straightforward.

Once such solutions are found, the fitting methodology developed here could be implemented in the axisymmetric case to find fully analytic approximations for all components of the metric tensor. Such a solution could then be used once more as a background on which to study the evolution of perturbations. The quasi-normal spectrum of these perturbations could then be used to place constraints on a variety of modified gravity theories through the future observations of gravitational wave ringdown modes with advanced detectors.

Acknowledgments

We would like to acknowledge Hector Okada da Silva for useful comments and suggestions. A. S. and N. Y. would like to acknowledge support from the NSF CAREER grants PHY-1250636 and PHY-1759615, as well as NASA grants NNX16AB98G and 80NSSC17M0041. T. P. S. acknowledges partial support from the STFC Consolidated Grant No. ST/P000703/1 and networking support from the COST Action GWverse CA16104.

NUMERICAL BLACK HOLE SOLUTIONS IN MODIFIED GRAVITY THEORIES: AXIAL SYMMETRY CASE

Contribution of Authors and Co-Authors

Manuscript in Chapter 4

Author: Andrew Sullivan

Contributions: Performed mathematical analysis of problem, compared results, and wrote the manuscript.

Co-Author: Nicolás Yunes

Contributions: Thought of the problem, helped find errors in the code, helped interpret results, discussed implications, and edited manuscripts.

Co-Author: Thomas Sotiriou

Contributions: Thought of the problem, helped find errors in the code, helped interpret results, discussed implications, and edited manuscripts.

Manuscript Information Page

Andrew Sullivan, Nicolás Yunes, and Thomas Sotiriou

Physical Review D

Status of Manuscript:

__X__Prepared for submission to a peer-reviewed journal

_____Officially submitted to a peer-reviewed journal

_____Accepted by a peer-reviewed journal

_____Published in a peer-reviewed journal

Published by:

Abstract

We extend recently developed numerical code to obtain stationary, axisymmetric solutions that describe rotating black hole spacetimes in a wide class of modified theories of gravity. The code utilizes a relaxed Newton-Raphson method to solve the full nonlinear modified Einstein's Equations on a two-dimensional grid with a Newton polynomial finite difference scheme. We validate this code by considering static and axisymmetric black holes in General Relativity. We obtain rotating black hole solutions in scalar-Gauss-Bonnet gravity with a linear (linear scalar-Gauss-Bonnet) and an exponential (Einstein-dilaton-Gauss-Bonnet) coupling and compare them to analytical and numerical perturbative solutions. From these numerical solutions, we construct a fitted analytical model and study observable properties calculated from this model and the numerical results.

Introduction

As we enter a new era of multi-messenger astrophsics, many new experiments will allow us to test Einstein's theory of general relativity (GR) in the strong field regime [38, 48, 75, 97, 103]. As we begin to probe this regime, previously used perturbative techniques may eliminate strong field instabilities that may have observable consequences, such as spontaneous scalarization of black holes that arise in a class of scalar-tensor theories within a certain mass range [45, 86]. We here extend previous steps taken towards producing theory agnostic predictions of black holes in modified theories of gravity without the use of perturbation theory.

We recently developed a numerical infrastructure to solve the modified Einstein equations for static and spherically symmetric black hole spacetimes [90]. The infrastructure used symbolic manipulation software to calculate the modified Einstein's

equations and export them into an executable C programming function. This was then discretized using a finite element method by replacing each differential operator at each grid point with a Newton interpolation polynomial and calculating the residual of the field equations. By minimizing this residual using a relaxed Newton-Raphson method, we can iteratively converge to the desired solution by calculating the linearized correction to our functions by solving a linear system of equations evaluated from the Jacobian matrix of our discretized differential equations. To validate this code, we applied this infrastructure to static and spherically symmetric black hole spacetimes in GR and scalar Gauss-Bonnet gravity with a linear (linear sGB) and exponential (Einstein-dilaton-Gauss-Bonnet, EdGB) coupling function. We now wish to extend this analysis to rotating black hole spacetimes using the same numerical infrastructure.

In this paper, we wish to describe the numerical setup to solve black holes in axially symmetric spacetimes. The extension is relatively straightforward where we instead discretize our partial differential equations on a two dimensional grid and simply replace each differential operator in the new dimension with the same Newton interpolation polynomial method as in the one dimensional case. To discretize any mixed partial derivatives, we follow the approach of [83] and introduce an auxiliary variable with a corresponding differential equation whose residual must simultaneously be minimized with the remaining system of differential equations.

Although the methodology of adding a second dimension is straightforward, unfortunately the computational complexity increases considerably. Take for example that our discretized linear system of equations in spherical symmetry had n grid points and $M = 3$ fields (two metric fields and the scalar field) to solve for. This led to a square Jacobian matrix of $(M \times n)^2 = 9n^2$ elements. We now must discretize our grid into a total of $n \times m$ grid points with four metric fields in axial symmetry

and the scalar field for a total of five fields to solve for. Furthermore, each mixed partial derivative of the fields require an additional differential equation so our total number of fields to minimize is doubled to $M = 10$ and our square Jacobian matrix grows to $(M \times n \times m)^2$ elements. As a result it is no longer feasible to evaluate our numerical infrastructure on laptop class computers and we must turn to high performance computing clusters but fortunately there is a wealth of publicly available resources on the subject matter.

We begin by validating our infrastructure by studying rotating black holes in GR and we directly compare the numerical result to the known Kerr solution. We find that our code converges to the correct solution within three iterations with our chosen initial guess. After validation in GR, we construct stationary, axially symmetric black holes in scalar Gauss-Bonnet (sGB) gravity, a well motivated modified theory that is a member of the quadratic gravity class [20, 24, 103].

When studying black holes in scalar Gauss-Bonnet gravity, we will again consider the two typical forms of the coupling function between the massless scalar field and the Gauss-Bonnet invariant. When the scalar field is coupled through an exponential to the Gauss-Bonnet invariant this is commonly referred to as Einstein-dilaton-Gauss-Bonnet (EdGB) gravity. In the regime where the scalar field is small, one can approximate the exponential as a linear coupling to the Gauss-Bonnet invariant which is commonly referred to as the linear scalar-Gauss-Bonnet gravity. We will again adopt this terminology throughout this paper namely: 'linear sGB' will refer to the use of a linear coupling function and 'EdGB' will refer to the exponential coupling function.

Stationary black holes have been found in linear sGB in axisymmetry using a slow-rotation approximation [15, 30, 66, 69, 72]. Conversely axisymmetric black holes in EdGB have only been obtained numerically [60]. There has also been recent work

on the dynamical evolution of black holes and binaries in sGB gravity [22, 23, 78, 98].

Unfortunately, the analytic solutions in slow rotation were derived in different coordinate systems which makes a direct comparison of our solutions impossible without resolving the perturbed system of equations order by order in compactified isotropic coordinates. To resolve this, we instead numerically solve the equations using a weak-coupling expansion where $\alpha \ll 1$ using our numerical infrastructure and verify that the solution in the spherically symmetric limit is equal to the known spherically symmetric analytic perturbed solution. We can then compare the fully nonlinear solutions in linear sGB and EdGB to this axially symmetric perturbative solution.

In the linear case, not including rotation, we recover the previous observation that the perturbative solution that assumes weak-coupling agrees exceptionally well with the exact linear solution while there are still large differences in the exponential coupling solution. If we include rotation, we find that the magnitude of these differences in the exponential coupling solution is suppressed as we increase the rotation of the black hole. In Fig. 4.1 we present the relative fractional correction in the ADM mass (left) and the scalar monopole charge (right) as a function of the dimensionless sGB coupling parameter $\bar{\alpha} = \alpha/r_{\rm H}^2$. Here we compare the weak-coupling perturbative solution, the linear sGB solution, and the EdGB solution for 3 different dimensionless spins that correspond to the black hole angular velocity on the horizon for the corresponding dimensionless spin value in GR. From these we can see that for the same coupling constant α, by increasing the spin of the black hole, we *decrease* its scalar charge and *suppress* the deviation in the mass from its GR value. Conversely, angular momentum *increases* for larger spin as expected, shown in Fig. 4.2 where we present the fractional change in the ADM angular momentum of the black hole for each solution for the same three dimensionless spin values. Note that

the dimensionless spins that we report here are not equivalent to the true spins of each black hole. As we shall see, our input parameter for the spin is the angular velocity of the black hole on the horizon $\Omega_{\rm H}$ which are set by the corresponding angular velocity of a Kerr black hole with the reported spin.

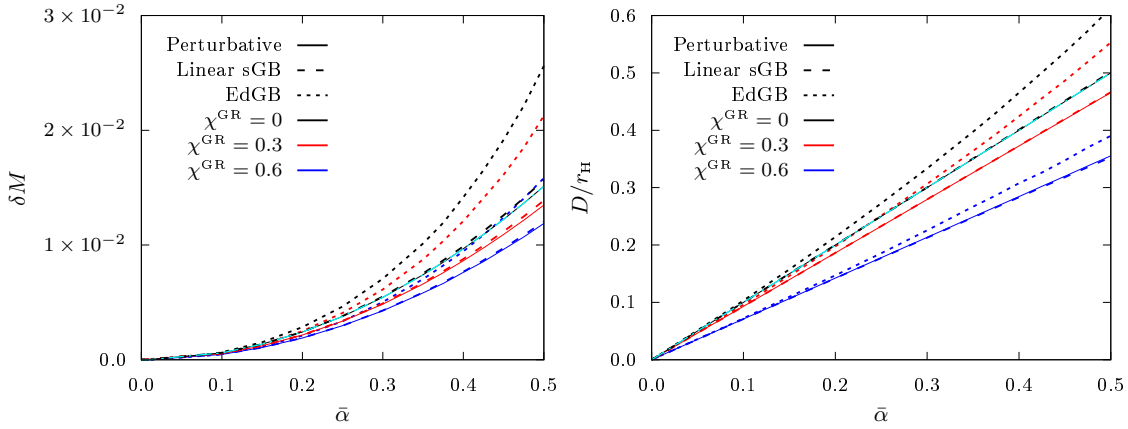

(a) Mass correction

(b) Scalar charge

Figure 4.1: Fractional change in mass (left) and the dimensionless scalar charge (right) vs dimensionless coupling $\bar{\alpha}$ for three dimensionless GR spin values, $\chi = 0, 0.3,$ and 0.6 denoted by the black, red, and blue colors respectively. The perturbative solution is denoted by the solid line, the sGB solution by the dashed line, and the EdGB solution denoted by the dotted line. We have also included the analytic perturbative solution in spherical symmetry as the dashed cyan colored line. Here we recover the agreement between the perturbative solution and the linear sGB solution in the nonrotating limit and the discrepancy of the EdGB solution. As we increase the spin of the black hole, we find a decrease in the scalar charge and a corresponding suppression of the fractional change in the mass from GR.

With these exact solutions in hand, we can calculate the location of the innermost stable circular orbit (ISCO) and the light ring. Figure 4.3 shows the fractional change in the location of the ISCO (left) and the light ring (right). We again find good agreement with the numerical perturbative solution and the linear sGB solution. For larger values of $\bar{\alpha}$, we find a large disagreement for the EdGB solutions. Finally, using the solutions, we can construct analytically fitted models for selected coupling

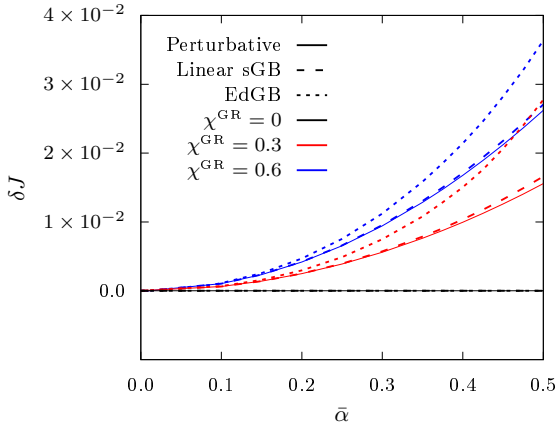

Figure 4.2: Fractional change in angular momentum vs dimensionless coupling $\bar{\alpha}$ for three dimensionless GR spin values, $\chi = 0, 0.3$, and 0.6 denoted by the black, red, and blue colors respectively. The perturbative solution is denoted by the solid line, the sGB solution by the dashed line, and the EdGB solution denoted by the dotted line. Here we find an increase in the angular momentum from GR both with increasing coupling and spin.

and spin values to allow for the rapid computation of these physical observables. We have verified that the observables from the models agree with the numerical solutions to within the prescribed error tolerance of the solutions. The fitting coefficients are available online though we provide a few examples in Appendix D.

The importance of the infrastructure presented here is that we are allowed to make minimal assumptions about the specific modified theory of gravity we are considering due to the symbolic nature in which we can calculate and export the field equations. The boundary conditions on the horizon and infinity only require that an event horizon exist and that the spacetime is asymptotically flat. Any additional fields only need additional boundary conditions specified that are incorporated into the infrastructure automatically, in the case of scalar Gauss-Bonnet, for the scalar field, we require that it be regular on the horizon and that it asymptotically vanish. For other additional vector or tensor fields, additional boundary conditions can be

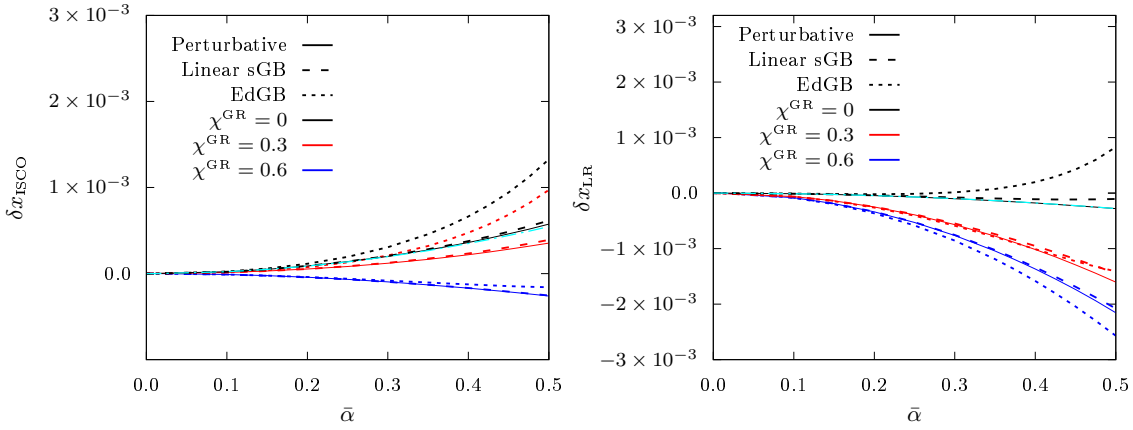

(a) Innermost stable circular orbit (b) Light ring

Figure 4.3: Fractional change in location of innermost stable circular orbit (left) and light ring (right) vs dimensionless coupling $\bar{\alpha}$ for three dimensionless GR spin values, $\chi = 0, 0.3$, and 0.6 denoted by the black, red, and blue colors respectively. The perturbative solution is denoted by the solid line, the sGB solution by the dashed line, and the EdGB solution denoted by the dotted line. We have also included the analytic perturbative solution in spherical symmetry as the dashed cyan colored line. Here again we recover the very good agreement between the perturbative solution and the linear sGB solution in the nonrotating limit and the discrepancy of the EdGB solution. We again find that the deviation away from GR is suppressed for increased values of the spin.

incorporated automatically in the same manner.

Furthermore, our infrastructure is free and open to the public so that the scientific community can utilize it as a tool to explore exotic black hole spacetimes. The analytical fitted models constructed from the solutions can be used to calculate astrophysical observables such as accretion disks around black holes [8], shadows of black holes [16], or quasinormal modes of black hole mergers [25], allowing for realistic data analysis investigations with Bayesian methods.

The remainder of this paper is organized as follows. Section 4 outlines adjustments that are required to extend the numerical algorithm to partial differential equations in axial symmetry. Section 4 validates the algorithm using a rotating Kerr

black hole. Section 4 applies the algorithm to sGB gravity and derives the results described above. Section 4 constructs a fitted analytical model from the numerical solutions and compares physical observables determined by the numerical solutions and the fits. Finally, Section 4 summarizes our results and points to future directions. For the remainder of this paper we use the following conventions: Greek letters denote spacetime indices; the metric has the spacetime signature $(-,+,+,+)$; we use geometric units where $G = 1 = c$.

Numerical Methods

The numerical infrastructure extends recent work from [90] to axial symmetry, following the approach in [60, 83], to build a partial differential equation solver for rotating black hole solutions in an arbitrary modified theory of gravity. The infrastructure uses a relaxed Newton-Raphson method to solve the discretized partial differential equations in two dimensions. The field equations are discretized using a Newton interpolation polynomial which naturally introduces discretization errors that must be controlled. As most of the foundations of this infrastructure is detailed in [90], we will focus on the extensions to axisymmetry in this section.

In axisymmetry, the Newton interpolation polynomial and the discretization error remains identical to the spherical symmetry case but with an additional dimension. Specifically, we replace each $\frac{\partial u}{\partial x}$ and $\frac{\partial u}{\partial y}$ operator with their discretized equivalents which introduces their respective discretization errors

$$\begin{aligned} \partial_x \vec{\boldsymbol{e}}_{(x,d)} &= \partial_x \vec{\boldsymbol{u}}_d^{(r+2)} - \partial_x \vec{\boldsymbol{u}}_d^{(r)}, \\ \partial_{xx} \vec{\boldsymbol{e}}_{(x,d)} &= \partial_{xx} \vec{\boldsymbol{u}}_d^{(r+2)} - \partial_{xx} \vec{\boldsymbol{u}}_d^{(r)}, \end{aligned} \tag{4.1}$$

$$\begin{aligned}\partial_y \vec{\boldsymbol{e}}_{(y,d)} &= \partial_y \vec{\boldsymbol{u}}_d^{(r+2)} - \partial_y \vec{\boldsymbol{u}}_d^{(r)}, \\ \partial_{yy} \vec{\boldsymbol{e}}_{(y,d)} &= \partial_{yy} \vec{\boldsymbol{u}}_d^{(r+2)} - \partial_{yy} \vec{\boldsymbol{u}}_d^{(r)}.\end{aligned} \tag{4.2}$$

where $\vec{\boldsymbol{e}}_{(x,d)}$ and $\vec{\boldsymbol{e}}_{(y,d)}$ are the discretized error vectors[1] at each grid point in the x and y dimension respectively. $\vec{\boldsymbol{u}}_d^{(r)}$ is the discretized solution vector $\vec{\boldsymbol{u}}$ that we wish to minimize to the Newton polynomial order r. With now two discretization errors, we obtain an additional discretization error correction equation that must be minimized

$$\boldsymbol{\mathcal{J}} \Delta \vec{\boldsymbol{u}}_{y,e} = -\vec{\boldsymbol{D}}_{y,e}, \tag{4.3}$$

where $\boldsymbol{\mathcal{J}}$ is the Jacobian matrix, $\Delta \vec{\boldsymbol{u}}_{y,e}$ is the correction on the solution vector $\vec{\boldsymbol{u}}$ due to the discretization error vector $\vec{\boldsymbol{D}}_{y,e}$ in the y-dimension. This additional equation must be minimized along with our two previous equations

$$\boldsymbol{\mathcal{J}} \Delta \vec{\boldsymbol{u}}_d = -\vec{\boldsymbol{b}}_d, \tag{4.4}$$

$$\boldsymbol{\mathcal{J}} \Delta \vec{\boldsymbol{u}}_{x,e} = -\vec{\boldsymbol{D}}_{x,e}. \tag{4.5}$$

To control the discretization error, we require that the relative correction due to both the x and y-dimension ($\vec{\boldsymbol{u}}_{x,e}$ and $\vec{\boldsymbol{u}}_{y,e}$) discretization error is below a specified tolerance,

$$\frac{\|\Delta \vec{\boldsymbol{u}}_{x,e}\|}{\|\vec{\boldsymbol{u}}_d\|} \leq \text{tol}, \tag{4.6}$$

$$\frac{\|\Delta \vec{\boldsymbol{u}}_{y,e}\|}{\|\vec{\boldsymbol{u}}_d\|} \leq \text{tol}. \tag{4.7}$$

The main addition from spherical to axisymmetry is the treatment of mixed

[1] In this paper, the word *vector* stands for a standard Euclidean vector in flat space.

derivatives. We utilize the method in [83] and treat each mixed derivative as a separate field equation. Namely by defining a new auxiliary variable

$$\frac{\partial u_0}{\partial y} = u_1, \tag{4.8}$$

and substituting it into each mixed derivative operator,

$$\frac{\partial^2 u_0}{\partial x \partial y} = \frac{\partial u_1}{\partial x}. \tag{4.9}$$

We then treat the auxiliary variable definition of Eq. (4.8) as a separate field equation whose residual we simultaneously must minimize

$$\frac{\partial u_0}{\partial y} - u_1 = b_1, \tag{4.10}$$

which will double the amount of differential equations we must solve. If the problem of interest does not contain any relevant mixed derivatives (which is the case for our chosen ansatz in GR) this step may be skipped. Unfortunately, in general this is not the case.

The resulting system of linear of equations as a result of the relaxed Newton-Raphson method changed the linear system solver method. In the spherically symmetric case, iterative solver methods were comparable but had faster convergence over direct methods. In the axisymmetric case, the field equations become less diagonally dominant and iterative methods fail to successfully accelerate the computation time. Due to this, we find that direct methods once again become the faster method because the size of our linear system is not large enough (on the order of millions of elements) for the iterative methods to accelerate convergence.

Validation

We will now apply our numerical infrastructure using the method described in the previous section to a stationary rotating black hole in general relativity described by the Kerr metric. Although the solution is known analytically, we can use it to benchmark our numerical infrastructure.

The familiar Einstein-Hilbert action in General Relativity in a vacuum is given by

$$S = \frac{1}{16\pi} \int d^4x \sqrt{-g}\, R\,, \tag{4.11}$$

where R is the Ricci scalar and g is the determinant of the metric $g_{\mu\nu}$. Varying the action with respect to the metric gives the vacuum Einstein field equations

$$G_{\mu\nu} = 0\,, \tag{4.12}$$

where $G_{\mu\nu}$ is the Einstein tensor.

We begin with an axisymmetric and stationary metric ansatz in isotropic coordinates,[2]

$$ds^2 = -f(\rho,\theta)dt^2 + \frac{m(\rho,\theta)}{f(\rho,\theta)}\left(d\rho^2 + \rho^2 d\theta^2\right) + \frac{l(\rho,\theta)}{f(\rho,\theta)}\rho^2 \sin^2\theta \left(d\phi - \frac{\omega(\rho,\theta)}{\rho}dt\right)^2, \tag{4.13}$$

where ρ is the isotropic radial coordinate, which is related to the Boyer-Lindquist

[2]Note that this is a slightly modified ansatz from [90]. This ansatz produces field equations that are easier to diagonalize as we will see later.

radial coordinate by

$$\begin{aligned} r &= \rho \left(1 + \frac{M_0 + a_0}{2\rho}\right)\left(1 + \frac{M_0 - a_0}{2\rho}\right), \\ &= \rho + M_0 + \frac{M_0^2 - a_0^2}{4\rho}. \end{aligned} \tag{4.14}$$

Here M_0 is the bare mass and a_0 is the spin of the black hole. As with the Kerr metric in Boyer-Lindquist coordinates, the Kerr metric in isotropic coordinates has two parameters, the bare mass and the spin. As we shall see below, it is convenient to replace the spin parameter a_0 with the event horizon radius $\rho_{\rm H}$. We define the spin as

$$a_0 \equiv \sqrt{M_0^2 - 4\rho_{\rm H}^2}, \tag{4.15}$$

and replace it in the above coordinate transformation,

$$r = \rho + M_0 + \frac{\rho_{\rm H}^2}{\rho}. \tag{4.16}$$

The Kerr metric in isotropic coordinates is

$$\begin{aligned} f_{\rm GR} &= \left(1 - \frac{\rho_{\rm H}^2}{\rho^2}\right)^2 \frac{F_1}{F_2}, \\ m_{\rm GR} &= \left(1 - \frac{\rho_{\rm H}^2}{\rho^2}\right)^2 \frac{F_1^2}{F_2}, \\ l_{\rm GR} &= \left(1 - \frac{\rho_{\rm H}^2}{\rho^2}\right)^2, \\ \omega_{\rm GR} &= \frac{F_3}{F_2}, \end{aligned} \tag{4.17}$$

where

$$
\begin{aligned}
F_1 &= \frac{2M_0^2}{\rho^2} + \left(1 - \frac{\rho_{\rm H}^2}{\rho^2}\right)^2 + \frac{2M_0}{\rho}\left(1 + \frac{\rho_{\rm H}^2}{\rho^2}\right) - \frac{M_0^2 - 4\rho_{\rm H}^2}{\rho^2}\sin^2\theta, \\
F_2 &= \left[\frac{2M_0^2}{\rho^2} + \left(1 - \frac{\rho_{\rm H}^2}{\rho^2}\right)^2 + \frac{2M_0}{\rho}\left(1 + \frac{\rho_{\rm H}^2}{\rho^2}\right)\right]^2 - \left(1 - \frac{\rho_{\rm H}^2}{\rho^2}\right)^2 \frac{M_0^2 - 4\rho_{\rm H}^2}{\rho^2}\sin^2\theta, \\
F_3 &= \frac{2M_0\sqrt{M_0^2 - 4\rho_{\rm H}^2}\left(1 + \frac{M_0}{\rho} + \frac{\rho_{\rm H}^2}{\rho^2}\right)}{\rho^2}.
\end{aligned}
\tag{4.18}
$$

We can notice a few things about the Kerr metric in these coordinates. First, on the event horizon, $f_{\rm GR}|_{\rho=\rho_{\rm H}} = m_{\rm GR}|_{\rho=\rho_{\rm H}} = l_{\rm GR}|_{\rho=\rho_{\rm H}} = 0$. Second, on the event horizon, the frame dragging term ω is a constant

$$
\omega|_{\rho=\rho_{\rm H}} = \omega_{\rm H} = \frac{\rho_{\rm H}\sqrt{M_0^2 - 4\rho_{\rm H}^2}}{2M_0\left(M_0 + 2\rho_{\rm H}\right)}, \tag{4.19}
$$

and is proportional to the angular velocity of the black hole $\Omega_{\rm H}$,

$$
\Omega_{\rm H} = \frac{\omega_{\rm H}}{\rho_{\rm H}} = \frac{\sqrt{M_0^2 - 4\rho_{\rm H}^2}}{2M_0\left(M_0 + 2\rho_{\rm H}\right)}. \tag{4.20}
$$

Third, the non-rotating Schwarzschild limit is equivalent to $M_0 = 2\rho_{\rm H}$ and in this limit,

$$
\begin{aligned}
f_{\rm GR}^{\rm SCHW} &= \frac{\left(1 - \frac{\rho_{\rm H}}{\rho}\right)^2}{\left(1 + \frac{\rho_{\rm H}}{\rho}\right)^2}, \\
m_{\rm GR}^{\rm SCHW} &= \left(1 - \frac{\rho_{\rm H}}{\rho}\right)^2\left(1 + \frac{\rho_{\rm H}}{\rho}\right)^2, \\
l_{\rm GR}^{\rm SCHW} &= m_{\rm GR}^{\rm SCHW}, \\
\omega_{\rm GR}^{\rm SCHW} &= 0.
\end{aligned}
\tag{4.21}
$$

Fourth, along the symmetry axis $\theta = 0$ and $\theta = \pi$, by requiring our solutions to be regular along this axis we expect our metric functions to satisfy the boundary conditions

$$\begin{aligned} \frac{\partial f}{\partial \theta}|_{\theta=0,\pi} &= 0, \\ \frac{\partial m}{\partial \theta}|_{\theta=0,\pi} &= 0, \\ \frac{\partial l}{\partial \theta}|_{\theta=0,\pi} &= 0, \\ \frac{\partial \omega}{\partial \theta}|_{\theta=0,\pi} &= 0, \end{aligned} \tag{4.22}$$

which our solution does satisfy. Lastly, as expected, the metric is asymptotically flat, $f_{\rm GR}|_{\rho\to\infty} = m_{\rm GR}|_{\rho\to\infty} = l_{\rm GR}|_{\rho\to\infty} = 1$ and $\omega_{\rm GR}|_{\rho\to\infty} = 0$. Asymptotically far away, the observable mass and angular momentum can be extracted from the decay of the metric components

$$\begin{aligned} g_{tt} &= -f + \frac{l}{f}\omega^2 \sin^2\theta = -1 + \frac{2M}{\rho} + \mathcal{O}\left(\frac{1}{\rho^2}\right), \\ g_{t\phi} &= -\frac{l}{f}\omega\rho \sin^2\theta = -\frac{2J}{\rho}\sin^2\theta + \mathcal{O}\left(\frac{1}{\rho^2}\right), \end{aligned} \tag{4.23}$$

where M and J are the Arnowit-Deser-Misner (ADM) mass and angular momentum respectively. For the Kerr solution, we find $M_{\rm GR} = M_0$ and $J_{\rm GR} = M_0\sqrt{M_0^2 - 4\rho_{\rm H}^2}$.

With this ansatz, we can compute the components of the Einstein tensor $G_{\mu\nu}$. To simplify the partial differential equations, following [60], we use linear combinations of the Einstein tensor to diagonalize the equations with respect to the operator $\hat{\mathcal{O}} =$

$\frac{\partial^2}{\partial\rho^2} + \frac{1}{\rho^2}\frac{\partial^2}{\partial\theta^2}$,

$$\begin{aligned}
\frac{m}{f}\left(G^{\mu}{}_{\mu} - 2G^{t}{}_{t} - \frac{2\omega}{\rho}G^{t}{}_{\phi}\right) &= \frac{1}{f}\hat{\mathcal{O}}f + \ldots, \\
2\frac{m}{f}\left(G^{\phi}{}_{\phi} - \frac{\omega}{\rho}G^{t}{}_{\phi}\right) &= \frac{1}{m}\hat{\mathcal{O}}m + \ldots, \\
2\frac{m}{f}\left(G^{\rho}{}_{\rho} + G^{\theta}{}_{\theta}\right) &= \frac{1}{l}\hat{\mathcal{O}}l + \ldots, \\
2\frac{f\,m}{l\,\sin^2\theta}\left(-\frac{1}{\rho}G^{t}{}_{\phi}\right) &= \hat{\mathcal{O}}\omega + \ldots.
\end{aligned} \tag{4.24}$$

As in the spherical symmetry case, we again use a compactified coordinate defined by

$$x = 1 - \frac{\rho_{\mathrm{H}}}{\rho}. \tag{4.25}$$

This changes our domain of integration from $\rho \in [\rho_{\mathrm{H}}, \infty)$ to the finite domain $x \in [0, 1]$. In these compactified isotropic coordinates, the Kerr metric has the form

$$\begin{aligned}
f_{\mathrm{GR}} &= x^2\,(x-2)^2\,\frac{F_1^{\mathrm{x}}}{F_2^{\mathrm{x}}}, \\
m_{\mathrm{GR}} &= x^2\,(x-2)^2\,\frac{(F_1^{\mathrm{x}})^2}{F_2^{\mathrm{x}}}, \\
l_{\mathrm{GR}} &= x^2\,(x-2)^2\,, \\
\omega_{\mathrm{GR}} &= \frac{F_3^{\mathrm{x}}}{F_2^{\mathrm{x}}},
\end{aligned} \tag{4.26}$$

where $F_1^{\mathrm{x}}, F_2^{\mathrm{x}}$, and F_3^{x} are the functions from Eq. (4.18) in compactified coordinates. As before, we have similar boundary conditions, $f_{\mathrm{GR}}|_{x=0} = m_{\mathrm{GR}}|_{x=0} = l_{\mathrm{GR}}|_{x=0} = 0$ and $\omega_{\mathrm{GR}}|_{x=0} = \omega_{\mathrm{H}}$. At infinity we have $f_{\mathrm{GR}}|_{x=1} = m_{\mathrm{GR}}|_{x=1} = l_{\mathrm{GR}}|_{x=1} = 1$ and $\omega_{\mathrm{GR}}|_{x=1} = 0$.

To prepare our field equations for numerical integration, we make an additional substitution following [59]. We find that this substitution is necessary to eliminate a numerical divergence on the event horizon in the scalar Gauss-Bonnet case that will

be considered in Sec. 4. We replace the metric functions

$$\begin{aligned} f &= x^2 \bar{f}, \\ m &= x^2 \bar{m}, \\ l &= x^2 \bar{l}, \end{aligned} \tag{4.27}$$

which removes this numerical divergence. This substitution keeps the boundary conditions as $x \to 1$ unchanged. At the horizon, the boundary conditions are obtained from examining an expansion of the metric functions around $x = 0$ and become

$$\begin{aligned} \left(\bar{f} - \frac{\partial \bar{f}}{\partial x}\right)|_{x=0} &= 0, \\ \left(\bar{m} + \frac{\partial \bar{m}}{\partial x}\right)|_{x=0} &= 0, \\ \left(\bar{l} + \frac{\partial \bar{l}}{\partial x}\right)|_{x=0} &= 0. \end{aligned} \tag{4.28}$$

Similar to the spherically symmetric case, the Newton-Raphson method requires an initial guess for the numerical system. We shall again, choose an initial guess that is a small perturbation away from the Kerr metric and that satisfies the boundary conditions

$$\begin{aligned} u_0^{(0)} &= f_{\rm GR}\left[1 + \delta\, \Delta x \Delta y\right], \\ u_1^{(0)} &= m_{\rm GR}\left[1 + \delta\, \Delta x \Delta y\right], \\ u_2^{(0)} &= l_{\rm GR}\left[1 + \delta\, \Delta x \Delta y\right], \\ u_3^{(0)} &= \omega_{\rm GR}\left[1 + \delta\, \Delta x \Delta y\right], \end{aligned} \tag{4.29}$$

where $\delta = 0.1$ and can be adjusted to improve or worsen the initial guess.[3] The

[3]We find that the convergence in GR is largely independent of the value of δ. Even initial guess values as large as $\delta = 1$ converge to the desired solution in less than 10 iterations.

normalized functions Δx and $\Delta\theta$ are given by

$$\begin{aligned}\Delta x &= \frac{256}{27}x^3\left(1-x\right),\\ \Delta y &= \frac{512}{\pi^3}\left(\frac{\theta}{\pi/2}\right)^3\left(1-\frac{\theta}{\pi/2}\right)^3.\end{aligned} \tag{4.30}$$

To solve our problem numerically, we begin by replacing the metric functions of our ansatz with their barred definitions of Eq. (4.27). We then define the auxiliary mixed derivative functions

$$\begin{aligned}\frac{\partial\bar{f}}{\partial\theta} &\equiv u_4,\\ \frac{\partial\bar{m}}{\partial\theta} &\equiv u_5,\\ \frac{\partial\bar{l}}{\partial\theta} &\equiv u_6,\\ \frac{\partial\omega}{\partial\theta} &\equiv u_7,\end{aligned} \tag{4.31}$$

and replace each mixed derivative operator given by[4]

$$\begin{aligned}\frac{\partial^2\bar{f}}{\partial x\partial\theta} &= \frac{\partial u_4}{\partial x},\\ \frac{\partial^2\bar{m}}{\partial x\partial\theta} &= \frac{\partial u_5}{\partial x},\\ \frac{\partial^2\bar{l}}{\partial x\partial\theta} &= \frac{\partial u_6}{\partial x},\\ \frac{\partial^2\omega}{\partial x\partial\theta} &= \frac{\partial u_7}{\partial x},\end{aligned} \tag{4.32}$$

in the diagonalized Einstein equations of Eq. (4.24) in compactified isotropic coordinates. From Eq. (4.10), the mixed derivative definitions above add 4 additional field equations we must solve simultaneously with the Einstein equations and we

[4]We find that it is unnecessary to make the second order replacement $\frac{\partial^2\bar{f}}{\partial\theta^2} = \frac{\partial u_4}{\partial\theta}$ as the second derivative $\frac{\partial^2\bar{f}}{\partial\theta^2}$ terms can be evaluated very accurately with our Newton polynomial representation. We find that this substitution only slows down convergence.

obtain a nonlinear system of 8 partial differential equations for our 8 functions to solve: $\bar{f}, \bar{m}, \bar{l}, \omega, u_4, u_5, u_6, u_7$.

We then discretize our differential operators using their Newton polynomial representation of order $r = 16$ on a 2-dimensional grid of 61×31 points and initialize our solver with the initial guess of Eq. (4.29). The two input parameters that we must specify is the horizon radius where we choose $\rho_{\rm H}$ and the angular velocity on the event horizon $\Omega_{\rm H}$. For all computations in this paper, we set $\rho_{\rm H} = 1$, which for a nonrotating black hole in GR corresponds to a black hole mass of $M_0 = 1/2$. The horizon angular velocity is chosen to coincide with a Kerr black hole of dimensionless spin $\chi^{\rm GR} = 0.6$ which from Eq. (4.20), $\Omega_{\rm H} = 0.0666$. We find that our numerical infrastructure converges to the desired solution below our specified tolerance of tol $= 10^{-5}$ in 4 iterations. The absolute error between the metric functions and the Kerr solution for each iteration is shown in Fig. 4.4.

Axially Symmetric Black Holes in Scalar-Gauss-Bonnet Gravity

In this section we solve the modified Einstein field equations in sGB gravity with both a linear coupling and an exponential coupling function, assuming a vacuum spacetime that is stationary and axially symmetric.

Action and Field equations

The action in scalar-Gauss-Bonnet gravity in a vacuum is given by

$$S = \frac{1}{16\pi} \int d^4x \sqrt{-g} \left[R - \beta \, \nabla_\mu \psi \nabla^\mu \psi + 2 \, \alpha F(\psi) \mathcal{G} \right], \tag{4.33}$$

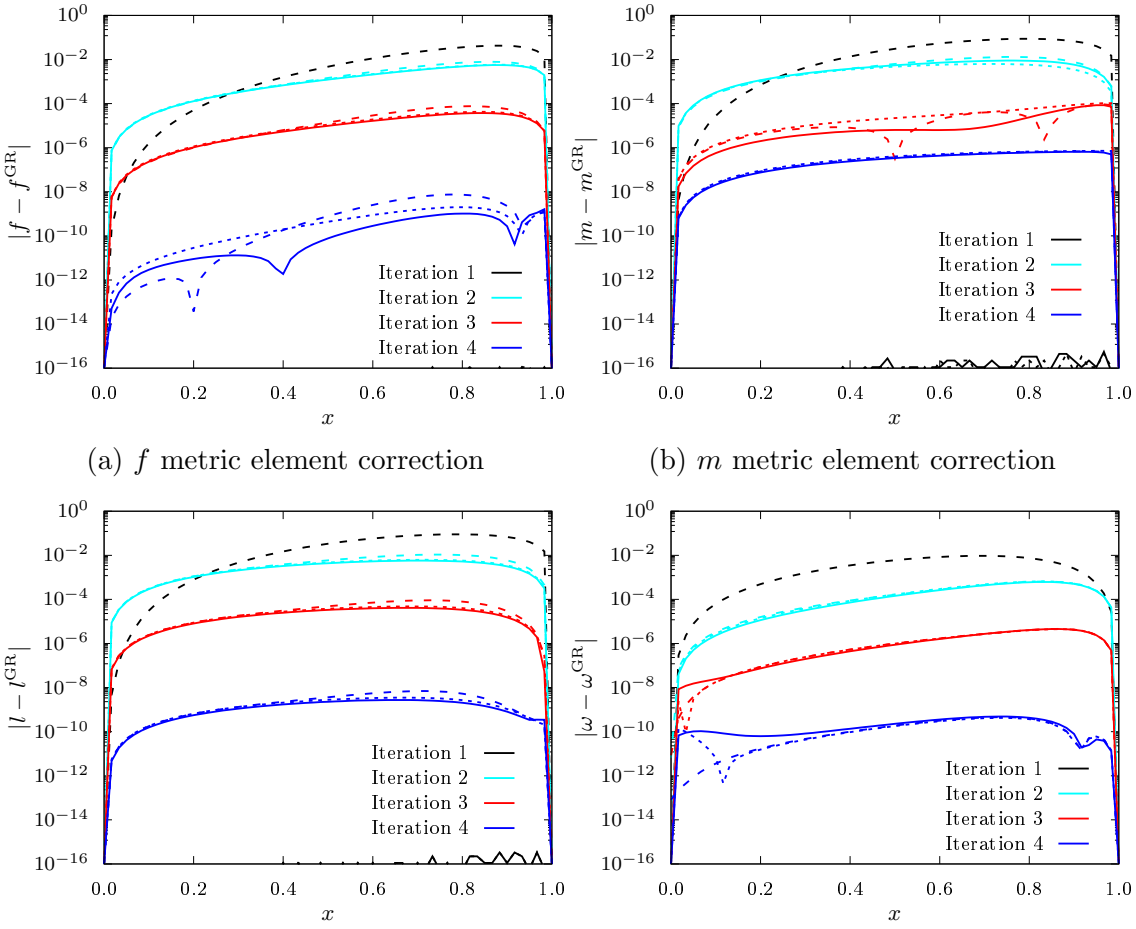

(a) f metric element correction

(b) m metric element correction

(c) l metric element correction

(d) ω metric element correction

Figure 4.4: Absolute error during each iteration (colored) for each metric element to the Kerr solution for three selected angles. Here we show the metric components f (top left), m (top right), l (bottom left) and ω (bottom right) for each iteration denoted by color and for three angles $\theta = 0, \pi/4, \pi/2$ denoted by the dotted, dashed, and solid lines respectively. We find that with our chosen initial guess, our numerical infrastructure converges to the Kerr solution to a maximum absolute error of $\mathcal{O}(10^{-6})$ and a minimum error of $\mathcal{O}(10^{-10})$ in 4 iterations.

where R is the Ricci scalar and g is the determinant of the metric $g_{\mu\nu}$. The real dimensionless scalar field ψ is coupled to the Gauss-Bonnet invariant $\mathcal{G}$ where

$$\mathcal{G} = R^2 - 4R^{\mu\nu}R_{\mu\nu} + R^{\mu\nu\rho\sigma}R_{\mu\nu\rho\sigma}, \tag{4.34}$$

through a function of the scalar field $F(\psi)$ with a coupling constant α which has dimensions length squared. We will keep the coupling constant β explicit in this section, but in all computation we set $\beta = 1$, as it can be eliminated through a redefinition of the scalar field ψ and the coupling constant α.

By varying the action with respect to the metric and the scalar field we obtain two field equations. Variation with respect to the metric field yields

$$G_{\mu\nu} - \beta\, T_{\mu\nu} + \alpha\, K_{\mu\nu} = 0, \tag{4.35}$$

where the scalar field stress-energy tensor is

$$T_{\mu\nu} = \nabla_\mu\psi\nabla_\nu\psi - \frac{1}{2}g_{\mu\nu}\nabla^\gamma\psi\nabla_\gamma\psi, \tag{4.36}$$

and

$$K_{\mu\nu} = \left(g_{\rho\mu}g_{\delta\nu} + g_{\rho\nu}g_{\delta\mu}\right)\nabla_\sigma\left[\epsilon^{\gamma\delta\alpha\beta}\epsilon^{\rho\sigma\lambda\eta}R_{\lambda\eta\alpha\beta}\nabla_\gamma F(\psi)\right]. \tag{4.37}$$

Variation with respect to the scalar field yields

$$\beta\Box\psi + \alpha\,\frac{\partial F}{\partial\psi}\mathcal{G} = 0. \tag{4.38}$$

The scalar field is subject to the following boundary conditions: it must be asymptotically flat, and its first derivative must vanish on the horizon in isotropic

coordinates, namely

$$\frac{\partial\psi}{\partial\rho}|_{\rho\to\rho_{\rm H}}=0,\qquad \psi|_{\rho\to\infty}=0. \tag{4.39}$$

In this paper we will consider two coupling functions typically explored in sGB gravity,

$$\begin{aligned} F(\psi)&=\psi \quad \leftrightarrow \text{ linear sGB}\,,\\ F(\psi)&=e^{\psi} \ \leftrightarrow \text{ EdGB}\,. \end{aligned} \tag{4.40}$$

Linear Scalar-Gauss-Bonnet Gravity

In the linear coupling theory $F(\psi)=\psi$, we numerically solve the field equations for an axially symmetric black hole perturbatively in the coupling α. If we assume the dimensionless coupling $\bar{\alpha}^2\ll 1$ where $r_{\rm H}$ sets the order of the curvature length of the system, we can perturbatively expand our metric as

$$g_{\mu\nu}=g^{(0)}_{\mu\nu}+\epsilon g^{(1)}_{\mu\nu}+\epsilon^2 g^{(2)}_{\mu\nu}, \tag{4.41}$$

where ϵ is a bookkeeping parameter, $\epsilon\ll 1$, and $\alpha=\mathcal{O}(\epsilon)$. This expansion with our metric ansatz is,

$$\begin{aligned} f&=f_0+\epsilon f_1+\epsilon^2 f_2,\\ m&=m_0+\epsilon m_1+\epsilon^2 m_2,\\ l&=l_0+\epsilon l_1+\epsilon^2 l_2,\\ \omega&=\omega_0+\epsilon\omega_1+\epsilon^2\omega_2,\\ \psi&=\psi_0+\epsilon\psi_1+\epsilon^2\psi_2, \end{aligned} \tag{4.42}$$

We can then substitute this ansatz into our field equations and expand order by order in ϵ.

To $\mathcal{O}(\epsilon^0)$, we find

$$\begin{aligned} G^{(0)}_{\mu\nu} - \beta T^{(0)}_{\mu\nu} &= 0, \\ \Box^{(0)}\psi^{(0)} &= 0, \end{aligned} \tag{4.43}$$

where $G^{(0)}_{\mu\nu}, T^{(0)}_{\mu\nu}$, and $\Box^{(0)}$ are the Einstein tensor, scalar field stress-energy tensor, and the d'Alambertian evaluated from the background metric $g^{(0)}_{\mu\nu}$ respectively. By imposing asymptotic flatness and regularity on the horizon of the scalar field, we find $\psi^{(0)} = 0$ which implies that $T^{(0)}_{\mu\nu} = 0$. As expected we then see that $g^{(0)}_{\mu\nu}$ is the solution to $G^{(0)}_{\mu\nu} = 0$ which is the Kerr metric and each f_0, m_0, l_0, ω_0 correspond to their respective Kerr values from Eq. (4.26).

At $\mathcal{O}(\epsilon)$, we find

$$\begin{aligned} G^{(1)}_{\mu\nu} - \beta T^{(1)}_{\mu\nu} + \alpha\, K^{(0)}_{\mu\nu} &= 0, \\ \beta\left(\Box^{(1)}\psi^{(0)} + \Box^{(0)}\psi^{(1)}\right) + \alpha\, \mathcal{G}^{(0)} &= 0. \end{aligned} \tag{4.44}$$

Since $\psi^{(0)} = 0$ from before, we know $K^{(0)}_{\mu\nu} = 0$. Additionally, $T^{(1)}_{\mu\nu} = 0$ because the stress-energy tensor is $\mathcal{O}(\psi^2)$. Thus the metric perturbation at $\mathcal{O}(\epsilon)$ vanishes, $g^{(1)}_{\mu\nu} = 0$ and $f_1 = m_1 = l_1 = \omega_1 = 0$. The scalar field equation then simplifies to

$$\beta\, \Box^{(0)}\psi^{(1)} + \alpha\, \mathcal{G}^{(0)} = 0. \tag{4.45}$$

In spherical symmetry, the scalar field correction at this order can be calculated analytically [87, 88, 104].

At $\mathcal{O}(\epsilon^2)$, the modified field equations are

$$G^{(2)}_{\mu\nu} - \beta T^{(2)}_{\mu\nu} + \alpha\, K^{(1)}_{\mu\nu} = 0, \tag{4.46}$$

$$\beta\left(\Box^{(2)}\psi^{(0)} + \Box^{(1)}\psi^{(1)} + \Box^{(0)}\psi^{(2)}\right) + \alpha\,\mathcal{G}^{(1)} = 0. \tag{4.47}$$

Because $g^{(1)}_{\mu\nu} = 0$, we know that $\Box^{(1)} = \mathcal{G}^{(1)} = 0$ which simplifies the scalar field equation to

$$\Box^{(0)}\psi^{(2)} = 0, \tag{4.48}$$

which implies that $\psi^{(2)} = 0$ by imposing asymptotic flatness and regularity on the horizon. Thus the nontrivial modified field equations of interest are Eqs. (4.45) and (4.46). In spherical symmetry [87, 88, 104] and in the slow rotation limit [15, 30, 66, 69, 72], these equations can be analytically solved order by order because the scalar field equation is sourced by the Gauss-Bonnet invariant evaluated on the unperturbed background. In spherical symmetry, in our compactified coordinate system (4.25) the perturbed solution to second order is,

$$\begin{aligned}
f_2^{\rm SPH} &= \frac{\alpha^2 x^2\,(x-1)}{4620\beta\rho_{\rm H}^4\,(x-2)^{14}}\Big[1117x^{10} - 24574x^9 + 246510x^8 - 1415920x^7 + 4941728x^6 \\
&\quad - 10150448x^5 + 11892496x^4 - 7411712x^3 + 2000768x^2 - 98560x + 19712\Big], \\
m_2^{\rm SPH} &= -\frac{8\alpha^2 x^2\,(x-1)^2}{1155\beta\rho_{\rm H}^4\,(x-2)^{10}}\Big[71x^8 - 1420x^7 + 11554x^6 - 49788x^5 + 118374x^4 \\
&\quad - 167280x^3 + 147600x^2 - 78720x + 19680\Big], \\
l_2^{\rm SPH} &= m_2^{\rm SPH}, \\
\omega_2^{\rm SPH} &= 0, \\
\psi_1^{\rm SPH} &= \frac{\alpha\,(1-x)}{3\beta\rho_{\rm H}^2\,(x-2)^6}\left[3x^4 - 30x^3 + 118x^2 - 176x + 88\right].
\end{aligned} \tag{4.49}$$

In axial symmetry, using a slow rotation expansion around the dimensionless spin $\chi = \frac{a}{M} \ll 1$, solutions have been found to $\mathcal{O}(\alpha^2, \chi^2)$ [15] and $\mathcal{O}(\alpha^{14}, \chi^5)$ [66]. We cannot directly compare these solutions in the slow rotation limit to the solutions in this work because they are calculated in different coordinate systems and a proper comparison would require calculating the solution to the same order in isotropic coordinates. Instead we solve will these equations directly without perturbatively expanding in rotation.

To solve Eqs. (4.45) and (4.46) we apply our numerical infrastructure to the partially decoupled nonlinear partial differential equations using the method described in Sec. 4. We could solve for the scalar field first using Eq. (4.45) and then use the result to solve Eq. (4.46) as is done analytically but we find no noticeable difference on the converged solution compared to solving both simultaneously which our code can already handle. This is possible because the scalar field equation is partially decoupled to the metric perturbation equations, namely the scalar field equation only depends on the known GR background to zeroth order and it converges very rapidly. Each successive iteration then only needs to minimize the metric perturbations. We choose an initial grid of 61×31 points and a Newton polynomial order $r = 16$. For the actual computation, we set $\rho_{\rm H} = 1$ which sets the bare mass of the black hole to $M_0 = 2$. We set the desired tolerance of the solution to tol $= 10^{-5}$ which is both placed on the residual and on the relative tolerance of the discretization correction. We use the spherically symmetric perturbed corrections of Eq. (4.49) as our initial guess and convergence typically occurs within 1 to 3 iterations. Figure 4.5 compares the numerical perturbed rotating solution to the analytically known spherically symmetric solution. From these plots, we can verify that the perturbative solution in the spherically symmetric limit ($\chi^{\rm GR} = 0$) exactly recovers the analytic spherically symmetric solution.

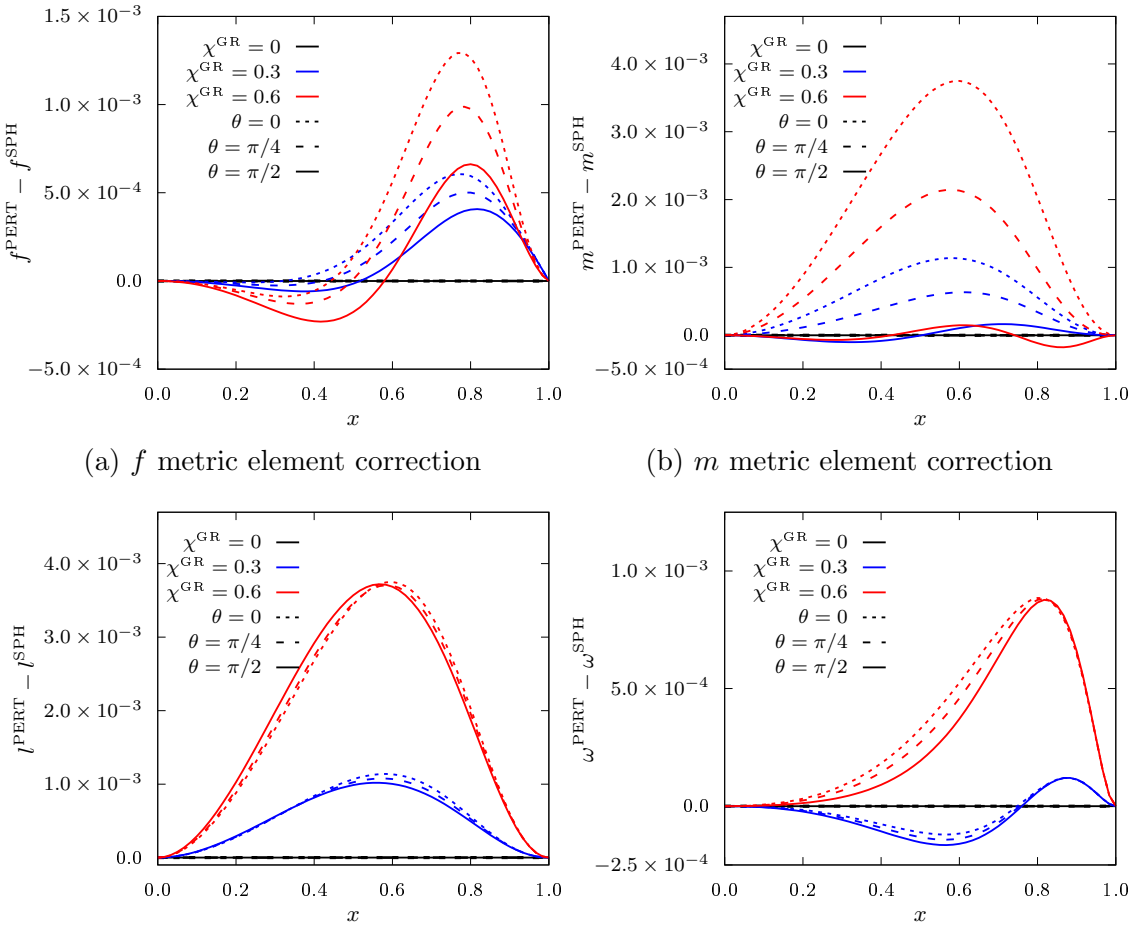

(a) f metric element correction

(b) m metric element correction

(c) l metric element correction

(d) ω metric element correction

Figure 4.5: Difference between metric elements for axisymmetric small coupling expansion and the analytic perturbative spherically symmetric solution for three selcted angles. Here we show the metric components f (top left), m (top right), l (bottom left) and ω (bottom right) for three dimensionless spin values $\chi = 0, 0.3, 0.6$ denoted by the black, blue, and red colors respectively and for three angles $\theta = 0, \pi/4, \pi/2$ denoted by the dotted, dashed, and solid lines respectively.

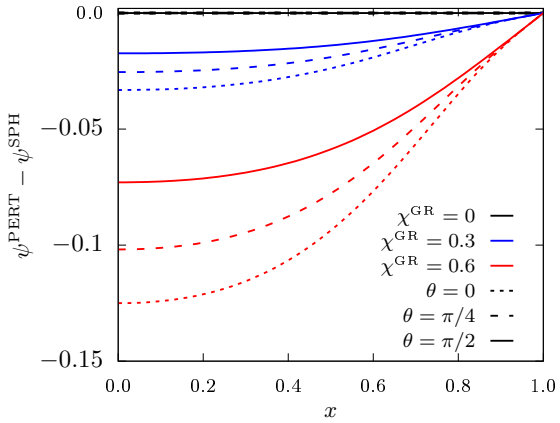

Figure 4.6: Difference between the axisymmetric small coupling expansion and the analytic perturbative spherically symmetric solution for scalar field for three selcted angles. The three dimensionless spin values $\chi = 0, 0.3, 0.6$ are denoted by the black, blue, and red colors respectively and the three angles $\theta = 0, \pi/4, \pi/2$ are denoted by the dotted, dashed, and solid lines respectively.

With this perturbed solution at hand, we can calculate the full nonlinear modified field equations in scalar Gauss-Bonnet gravity. The modified field equations are Eqs. (4.35) and (4.38) with $F(\psi) = \psi$. In Fig. 4.7 and 4.8 we show the difference between the full linear sGB solution and the Kerr solution for each metric element and the scalar field respectively for three different angles and three dimensionless spin values. It is important to note that the physical dimensionless spin parameter of the black hole is not given by $\chi^{\rm GR}$ as it will depend on α. We instead use the $\chi^{\rm GR}$ value to calculate the angular velocity of the event horizon from Eq. (4.20) which is the input parameter to our numerical infrastructure and will be identical for each solution of a given $\chi^{\rm GR}$. From a comparison of the sGB solution to Kerr for these dimensionless spin values, we again notice that the deviation is suppressed as the spin increases.

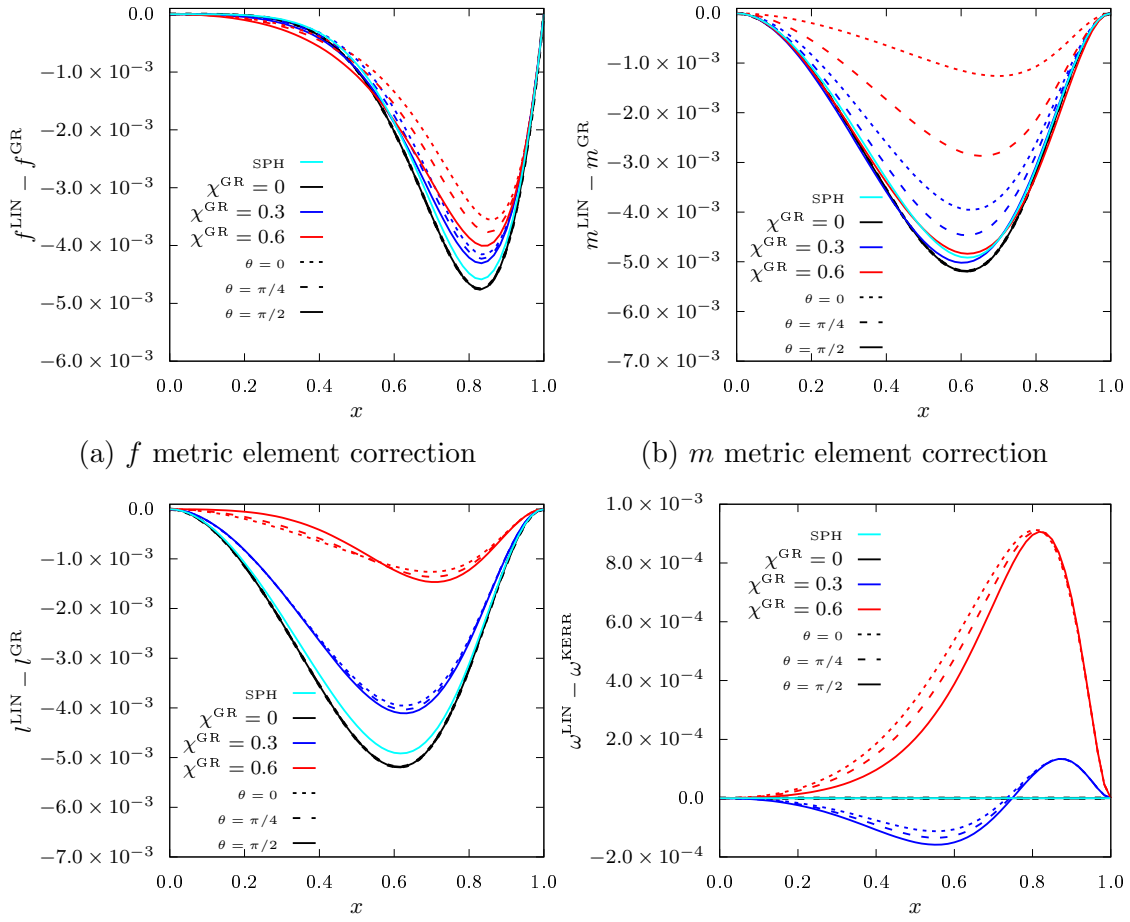

(a) f metric element correction

(b) m metric element correction

(c) l metric element correction

(d) ω metric element correction

Figure 4.7: Difference between metric elements for linear coupling function and the Kerr metric for three selcted angles. Here we show the metric components f (top left), m (top right), l (bottom left) and ω (bottom right) for three dimensionless spin values $\chi = 0, 0.3, 0.6$ denoted by the black, blue, and red colors respectively and for three angles $\theta = 0, \pi/4, \pi/2$ denoted by the dotted, dashed, and solid lines respectively. We also show the analytic perturbative spherically symmetric solutions in cyan. Notice how the nonrotating linear sGB solution has a larger deviation than the analytic perturbative spherically symmetric solution as expected but that this deviation is then suppressed for larger spin values.

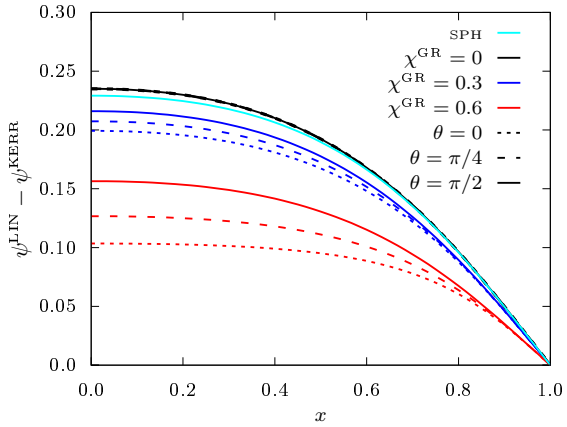

Figure 4.8: The scalar field using the linear coupling function for three selcted angles. The three dimensionless spin values $\chi = 0, 0.3, 0.6$ are denoted by the black, blue, and red colors respectively and the three angles $\theta = 0, \pi/4, \pi/2$ are denoted by the dotted, dashed, and solid lines respectively. The analytic perturbative spherically symmetric solution is in cyan. Like for the deviations of the metric functions, we find very good agreement between the nonrotating linear sGB scalar field and the analytic spherically symmetric perturbation but the scalar charge is suppressed for larger spin values.

Einstein-dilaton-Gauss-Bonnet Gravity

Let us now consider the case of an exponential coupling function. The resulting field equations are Eqs. (4.35) and (4.38) with $F(\psi) = e^{\psi}$. We find a numerical solution using the computational infrastructure of Sec. 4, with the same choices for the grid spacing, Newton polynomial order, etc as in the previous subsection. We show the results in Figs. 4.9 and 4.10. This time we find a much larger deviation from GR in the EdGB solutions than with the linear sGB coupling. We also find a much larger range of differences for the m metric function than for the f, l, and ω components. This is particularly interesting because this is coincidentally the metric function that has a negligible impact on the physical observables we have calculated. For example, as we will see in the next section, geodesics in an axially symmetric spacetime are completely independent of the g_{rr} component of the metric. This is not entirely true for an isotropic metric because $\rho^2 \sin^2\theta g_{\phi\phi} = g_{\rho\rho}$ but these results suggest that even in isotropic coordinates, the dependence on the $g_{\rho\rho}$ metric function is minimal. With our nonlinear numerical solutions at hand, we now use these solutions to construct analytical fitted models and we compare physical observables like the location of the innermost-stable-circular orbit and the light ring.

Properties of Solution

In this section we explore the physical properties of the numerical solutions found in the previous sections. We begin by finding analytical models that we fit to the data to provide accurate, closed-form expressions that allow for the rapid computation of physical observables. We then use the numerical results to calculate the location of the innermost stable circular orbit (ISCO) and the light ring (LR) by analyzing the motion of null and timelike geodesics. We will derive a modified theory of gravity

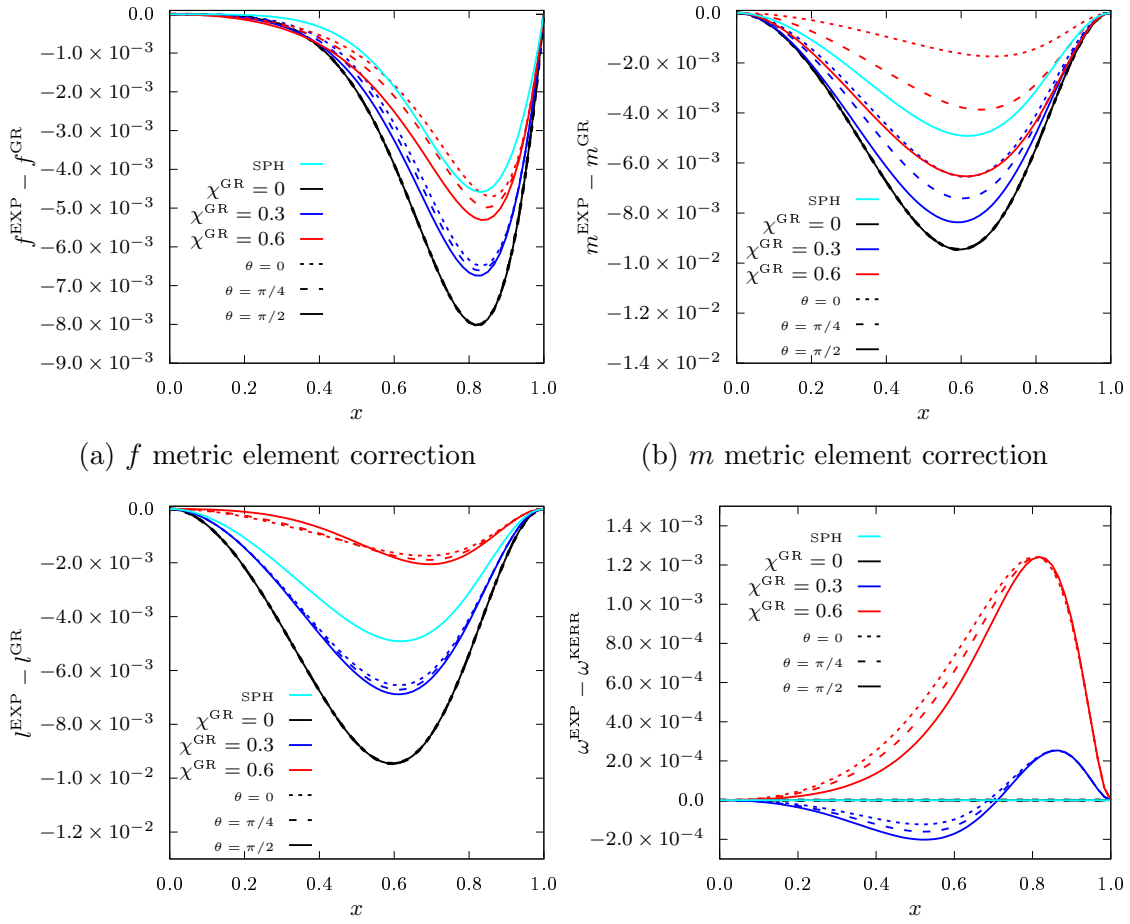

(a) f metric element correction

(b) m metric element correction

(c) l metric element correction

(d) ω metric element correction

Figure 4.9: Difference between metric elements for exponential coupling function and the Kerr metric for three selcted angles. Here we show the metric components f (top left), m (top right), l (bottom left) and ω (bottom right) for three dimensionless spin values $\chi = 0, 0.3, 0.6$ denoted by the black, blue, and red colors respectively and for three angles $\theta = 0, \pi/4, \pi/2$ denoted by the dotted, dashed, and solid lines respectively. We also show the analytic perturbative spherically symmetric solutions in cyan. We find a much larger deviation from GR than with the linear sGB coupling, as expected.

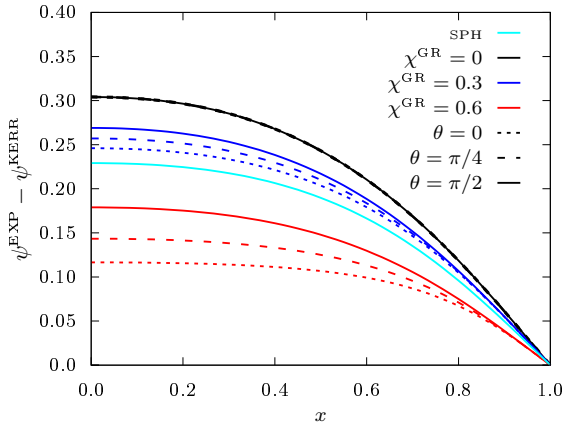

Figure 4.10: The scalar field using the exponential coupling function for three selcted angles. The three dimensionless spin values $\chi = 0, 0.3, 0.6$ are denoted by the black, blue, and red colors respectively and the three angles $\theta = 0, \pi/4, \pi/2$ are denoted by the dotted, dashed, and solid lines respectively. The analytic perturbative spherically symmetric solution is in cyan.

independent method to numerically calculate the location of the ISCO and the LR from only the symmetries of our spacetime.

Fitting Function

In the compactified coordinate system introduced in Eq. (4.25), the full nonlinear solutions for a given coupling α can be expressed as

$$\begin{aligned} f(x,\theta) &= f_{\rm GR} + f_{\rm nonlin}(x,\theta), \\ m(x,\theta) &= m_{\rm GR} + m_{\rm nonlin}(x,\theta), \\ l(x,\theta) &= l_{\rm GR} + l_{\rm nonlin}(x,\theta), \\ \omega(x,\theta) &= \omega_{\rm GR} + \omega_{\rm nonlin}(x,\theta), \\ \psi(x,\theta) &= \psi_{\rm nonlin}(x,\theta), \end{aligned} \tag{4.50}$$

where they are treated as corrections to the Kerr solution. We propose best fit models for the non-linear corrections of the form

$$
\begin{aligned}
f_{\rm nonlin}(x,\theta) &= x^2\,(x-1)\left(\sum_i\sum_j a_{i,j}x^i\theta^j\right),\\
m_{\rm nonlin}(x,\theta) &= x^2\,(x-1)^2\left(\sum_i\sum_j b_{i,j}x^i\theta^j\right),\\
l_{\rm nonlin}(x,\theta) &= x^2\,(x-1)^2\left(\sum_i\sum_j c_{i,j}x^i\theta^j\right),\\
\omega_{\rm nonlin}(x,\theta) &= \,(x-1)^2\left(\sum_i\sum_j d_{i,j}x^i\theta^j\right),\\
\psi_{\rm nonlin}(x,\theta) &= \,(x-1)\left(\sum_i\sum_j e_{i,j}x^i\theta^j\right),
\end{aligned}
\tag{4.51}
$$

and then fit these models to our numerical solutions to determine the constants $(a_{i,j}, b_{i,j}, c_{i,j}, d_{i,j}, e_{i,j})$ on the grid domain $x \in [0,1]$ and $\theta \in [0,\pi/2]$. The fitting order of our models is determined by systematically increasing the polynomial order of each function until the residual between the numerical solution and the model saturates. An example of some of the best-fit coefficients $(a_{i,j}, b_{k,l}, c_{m,n}, d_{p,q}, e_{r,s})$ are included in Appendix D, and they are available in a `Mathematica` file at `https://github.com/sullivanandrew/XPDES`. We plot the difference between both the numerical solutions and the fitted models for a coupling of $\alpha = 0.5$ and a spin $\chi^{\rm GR} = 0.6$ to the Kerr solution as well as the residuals between the models and the numerical data for the metric components and the scalar field for the linear sGB and EdGB solutions in Fig. 4.11, 4.12, 4.14, and 4.13. We find that the residual between the models and the numerical data is always below the specified tolerance on the numerical solution of $\mathcal{O}(10^{-5})$. Thus the fitted models can be treated as "exact" for practical applications to the specified tolerance.

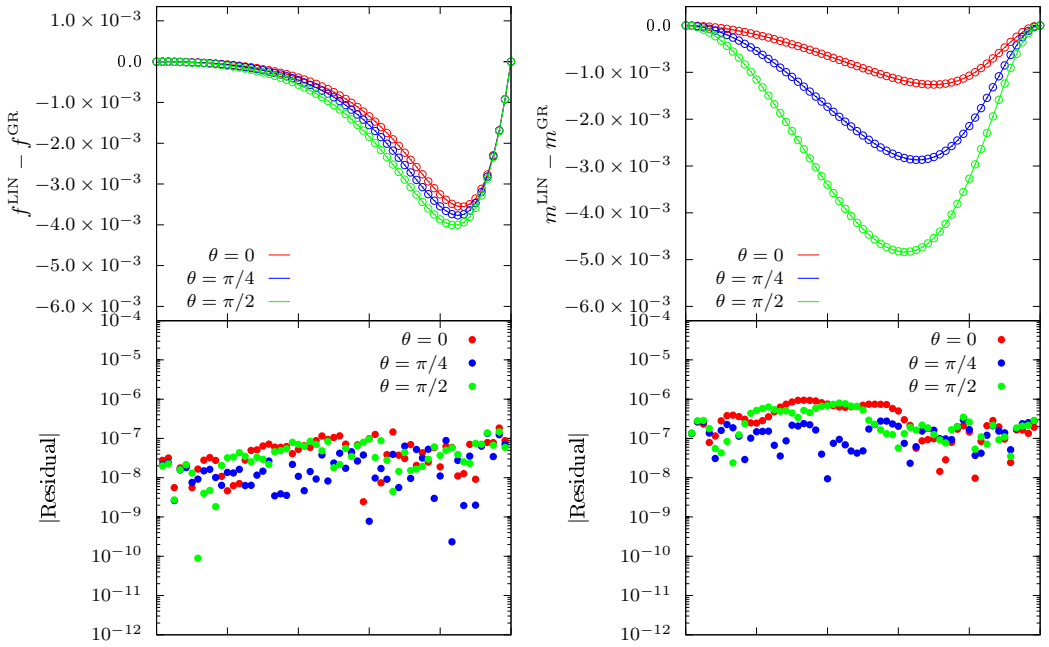

(a) f metric element residual

(b) m metric element residual

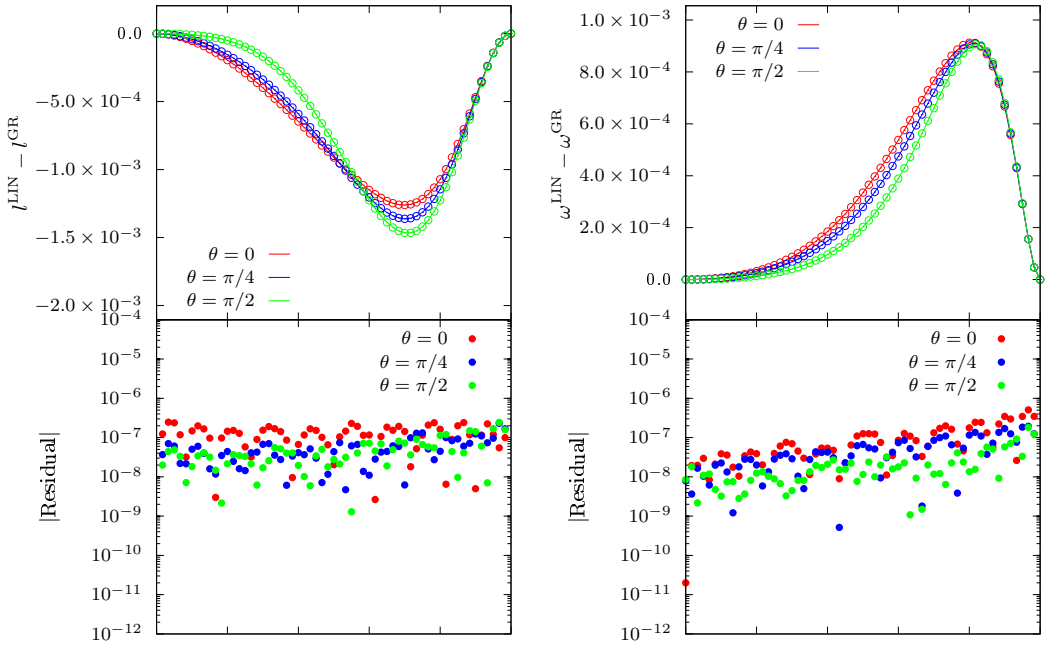

(c) l metric element residual

(d) ω metric element residual

Figure 4.11: Difference between metric elements using the linear coupling function and the analytical fit and the Kerr metric for three selected angles for a solution of $\bar{\alpha} = 0.5$ and $\chi = 0.6$ (top) and the absolute residual between the analytical fit and the numerical data (bottom). Here we show the metric components f (top left), m (top right), l (bottom left) and ω (bottom right) for three angles $\theta = 0, \pi/4, \pi/2$ denoted by the red, blue, and green colors respectively. The analytic fit is denoted by the solid line, while the dots are the numerical solution.

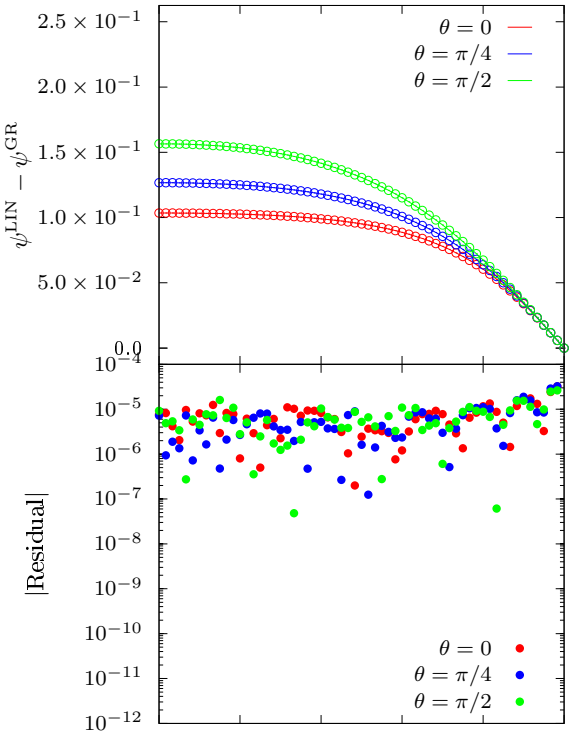

Figure 4.12: The scalar field using the linear coupling function and its analytical fit for $\bar{\alpha} = 0.5$ and $\chi = 0.6$ and the absolute residual between the analytical fit and the numerical data (bottom). The analytic fit for three angles $\theta = 0, \pi/4, \pi/2$ are denoted by the red, blue, and green solid lines respectively while the dots denote the numerical solution.

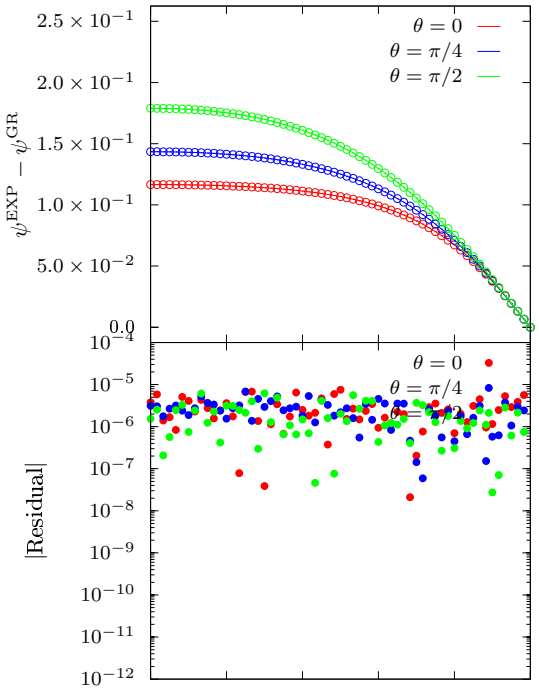

Figure 4.13: The scalar field using the exponential coupling function and its analytical fit for $\bar{\alpha} = 0.5$ and $\chi = 0.6$ and the absolute residual between the analytical fit and the numerical data (bottom). The analytic fit for three angles $\theta = 0, \pi/4, \pi/2$ are denoted by the red, blue, and green solid lines respectively while the dots denote the numerical solution.

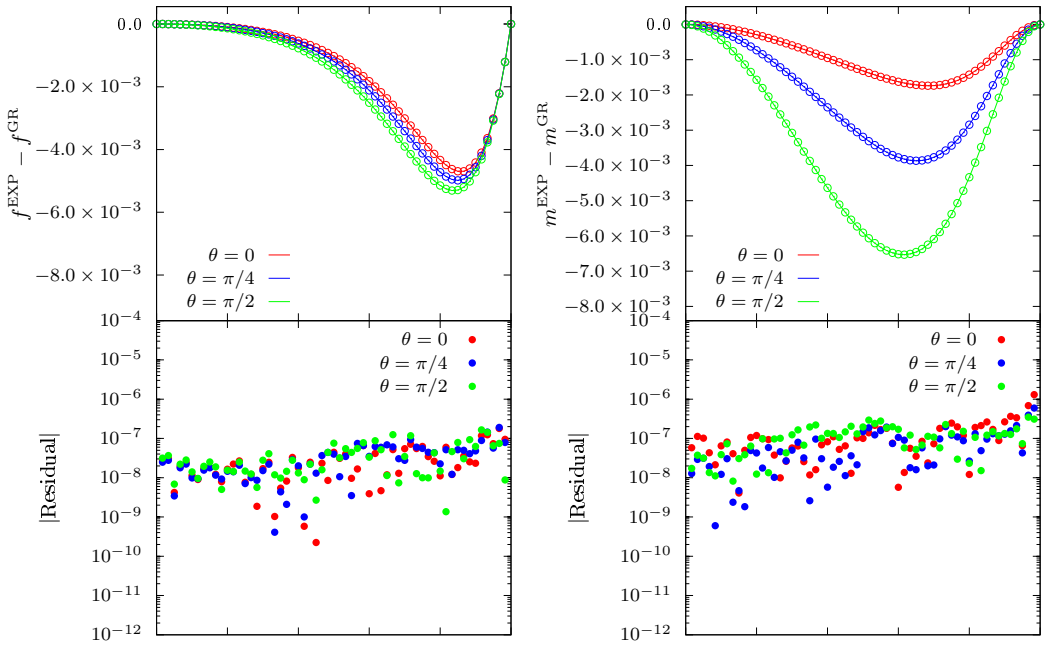

(a) f metric element residual

(b) m metric element residual

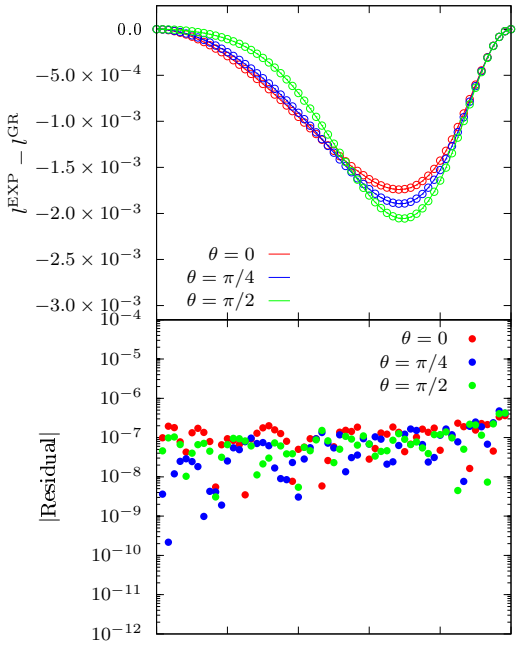

(c) l metric element residual

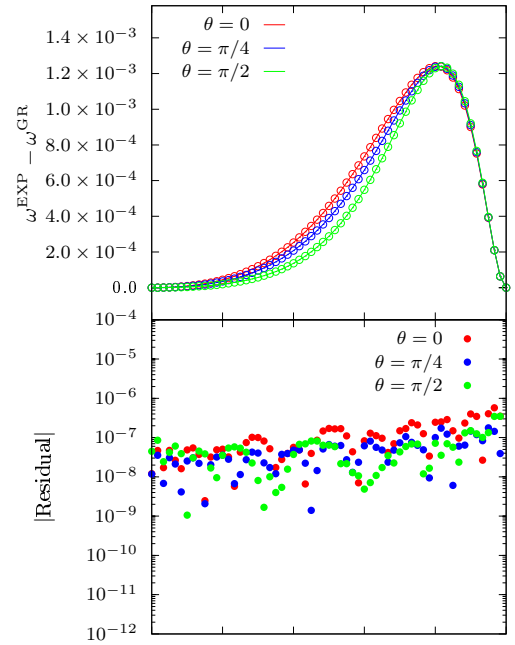

(d) ω metric element residual

Figure 4.14: Difference between metric elements using the exponential coupling function and the analytical fit and the Kerr metric for three selected angles for a solution of $\bar{\alpha} = 0.5$ and $\chi = 0.6$ and the absolute residual between the analytical fit and the numerical data (bottom). Here we show the metric components f (top left), m (top right), l (bottom left) and ω (bottom right) for three angles $\theta = 0, \pi/4, \pi/2$ denoted by the red, blue, and green colors respectively. The analytic fit is denoted by the solid line, while the dots are the numerical solution.

Marginal Stable Circular Orbits

To numerically calculate the location of the marginal stable circular orbits (MSCO) around a stationary, axially symmetric black hole we begin with a generic metric ansatz of the form

$$ds^2 = g_{tt}dt^2 + g_{rr}dr^2 + g_{\theta\theta}d\theta^2 + g_{\phi\phi}d\phi^2 + 2g_{t\phi}dtd\phi. \tag{4.52}$$

The two killing vectors of our spacetime t^μ and ϕ^μ correspond to the reduced energy E and angular momentum L of the particle,

$$\begin{aligned} E &= -t_\mu \frac{dx^\mu}{d\lambda} = -g_{tt}\dot{t} - g_{t\phi}\dot{\phi}, \\ L &= \phi_\mu \frac{dx^\mu}{d\lambda} = g_{t\phi}\dot{t} + g_{\phi\phi}\dot{\phi}, \end{aligned} \tag{4.53}$$

which can be combined to obtain expressions for $\dot{t}$ and $\dot{\phi}$,

$$\begin{aligned} \dot{t} &= \frac{Eg_{tt} + Lg_{t\phi}}{{g_{t\phi}}^2 - g_{tt}g_{\phi\phi}}, \\ \dot{\phi} &= -\frac{Eg_{t\phi} + Lg_{tt}}{{g_{t\phi}}^2 - g_{tt}g_{\phi\phi}}. \end{aligned} \tag{4.54}$$

If we consider orbits constrained to the equatorial plane $\theta = \pi/2$, the four-velocity normalization condition becomes

$$-\epsilon = g_{tt}\dot{t}^2 + g_{rr}\dot{r}^2 + g_{\phi\phi}\dot{\phi}^2 + 2g_{t\phi}\dot{t}\dot{\phi}, \tag{4.55}$$

where $\epsilon = 0$ for photon and $\epsilon = 1$ for massive particles. Inserting $\dot{t}$ and $\dot{\phi}$, we can solve for $\dot{r}^2$ and define an effective potential U_{eff} given by

$$\dot{r}^2 = \frac{1}{g_{rr}}\left(-\epsilon + \frac{E^2 g_{\phi\phi} + 2ELg_{t\phi} + L^2 g_{tt}}{{g_{t\phi}}^2 - g_{tt}g_{\phi\phi}}\right) \equiv U_{\text{eff}}. \tag{4.56}$$

The condition for a circular orbit is $\dot{r} = \ddot{r} = 0$ by differentiating

$$\frac{d}{d\lambda}\dot{r}^2 = 2\dot{r}\ddot{r} = \frac{dU_{\text{eff}}}{dr}\dot{r} \rightarrow \ddot{r} = \frac{dU_{\text{eff}}}{dr} = 0, \tag{4.57}$$

we find that these two conditions imply that the effective potential and its derivative must vanish. These two conditions can be rearranged to two differential equations that must be simultaneously satisfied:

$$E^2 g_{\phi\phi} + 2ELg_{t\phi} + L^2 g_{tt} - \epsilon\left({g_{t\phi}}^2 - g_{tt}g_{\phi\phi}\right) = 0, \tag{4.58}$$

$$E^2 {g_{\phi\phi}}' + 2ELg_{t\phi}' + L^2 {g_{tt}}' - \epsilon\left({g_{t\phi}}^2 - g_{tt}g_{\phi\phi}\right)' = 0, \tag{4.59}$$

where the primes denote radial derivatives e.g. ${g_{tt}}' = \frac{dg_{tt}}{dr}$. We now turn to specific cases of these marginal stable circular orbits: the light ring, and the innermost stable circular orbit.

Light Ring

For a photon, $\epsilon = 0$ and Eq. (4.58) can be solved quadratically for E or L

$$L = E\left(\frac{g_{t\phi} \pm \sqrt{{g_{t\phi}}^2 - g_{tt}g_{\phi\phi}}}{g_{tt}}\right), \tag{4.60}$$

and this result can be inserted into Eq. (4.59) to obtain a first order differential equation given by

$$\begin{aligned} {g_{\phi\phi}}' + 2{g_{t\phi}}'&\left(\frac{g_{t\phi} \pm \sqrt{{g_{t\phi}}^2 - g_{tt}g_{\phi\phi}}}{g_{tt}}\right) \\ &+ {g_{tt}}'\left(\frac{g_{t\phi} \pm \sqrt{{g_{t\phi}}^2 - g_{tt}g_{\phi\phi}}}{g_{tt}}\right)^2 = 0, \end{aligned} \tag{4.61}$$

whose smallest root is the location of the light ring. Once we insert the metric functions known analytically or numerically, we only need to determine the root of the above equation to find the location of the light ring. The novelty of this approach is that we have not specified a modified theory of gravity and have derived this equation simply from the symmetries of our spacetime. With our nonlinear numerical solutions, we can approximate the derivatives using our Newton interpolation polynomial and use a Newton-Raphson algorithm to find the root. The results were presented in Fig. 4.3.

Innermost Stable Circular Orbit

For a massive particle, $\epsilon = 1$ and the innermost stable circular orbit is located at the saddle point of the effective potential, specifically when $U''_{\text{eff}} = 0$. This adds another condition that must be satisfied and another differential equation analogous to Eq. (4.59) given by

$$E^2 {g_{\phi\phi}}'' + 2EL{g_{t\phi}}'' + L^2 {g_{tt}}'' - \epsilon \left({g_{t\phi}}^2 - g_{tt}g_{\phi\phi}\right)'' = 0. \tag{4.62}$$

To find the ISCO, we begin by solving Eq. (4.58) quadratically for L similar to the approach taken for the light ring

$$L = \frac{Eg_{t\phi} \pm \sqrt{\left(E^2 + \epsilon g_{tt}\right)\left({g_{t\phi}}^2 - g_{tt}g_{\phi\phi}\right)}}{g_{tt}}. \tag{4.63}$$

We insert this expression into Eq. (4.59) and solve for E as a function of only the metric and its first derivatives

$$E = E\left[g_{\mu\nu}, {g_{\mu\nu}}'\right], \tag{4.64}$$

which can also be substituted back into Eq. (4.63) to obtain L also as a function of only the metric and its first derivatives

$$L = L\left[g_{\mu\nu}, g_{\mu\nu}{}'\right]. \tag{4.65}$$

These expressions are calculated in the symbolic manipulation software *Maple 2018* available at `https://github.com/sullivanandrew/XPDES` and will not be presented here. Finally, we can substitute both of these into Eq. (4.62) to obtain a second order differential equation, the smallest root of which is the ISCO. As in the case with the light ring, this is done numerically with a Newton-Raphson algorithm and the result is shown on the left plot of Fig. 4.3.

Conclusions

We have presented here a numerical infrastructure to calculate the exterior spacetimes of rotating black holes in a wide class of modified theories of gravity. We have validated this infrastructure in GR and by direct comparison with a rotating, weak-coupling perturbative numerical solution. We then compared the full nonlinear solutions to rotating black holes to find the deviations from GR in the metric functions and the physical observables such as the mass and angular momentum. We then used the numerical solutions to construct analytical fitted models that reproduce the data to within the accuracy of the solutions and calculated other physical observables like location of the the ISCO and light ring. We find that the solutions in linear sGB are very closely approximated by the perturbative weak-coupling expansion and that these solutions differ quite drastically from the EdGB solutions found using an exponential coupling. We also find that the deviations of rotating black holes from GR become increasingly suppressed for black hole larger spins as the deviations sourced

by the scalar charge begin to become dominated by the gravitational effects of the angular momentum.

The analytical fitted models constructed from these solutions can be used to calculate other astrophysical observables such as accretion disks around black holes [8] or black hole shadows [16]. These solutions can also be used as a background to study polar and axial perturbations to predict the quasinormal mode spectrum of scalar Gauss-Bonnet black holes [25, 31, 67, 105]. These can then be compared to gravitational wave ringdown observations of merging black holes of future detectors to place constraints on a variety of modified gravity theories.

Acknowledgments

We are grateful for the computational support of the Hyalite High-Performance Computing System, operated and supported by University Information Technology Research Cyberinfrastructure at Montana State University. A. S. and N. Y. would like to acknowledge support from NSF PHY-1759615 and NASA grant 80NSSC18K1352. T. P. S. acknowledges partial support from the STFC Consolidated Grant No. ST/P000703/1 and networking support from the COST Action GWverse CA16104.

CONCLUSION

In summary, we have used two different numerical approaches to solve for rotating compact objects in two modified theories of gravity. First we used a fourth-order Runge-Kutta-Fehlberg method to numerically integrate the modified equations of stellar structure for neutron stars in massive bigravity with realistic equations of state to first order in slow rotation. This required a multi-dimensional shooting method to determine integration constants at the stellar core and spatial infinity. We then calculated physical observables from the solutions such as the mass, radius, and moment of inertia. We found that the mass of the star is not constant outside the stellar surface in this theory and that the modifications in the mass-radius and moment of inertia-mass relations are degenerate with the equation of state. These results could be used to place constraints on the coupling parameters of the theory with a future analysis of the post-Keplerian parameters of binary pulsar systems.

The second numerical approach applied a finite difference method to a discretized grid for stationary spherically symmetric and axially symmetric black hole spaces times in scalar Gauss-Bonnet gravity. The method uses a minimal amount of assumptions of the modified theory of gravity to produce a theory independent numerical infrastructure to calculate physical observables of rotating black holes in a wide class of modified theories of gravity. We discretized the modified field equations on a 2-dimensional grid and used a relaxed Newton-Raphson method to minimize the residual of the solution. We utilized an adaptive mesh refinement to control the discretization errors throughout this process. From the solutions, we were able to calculate physical observables in various formulations of this theory that make various approximations and tested how accurate each approximation compares. From the numerical solutions, we constructed a fitted analytical model, accurate to

the numerical tolerance of each solution, that we then used to rapidly calculate the same physical observables we obtained from the full numerical solution. These fitted analytical models can be used in future studies as backgrounds to study black hole perturbations and calculate the quasinormal ringdown modes of binary black hole mergers in these theories.

REFERENCES CITED

[1] B. P. Abbott et al. Gw151226: Observation of gravitational waves from a 22-solar-mass binary black hole coalescence. *Phys. Rev. Lett.*, 116:241103, Jun 2016.

[2] B. P. Abbott et al. Observation of gravitational waves from a binary black hole merger. *Phys. Rev. Lett.*, 116:061102, Feb 2016.

[3] B. P. Abbott et al. Gw170104: Observation of a 50-solar-mass binary black hole coalescence at redshift 0.2. *Phys. Rev. Lett.*, 118:221101, Jun 2017.

[4] B. P. Abbott et al. Gw170608: Observation of a 19 solar-mass binary black hole coalescence. *The Astrophysical Journal Letters*, 851(2):L35, 2017.

[5] B. P. Abbott et al. Gw170814: A three-detector observation of gravitational waves from a binary black hole coalescence. *Phys. Rev. Lett.*, 119:141101, Oct 2017.

[6] B. P. Abbott et al. Gw170817: Observation of gravitational waves from a binary neutron star inspiral. *Phys. Rev. Lett.*, 119:161101, Oct 2017.

[7] B. P. *et al.* Abbott. Tests of general relativity with GW150914. *Phys. Rev. Lett.*, 116(22):221101, 2016.

[8] Marek A. Abramowicz and P. Chris Fragile. Foundations of black hole accretion disk theory. *Living Reviews in Relativity*, 16(1):1, Jan 2013.

[9] A. Akmal, V. R. Pandharipande, and D. G. Ravenhall. The Equation of state of nucleon matter and neutron star structure. *Phys. Rev.*, C58:1804–1828, 1998.

[10] S. O. Alexeyev and M. V. Pomazanov. Black hole solutions with dilatonic hair in higher curvature gravity. *Phys. Rev. D*, 55:2110–2118, Feb 1997.

[11] John Antoniadis, Paulo C. C. Freire, Norbert Wex, Thomas M. Tauris, Ryan S. Lynch, Marten H. van Kerkwijk, Michael Kramer, Cees Bassa, Vik S. Dhillon, Thomas Driebe, Jason W. T. Hessels, Victoria M. Kaspi, Vladislav I. Kondratiev, Norbert Langer, Thomas R. Marsh, Maura A. McLaughlin, Timothy T. Pennucci, Scott M. Ransom, Ingrid H. Stairs, Joeri van Leeuwen, Joris P. W. Verbiest, and David G. Whelan. A massive pulsar in a compact relativistic binary. *Science*, 340(6131), 2013.

[12] Katsuki Aoki, Kei-ichi Maeda, and Makoto Tanabe. Relativistic stars in bigravity theory. *Phys. Rev.*, D93(6):064054, 2016.

[13] Zaven Arzoumanian, Adam Brazier, Sarah Burke-Spolaor, Sydney Chamberlin, Shami Chatterjee, Brian Christy, James M. Cordes, Neil J. Cornish, Fronefield Crawford, H. Thankful Cromartie, Kathryn Crowter, Megan E. DeCesar,

Paul B. Demorest, Timothy Dolch, Justin A. Ellis, Robert D. Ferdman, Elizabeth C. Ferrara, Emmanuel Fonseca, Nathan Garver-Daniels, Peter A. Gentile, Daniel Halmrast, E. A. Huerta, Fredrick A. Jenet, Cody Jessup, Glenn Jones, Megan L. Jones, David L. Kaplan, Michael T. Lam, T. Joseph W. Lazio, Lina Levin, Andrea Lommen, Duncan R. Lorimer, Jing Luo, Ryan S. Lynch, Dustin Madison, Allison M. Matthews, Maura A. McLaughlin, Sean T. McWilliams, Chiara Mingarelli, Cherry Ng, David J. Nice, Timothy T. Pennucci, Scott M. Ransom, Paul S. Ray, Xavier Siemens, Joseph Simon, Renée Spiewak, Ingrid H. Stairs, Daniel R. Stinebring, Kevin Stovall, Joseph K. Swiggum, Stephen R. Taylor, Michele Vallisneri, Rutger van Haasteren, Sarah J. Vigeland, and Weiwei Zhu and. The NANOGrav 11-year data set: High-precision timing of 45 millisecond pulsars. *The Astrophysical Journal Supplement Series*, 235(2):37, apr 2018.

[14] Eloy Ayón-Beato, Daniel Higuita-Borja, and Julio A. Móndez-Zavaleta. Rotating (A)dS black holes in bigravity. *Phys. Rev.*, D93(2):024049, 2016.

[15] Dimitry Ayzenberg and Nicolás Yunes. Slowly rotating black holes in einstein-dilaton-gauss-bonnet gravity: Quadratic order in spin solutions. *Phys. Rev. D*, 90:044066, Aug 2014.

[16] Dimitry Ayzenberg and NicolÃ¡s Yunes. Black hole shadow as a test of general relativity: quadratic gravity. *Classical and Quantum Gravity*, 35(23):235002, 2018.

[17] Eugeny Babichev and Alessandro Fabbri. Instability of black holes in massive gravity. *Class. Quant. Grav.*, 30:152001, 2013.

[18] Eugeny Babichev and Alessandro Fabbri. Rotating black holes in massive gravity. *Phys. Rev.*, D90:084019, 2014.

[19] Eugeny Babichev and Alessandro Fabbri. Stability analysis of black holes in massive gravity: a unified treatment. *Phys. Rev.*, D89(8):081502, 2014.

[20] Leor Barack, Vitor Cardoso, Samaya Nissanke, Thomas P Sotiriou, Abbas Askar, Chris Belczynski, Gianfranco Bertone, Edi Bon, Diego Blas, Richard Brito, Tomasz Bulik, Clare Burrage, Christian T Byrnes, Chiara Caprini, Masha Chernyakova, Piotr Chruściel, Monica Colpi, Valeria Ferrari, Daniele Gaggero, Jonathan Gair, Juan García-Bellido, S F Hassan, Lavinia Heisenberg, Martin Hendry, Ik Siong Heng, Carlos Herdeiro, Tanja Hinderer, Assaf Horesh, Bradley J Kavanagh, Bence Kocsis, Michael Kramer, Alexandre Le Tiec, Chiara Mingarelli, Germano Nardini, Gijs Nelemans, Carlos Palenzuela, Paolo Pani, Albino Perego, Edward K Porter, Elena M Rossi, Patricia Schmidt, Alberto Sesana, Ulrich Sperhake, Antonio Stamerra, Leo C Stein, Nicola Tamanini, Thomas M Tauris, L Arturo Urena-López, Frederic Vincent, Marta Volonteri,

Barry Wardell, Norbert Wex, Kent Yagi, Tiziano Abdelsalhin, Miguel Ángel Aloy, Pau Amaro-Seoane, Lorenzo Annulli, Manuel Arca-Sedda, Ibrahima Bah, Enrico Barausse, Elvis Barakovic, Robert Benkel, Charles L Bennett, Laura Bernard, Sebastiano Bernuzzi, Christopher P L Berry, Emanuele Berti, Miguel Bezares, Jose Juan Blanco-Pillado, Jose Luis Blázquez-Salcedo, Matteo Bonetti, Mateja Bošković, Zeljka Bosnjak, Katja Bricman, Bernd BrÃ$\frac{1}{4}$gmann, Pedro R Capelo, Sante Carloni, Pablo Cerdá-Durán, Christos Charmousis, Sylvain Chaty, Aurora Clerici, Andrew Coates, Marta Colleoni, Lucas G Collodel, Geoffrey Compère, William Cook, Isabel Cordero-Carrión, Miguel Correia, Álvaro de la Cruz-Dombriz, Viktor G Czinner, Kyriakos Destounis, Kostas Dialektopoulos, Daniela Doneva, Massimo Dotti, Amelia Drew, Christopher Eckner, James Edholm, Roberto Emparan, Recai Erdem, Miguel Ferreira, Pedro G Ferreira, Andrew Finch, Jose A Font, Nicola Franchini, Kwinten Fransen, Dmitry Gal'tsov, Apratim Ganguly, Davide Gerosa, Kostas Glampedakis, Andreja Gomboc, Ariel Goobar, Leonardo Gualtieri, Eduardo Guendelman, Francesco Haardt, Troels Harmark, Filip Hejda, Thomas Hertog, Seth Hopper, Sascha Husa, Nada Ihanec, Taishi Ikeda, Amruta Jaodand, Philippe Jetzer, Xisco Jimenez-Forteza, Marc Kamionkowski, David E Kaplan, Stelios Kazantzidis, Masashi Kimura, Shiho Kobayashi, Kostas Kokkotas, Julian Krolik, Jutta Kunz, Claus Lämmerzahl, Paul Lasky, José P S Lemos, Jackson Levi Said, Stefano Liberati, Jorge Lopes, Raimon Luna, Yin-Zhe Ma, Elisa Maggio, Alberto Mangiagli, Marina Martinez Montero, Andrea Maselli, Lucio Mayer, Anupam Mazumdar, Christopher Messenger, Brice Ménard, Masato Minamitsuji, Christopher J Moore, David Mota, Sourabh Nampalliwar, Andrea Nerozzi, David Nichols, Emil Nissimov, Martin Obergaulinger, Niels A Obers, Roberto Oliveri, George Pappas, Vedad Pasic, Hiranya Peiris, Tanja Petrushevska, Denis Pollney, Geraint Pratten, Nemanja Rakic, Istvan Racz, Miren Radia, Fethi M Ramazanoğlu, Antoni Ramos-Buades, Guilherme Raposo, Marek Rogatko, Roxana Rosca-Mead, Dorota Rosinska, Stephan Rosswog, Ester Ruiz-Morales, Mairi Sakellariadou, Nicolás Sanchis-Gual, Om Sharan Salafia, Anuradha Samajdar, Alicia Sintes, Majda Smole, Carlos Sopuerta, Rafael Souza-Lima, Marko Stalevski, Nikolaos Stergioulas, Chris Stevens, Tomas Tamfal, Alejandro Torres-Forné, Sergey Tsygankov, Kıvanç İ Ünlütürk, Rosa Valiante, Maarten van de Meent, José Velhinho, Yosef Verbin, Bert Vercnocke, Daniele Vernieri, Rodrigo Vicente, Vincenzo Vitagliano, Amanda Weltman, Bernard Whiting, Andrew Williamson, Helvi Witek, Aneta Wojnar, Kadri Yakut, Haopeng Yan, Stoycho Yazadjiev, Gabrijela Zaharijas, and Miguel Zilhão. Black holes, gravitational waves and fundamental physics: a roadmap. *Classical and Quantum Gravity*, 36(14):143001, jun 2019.

[21] Enrico Barausse, Ted Jacobson, and Thomas P. Sotiriou. Black holes in einstein-aether and hořava-lifshitz gravity. *Phys. Rev. D*, 83:124043, Jun 2011.

[22] Robert Benkel, Thomas P. Sotiriou, and Helvi Witek. Dynamical scalar hair formation around a schwarzschild black hole. *Phys. Rev. D*, 94:121503, Dec 2016.

[23] Robert Benkel, Thomas P. Sotiriou, and Helvi Witek. Black hole hair formation in shift-symmetric generalised scalar-tensor gravity. *Class. Quant. Grav.*, 34(6):064001, 2017.

[24] Emanuele Berti, Enrico Barausse, Vitor Cardoso, Leonardo Gualtieri, Paolo Pani, Ulrich Sperhake, Leo C Stein, Norbert Wex, Kent Yagi, Tessa Baker, C P Burgess, FlÃ¡vio S Coelho, Daniela Doneva, Antonio De Felice, Pedro G Ferreira, Paulo C C Freire, James Healy, Carlos Herdeiro, Michael Horbatsch, Burkhard Kleihaus, Antoine Klein, Kostas Kokkotas, Jutta Kunz, Pablo Laguna, Ryan N Lang, Tjonnie G F Li, Tyson Littenberg, Andrew Matas, Saeed Mirshekari, Hirotada Okawa, Eugen Radu, Richard O'Shaughnessy, Bangalore S Sathyaprakash, Chris Van Den Broeck, Hans A Winther, Helvi Witek, Mir Emad Aghili, Justin Alsing, Brett Bolen, Luca Bombelli, Sarah Caudill, Liang Chen, Juan Carlos Degollado, Ryuichi Fujita, Caixia Gao, Davide Gerosa, Saeed Kamali, Hector O Silva, JoÃ£o G Rosa, Laleh Sadeghian, Marco Sampaio, Hajime Sotani, and Miguel Zilhao. Testing general relativity with present and future astrophysical observations. *Classical and Quantum Gravity*, 32(24):243001, 2015.

[25] Jose Luis Blázquez-Salcedo, Caio F. B. Macedo, Vitor Cardoso, Valeria Ferrari, Leonardo Gualtieri, Fech Scen Khoo, Jutta Kunz, and Paolo Pani. Perturbed black holes in Einstein-dilaton-Gauss-Bonnet gravity: Stability, ringdown, and gravitational-wave emission. *Phys. Rev.*, D94(10):104024, 2016.

[26] Richard Brito, Vitor Cardoso, and Paolo Pani. Black holes with massive graviton hair. *Phys. Rev.*, D88:064006, 2013.

[27] Richard Brito, Vitor Cardoso, and Paolo Pani. Massive spin-2 fields on black hole spacetimes: Instability of the Schwarzschild and Kerr solutions and bounds on the graviton mass. *Phys. Rev.*, D88(2):023514, 2013.

[28] Cliff P. Burgess. Quantum gravity in everyday life: General relativity as an effective field theory. *Living Reviews in Relativity*, 7(1):5, Apr 2004.

[29] C.P. Burgess. An introduction to effective field theory. *Annual Review of Nuclear and Particle Science*, 57(1):329–362, 2007.

[30] Bruce A. Campbell, Nemanja Kaloper, and Keith A. Olive. Classical hair for kerr-newman black holes in string gravity. *Physics Letters B*, 285(3):199 – 205, 1992.

[31] Vitor Cardoso, Masashi Kimura, Andrea Maselli, Emanuele Berti, Caio F. B. Macedo, and Ryan McManus. Parametrized black hole quasinormal ringdown: Decoupled equations for nonrotating black holes. *Phys. Rev. D*, 99:104077, May 2019.

[32] Sean M. Carroll. The cosmological constant. *Living Reviews in Relativity*, 4(1):1, 2001.

[33] Clifford Cheung and Grant N. Remmen. Positive Signs in Massive Gravity. *JHEP*, 04:002, 2016.

[34] D. Comelli, M. Crisostomi, F. Nesti, and L. Pilo. Spherically Symmetric Solutions in Ghost-Free Massive Gravity. *Phys. Rev.*, D85:024044, 2012.

[35] Alan Cooney, Simon DeDeo, and Dimitrios Psaltis. Gravity with perturbative constraints: Dark energy without new degrees of freedom. *Phys. Rev. D*, 79:044033, Feb 2009.

[36] G. D'Amico, C. de Rham, S. Dubovsky, G. Gabadadze, D. Pirtskhalava, and A. J. Tolley. Massive Cosmologies. *Phys. Rev.*, D84:124046, 2011.

[37] Thibault Damour. Binary Systems as Test-beds of Gravity Theories. 2007.

[38] Thibault Damour. *Binary Systems as Test-Beds of Gravity Theories*, pages 1–41. Springer Netherlands, Dordrecht, 2009.

[39] Thibault Damour and Gilles Esposito-Farèse. Gravitational-wave versus binary-pulsar tests of strong-field gravity. *Phys. Rev. D*, 58:042001, Jul 1998.

[40] Antonio De Felice, Takashi Nakamura, and Takahiro Tanaka. Possible existence of viable models of bi-gravity with detectable graviton oscillations by gravitational wave detectors. *PTEP*, 2014:043E01, 2014.

[41] Claudia de Rham. Massive Gravity. *Living Rev. Rel.*, 17:7, 2014.

[42] Claudia de Rham, J. Tate Deskins, Andrew J. Tolley, and Shuang-Yong Zhou. Graviton Mass Bounds. *Rev. Mod. Phys.*, 89(2):025004, 2017.

[43] Claudia de Rham, Gregory Gabadadze, and Andrew J. Tolley. Resummation of Massive Gravity. *Phys. Rev. Lett.*, 106:231101, 2011.

[44] Sheperd Doeleman, Eric Agol, Don Backer, Fred Baganoff, Geoffrey C. Bower, Avery Broderick, Andrew Fabian, Vincent Fish, Charles Gammie, Paul Ho, Mareki Honman, Thomas Krichbaum, Avi Loeb, Dan Marrone, Mark Reid, Alan Rogers, Irwin Shapiro, Peter Strittmatter, Remo Tilanus, Jonathan Weintroub, Alan Whitney, Melvyn Wright, and Lucy Ziurys. Imaging an Event Horizon: submm-VLBI of a Super Massive Black Hole. In *astro2010: The*

Astronomy and Astrophysics Decadal Survey, volume 2010, page 68, January 2009.

[45] Daniela D. Doneva and Stoytcho S. Yazadjiev. New gauss-bonnet black holes with curvature-induced scalarization in extended scalar-tensor theories. *Phys. Rev. Lett.*, 120:131103, Mar 2018.

[46] Jonas Enander and Edvard Mörtsell. On stars, galaxies and black holes in massive bigravity. *Journal of Cosmology and Astroparticle Physics*, 2015(11):023, 2015.

[47] E. Fehlberg. Klassische runge-kutta-formeln vierter und niedrigerer ordnung mit schrittweiten-kontrolle und ihre anwendung auf wärmeleitungsprobleme. *Computing*, 6(1):61–71, 1970.

[48] Jonathan R. Gair, Michele Vallisneri, Shane L. Larson, and John G. Baker. Testing general relativity with low-frequency, space-based gravitational-wave detectors. *Living Reviews in Relativity*, 16(1):7, 2013.

[49] Jeremy Gray. Epistemology of geometry. In Edward N. Zalta, editor, *The Stanford Encyclopedia of Philosophy*. Metaphysics Research Lab, Stanford University, fall 2019 edition, 2019.

[50] David J. Gross and John H. Sloan. The quartic effective action for the heterotic string. *Nuclear Physics B*, 291:41 – 89, 1987.

[51] Sebastien Guillot, Mathieu Servillat, Natalie A. Webb, and Robert E. Rutledge. Measurement of the Radius of Neutron Stars with High S/N Quiescent Low-mass X-ray Binaries in Globular Clusters. *Astrophys. J.*, 772:7, 2013.

[52] Zong-Kuan Guo, Nobuyoshi Ohta, and Takashi Torii. Black holes in the dilatonic einstein-gauss-bonnet theory in various dimensions. i asymptotically flat black holes . *Progress of Theoretical Physics*, 120(3):581–607, 2008.

[53] Toral Gupta, Barun Majumder, Kent Yagi, and NicolÃ¡s Yunes. I-Love-Q Relations for Neutron Stars in dynamical Chern Simons Gravity. 2017.

[54] J. B. Hartle. Slowly Rotating Relativistic Stars. I. Equations of Structure. *Astrophys. J.*, 150:1005, December 1967.

[55] James B. Hartle and Kip S. Thorne. Slowly Rotating Relativistic Stars. II. Models for Neutron Stars and Supermassive Stars. *Astrophys. J.*, 153:807, 1968.

[56] S. F. Hassan and Rachel A. Rosen. On Non-Linear Actions for Massive Gravity. *JHEP*, 07:009, 2011.

[57] S. F. Hassan and Rachel A. Rosen. Bimetric Gravity from Ghost-free Massive Gravity. *JHEP*, 02:126, 2012.

[58] P. Kanti, N. E. Mavromatos, J. Rizos, K. Tamvakis, and E. Winstanley. Dilatonic black holes in higher curvature string gravity. *Phys. Rev. D*, 54:5049–5058, Oct 1996.

[59] Burkhard Kleihaus and Jutta Kunz. Static axially symmetric einstein-yang-mills-dilaton solutions. ii. black hole solutions. *Phys. Rev. D*, 57:6138–6157, May 1998.

[60] Burkhard Kleihaus, Jutta Kunz, Sindy Mojica, and Eugen Radu. Spinning black holes in einstein–gauss-bonnet–dilaton theory: Nonperturbative solutions. *Phys. Rev. D*, 93:044047, Feb 2016.

[61] Kostas D. Kokkotas and Bernd G. Schmidt. Quasi-normal modes of stars and black holes. *Living Reviews in Relativity*, 2(1):2, 1999.

[62] James M. Lattimer and Bernard F. Schutz. Constraining the equation of state with moment of inertia measurements. *The Astrophysical Journal*, 629(2):979, 2005.

[63] James M. Lattimer and F. Douglas Swesty. A generalized equation of state for hot, dense matter. *Nuclear Physics A*, 535(2):331 – 376, 1991.

[64] Duncan R. Lorimer. Binary and millisecond pulsars. *Living Reviews in Relativity*, 11(1):8, Nov 2008.

[65] A. G. Lyne, M. Burgay, M. Kramer, A. Possenti, R.N. Manchester, F. Camilo, M. A. McLaughlin, D. R. Lorimer, N. D'Amico, B. C. Joshi, J. Reynolds, and P. C. C. Freire. A double-pulsar system: A rare laboratory for relativistic gravity and plasma physics. *Science*, 303(5661):1153–1157, 2004.

[66] Andrea Maselli, Paolo Pani, Leonardo Gualtieri, and Valeria Ferrari. Rotating black holes in einstein-dilaton-gauss-bonnet gravity with finite coupling. *Phys. Rev. D*, 92:083014, Oct 2015.

[67] Ryan McManus, Emanuele Berti, Caio F. B. Macedo, Masashi Kimura, Andrea Maselli, and Vitor Cardoso. Parametrized black hole quasinormal ringdown. ii. coupled equations and quadratic corrections for nonrotating black holes. *Phys. Rev. D*, 100:044061, Aug 2019.

[68] S. Mignemi and N. R. Stewart. Charged black holes in effective string theory. *Phys. Rev. D*, 47:5259–5269, Jun 1993.

[69] S. Mignemi and N.R. Stewart. Dilaton-axion hair for slowly rotating kerr black holes. *Physics Letters B*, 298(3):299 – 304, 1993.

[70] M. C. Miller, F. K. Lamb, A. J. Dittmann, S. Bogdanov, Z. Arzoumanian, K. C. Gendreau, S. Guillot, A. K. Harding, W. C. G. Ho, J. M. Lattimer, R. M. Ludlam, S. Mahmoodifar, S. M. Morsink, P. S. Ray, T. E. Strohmayer, K. S. Wood, T. Enoto, R. Foster, T. Okajima, G. Prigozhin, and Y. Soong. PSR j0030+0451 mass and radius from NICER data and implications for the properties of neutron star matter. *The Astrophysical Journal*, 887(1):L24, dec 2019.

[71] Paolo Pani and Vitor Cardoso. Are black holes in alternative theories serious astrophysical candidates? the case for einstein-dilaton-gauss-bonnet black holes. *Phys. Rev. D*, 79:084031, Apr 2009.

[72] Paolo Pani, Caio F. B. Macedo, Luís C. B. Crispino, and Vitor Cardoso. Slowly rotating black holes in alternative theories of gravity. *Phys. Rev. D*, 84:087501, Oct 2011.

[73] W. Pauli and M. Fierz. On Relativistic Field Equations of Particles With Arbitrary Spin in an Electromagnetic Field. *Helv. Phys. Acta*, 12:297–300, 1939.

[74] William H. Press, Saul A. Teukolsky, William T. Vetterling, and Brian P. Flannery. *Numerical Recipes in C (2Nd Ed.): The Art of Scientific Computing*. Cambridge University Press, New York, NY, USA, 1992.

[75] Dimitrios Psaltis. Probes and tests of strong-field gravity with observations in the electromagnetic spectrum. *Living Reviews in Relativity*, 11(1):9, 2008.

[76] Tullio Regge and John A. Wheeler. Stability of a schwarzschild singularity. *Phys. Rev.*, 108:1063–1069, Nov 1957.

[77] Luciano Rezzolla and Alexander Zhidenko. New parametrization for spherically symmetric black holes in metric theories of gravity. *Phys. Rev. D*, 90:084009, Oct 2014.

[78] Justin L. Ripley and Frans Pretorius. Hyperbolicity in spherical gravitational collapse in a horndeski theory. *Phys. Rev. D*, 99:084014, Apr 2019.

[79] Matteo Luca Ruggiero and Angelo Tartaglia. A Post-Keplerian parameter to test gravito-magnetic effects in binary pulsar systems. *Phys. Rev.*, D72:084030, 2005.

[80] Y. Saad and M. Schultz. Gmres: A generalized minimal residual algorithm for solving nonsymmetric linear systems. *SIAM Journal on Scientific and Statistical Computing*, 7(3):856–869, 1986.

[81] Laura Sampson, Nicolás Yunes, Neil Cornish, Marcelo Ponce, Enrico Barausse, Antoine Klein, Carlos Palenzuela, and Luis Lehner. Projected constraints on scalarization with gravitational waves from neutron star binaries. *Phys. Rev. D*, 90:124091, Dec 2014.

[82] Angnis Schmidt-May and Mikael von Strauss. Recent developments in bimetric theory. *Journal of Physics A: Mathematical and Theoretical*, 49(18):183001, 2016.

[83] W. Schönauer and R. Weiß. Efficient vectorizable pde solvers. *Journal of Computational and Applied Mathematics*, 27(1):279 – 297, 1989. Special Issue on Parallel Algorithms for Numerical Linear Algebra.

[84] Willi Schönauer, Karlheinz Raith, and Gerhard Glotz. The principle of the difference of difference quotients as a key to the self-adaptive solution of nonlinear partial differential equations. *Computer Methods in Applied Mechanics and Engineering*, 28(3):327 – 359, 1981.

[85] H. Shen, H. Toki, K. Oyamatsu, and K. Sumiyoshi. Relativistic equation of state of nuclear matter for supernova and neutron star. *Nucl. Phys.*, A637:435–450, 1998.

[86] Hector O. Silva, Jeremy Sakstein, Leonardo Gualtieri, Thomas P. Sotiriou, and Emanuele Berti. Spontaneous scalarization of black holes and compact stars from a gauss-bonnet coupling. *Phys. Rev. Lett.*, 120:131104, Mar 2018.

[87] Thomas P. Sotiriou and Shuang-Yong Zhou. Black hole hair in generalized scalar-tensor gravity. *Phys. Rev. Lett.*, 112:251102, 2014.

[88] Thomas P. Sotiriou and Shuang-Yong Zhou. Black hole hair in generalized scalar-tensor gravity: An explicit example. *Phys. Rev. D*, 90:124063, Dec 2014.

[89] Ingrid H. Stairs. Testing general relativity with pulsar timing. *Living Reviews in Relativity*, 6(1):5, 2003.

[90] Andrew Sullivan, Nicolás Yunes, and Thomas P. Sotiriou. Numerical black hole solutions in modified gravity theories: Spherical symmetry case. *Phys. Rev. D*, 101:044024, Feb 2020.

[91] Saul A. Teukolsky. Rotating black holes: Separable wave equations for gravitational and electromagnetic perturbations. *Phys. Rev. Lett.*, 29:1114–1118, Oct 1972.

[92] Takashi Torii, Hiroki Yajima, and Kei-ichi Maeda. Dilatonic black holes with a gauss-bonnet term. *Phys. Rev. D*, 55:739–753, Jan 1997.

[93] H. van der Vorst. Bi-cgstab: A fast and smoothly converging variant of bi-cg for the solution of nonsymmetric linear systems. *SIAM Journal on Scientific and Statistical Computing*, 13(2):631–644, 1992.

[94] Mikhail S. Volkov. Cosmological solutions with massive gravitons in the bigravity theory. *JHEP*, 01:035, 2012.

[95] Mikhail S. Volkov. Hairy black holes in the ghost-free bigravity theory. *Phys. Rev.*, D85:124043, 2012.

[96] Clifford M. Will. Bounding the mass of the graviton using gravitational-wave observations of inspiralling compact binaries. *Phys. Rev. D*, 57:2061–2068, Feb 1998.

[97] Clifford M. Will. The confrontation between general relativity and experiment. *Living Reviews in Relativity*, 17(1):4, Jun 2014.

[98] Helvi Witek, Leonardo Gualtieri, Paolo Pani, and Thomas P. Sotiriou. Black holes and binary mergers in scalar Gauss-Bonnet gravity: scalar field dynamics. 2018.

[99] Kent Yagi, Leo C. Stein, and Nicolás Yunes. Challenging the presence of scalar charge and dipolar radiation in binary pulsars. *Phys. Rev. D*, 93:024010, Jan 2016.

[100] Kent Yagi and Nicolas Yunes. I-Love-Q. *Science*, 341:365–368, 2013.

[101] Kent Yagi and Nicolas Yunes. I-Love-Q Relations in Neutron Stars and their Applications to Astrophysics, Gravitational Waves and Fundamental Physics. *Phys. Rev.*, D88(2):023009, 2013.

[102] Kent Yagi and Nicolas Yunes. Approximate Universal Relations among Tidal Parameters for Neutron Star Binaries. *Class. Quant. Grav.*, 34(1):015006, 2017.

[103] Nicolás Yunes and Xavier Siemens. Gravitational-wave tests of general relativity with ground-based detectors and pulsar-timing arrays. *Living Reviews in Relativity*, 16(1):9, Nov 2013.

[104] Nicolás Yunes and Leo C. Stein. Nonspinning black holes in alternative theories of gravity. *Phys. Rev. D*, 83:104002, May 2011.

[105] Aaron Zimmerman, Huan Yang, Zachary Mark, Yanbei Chen, and Luis Lehner. Quasinormal modes beyond kerr. In Carlos F. Sopuerta, editor, *Gravitational Wave Astrophysics*, pages 217–223, Cham, 2015. Springer International Publishing.

APPENDICES

APPENDIX A

SAMPLE FUNCTIONS

$$
\begin{aligned}
F_1 &= m^2 \cos^2\eta \left[c_3 U^2 - (3c_3+1)\, U\, r + 2r^2 \left(c_3 + \frac{3}{4} \right) \right], \\
&\quad \mathrm{x}\sqrt{\frac{U\,(r-2m_g)}{r\,(U-2m_f)}}, \\
F_2 &= 4r^2\pi\rho - \frac{3}{2} m^2 \cos^2\eta \Bigg[\left(\frac{5}{3} c_3 + 2 \right) r^2 - \left(\frac{8}{3} c_3 + 2 \right) U\, r, \\
&\quad + \left(c_3 + \frac{1}{3} \right) U^2 \Bigg], \\
F_3 &= -\frac{1}{2} m^2 \sin^2\eta \left[(U-r)\,(U-3r)\, c_3 + r^2 \right], \\
F_4 &= \frac{m^2 \sin^2\eta \left[c_3 U^2 - (3c_3+1)\, U\, r + 2r^2 \left(c_3 + \frac{3}{4} \right) \right]}{\sqrt{\frac{U(r-2m_g)}{r\left(U-2m_f\right)}}},
\end{aligned}
\tag{A.1}
$$

The remaining F_5, F_6, and F are available upon request.

APPENDIX B

NUMERICAL METHODS

We begin by outlining the Newton-Raphson method in the continuum limit in Sec. B. The discretization method takes our generic system of nonlinear differential equations and recasts them for evaluation on a discrete domain through a Newton polynomial scheme outlined in Sec. B. This method naturally introduces discretization errors that must be estimated which is outlined in Sec. B. Then these discretization errors must be controlled in a method outlined in Sec. B. Combining these results, we describe the application of the discrete Newton-Raphson method with a relaxation factor in Sec. B, which reduces the computational problem to solving a system of coupled linear equations through two iterative Krylov subspace methods, detailed in Sec. B.

Iterative Relaxation Method in the Continuum Limit

We start with a system of M, second-order, nonlinear elliptic partial differential equations. In the simplest 1-D (spherically symmetric and stationary) case, these equations are ordinary differential equations of some independent variable x, such that in operator form

$$\mathcal{D}\,\vec{u}^{\,*} = 0\,, \tag{B.1}$$

where $\mathcal{D}$ is an $M \times M$ matrix of nonlinear differential operators and $\vec{u}^{\,*}$ is the *solution vector*[1] with M elements. The elements of $\vec{u}$ are the fields in the problem, which we will sometimes denote with capital latin indices $\vec{u} = (u_0, u_1, \ldots, u_A, \ldots, u_{M-1})$. We see then that the special solution vector $\vec{u}^{\,*}$ is annihilated by the differential operator $\mathcal{D}$.

In general, however, one does not know the solution to the differential system, so a generic vector $\vec{U}$ will not be annihilated by $\mathcal{D}$. Rather, for a generic vector $\vec{U}$ that is not a solution to the differential system one has

$$\mathcal{D}\,\vec{U} = \vec{b}(\vec{U}), \tag{B.2}$$

where the *residual vector* $\vec{b}$ has M elements and is a function of $\vec{U}$. The generic vector $\vec{U}$ is a functional that spans the vector function space that contains the solution vector $\vec{u}^{\,*}$ and any other vector that does not satisfy the differential system $\vec{u}$[2]. Clearly then, once one finds the correct vector $\vec{U}$, namely $\vec{U} = \vec{u}^{\,*}$, then $\vec{b}(\vec{u}^{\,*}) = 0$.

The vector $\vec{U}$ is also subject to boundary conditions. We can express these in the form

$$\mathcal{B}\,\vec{U}|_{\partial V} = \vec{B}, \tag{B.3}$$

where $\mathcal{B}$ is another $M \times M$ matrix typically composed of a combination of real numbers and first-order differential operators, while ∂V is the boundary of the spatial domain.

[1] In this paper, the word *vector* stands for a standard Euclidean vector in flat space.

[2] In particle physics, the set of functions that satisfy a differential system of equations is sometimes referred to as "on shell," while those that do not are referred to as "off shell." Thus $\vec{U}$ spans the space that contains both on and off shell functions.

The *boundary vector* $\vec{B}$ also has M elements and is a set of constants defined on the boundary ∂V. Defining the boundary conditions in this way allows the imposition of Neumann boundary conditions for a subset of the components of $\vec{U}$ and Dirichlet boundary conditions for other components.

Let us assume that we have a vector $\vec{u}$ that we know is close the the actual solution vector $\vec{u}^*$. If so, the difference between it and the actual solution is some other small vector $\Delta\vec{u}$. Let us refer to the latter as the *correction vector*, which is mathematically defined via

$$\Delta\vec{u} := \vec{u}^* - \vec{u}. \tag{B.4}$$

We begin by linearizing $\vec{b}(\vec{U})$ around $\vec{U} = \vec{u}$ through a first-order Taylor expansion, analogous to the familiar Taylor expansion of $f(x)$ about $x = a$. Doing so, we find

$$\vec{b}(\vec{U}) \approx \vec{b}(\vec{u}) + \left.\frac{\partial\vec{b}}{\partial\vec{U}}\right|_{\vec{u}} \left(\vec{U} - \vec{u}\right). \tag{B.5}$$

We then evaluate this expression at the solution vector $\vec{U} = \vec{u}^*$ and obtain

$$\vec{b}(\vec{u}^*) \approx \vec{b}(\vec{u}) + \left.\frac{\partial\vec{b}}{\partial\vec{U}}\right|_{\vec{u}} (\vec{u}^* - \vec{u}). \tag{B.6}$$

Using that $\vec{b}(\vec{u}^*) = 0$ and substituting the correction vector defined in Eq. (B.4), this can be simplified to

$$\mathcal{J}\Delta\vec{u} \approx -\vec{b}(\vec{u}), \tag{B.7}$$

where we have defined the $M \times M$ Jacobian matrix

$$\mathcal{J} := \left.\frac{\partial\vec{b}}{\partial\vec{U}}\right|_{\vec{u}}. \tag{B.8}$$

We now wish to solve for the correction vector $\Delta\vec{u}$, which implies we must either invert the Jacobian or solve the linear system in Eq. (B.7). In practice, matrix inversion is typically more computationally expensive than linear system solving, so the latter is the method we use here, which we will explain in more detail in Sec. B. If one knew the correction vector $\Delta\vec{u}$ exactly, one could then find the solution vector from Eq. (B.4). But in reality the linearizaton in Eq. (B.5) implies the correction vector we find by solving Eq. (B.7) is only an approximation to the true correction vector. This implies that to find the true correction vector we must apply this procedure *iteratively*.

Let us then describe the first couple of iterations of this procedure. We start with an initial guess $\vec{u}^{(0)}$ that we know is close to the true solution, where the superscript in parenthesis is the iteration number. In this paper, the initial guess can be chosen to be either the GR solution, or an approximate solution for all fields in the modified

theory. With this initial guess, we then find the initial residual vector

$$\vec{b}^{(0)} = \mathcal{D}\vec{u}^{(0)}. \tag{B.9}$$

Since the initial guess is not a solution to the differential system, the residual vector does not vanish, and we must thus correct the initial guess to find the first-iterated solution

$$\vec{u}^{(1)} = \vec{u}^{(0)} + \Delta\vec{u}^{(0)}\,. \tag{B.10}$$

This requires the calculation of the zeroth-iterated correction vector $\Delta\vec{u}^{(0)}$, which we find by solving the linear system

$$\mathcal{J}^{(0)}\Delta\vec{u}^{(0)} = -\vec{b}(\vec{u}^{(0)})\,, \tag{B.11}$$

where the Jacobian is evaluated on the initial guess $\vec{u}^{(0)}$. This procedure then yields $\vec{u}^{(1)}$, and now it can be repeated until the n^{th}-iteration to the solution $\vec{u}^{(n)}$ is sufficiently close to $\vec{u}^*$, i.e. until the residual vector is below some specified tolerance, $\vec{b}(\vec{u}^{(n)}) < \mathrm{tol}$.

Discrete Representation through Newton's Polynomials

In order to numerically solve the differential system described above, one first needs to discretize it on a finite numerical grid. We here use Newton's (centrally divided difference) interpolation polynomial method, which we describe next.

Newton's interpolation polynomial provides a continuous local representation of a discrete function given by a set of data points. This procedure is a discrete analog of using a Taylor series to represent an approximation to a continuous function $f(x)$ as a local polynomial about some point $x = a$, namely

$$\begin{aligned} f(x) &= \sum_{n=0}^{\infty} \frac{f^{(n)}(a)}{n!}\,(x-a)^n\,, \\ &= f(a) + f'(a)\,(x-a) + \frac{1}{2}f''(a)\,(x-a)^2 + \ldots\,, \end{aligned} \tag{B.12}$$

where the primes denote derivatives with respect to the independent variable x.

Now imagine that instead of a continuous function $f(x)$, we have a discrete function $u_d(x)$ known only on a discrete collection of N data points $[(x_0, u_0), (x_1, u_1), \ldots, (x_i, u_i), \ldots, (x_{N-}$ Notice that the lower-case Latin subscript here does not denote the components of the $\vec{u}$ of the previous subsection, but rather the element x_i at which we evaluate the discrete function u_d. For notational convenience, we identify u_i with the discrete function $u_d(x)$ evaluated at each point x_i, namely

$$u_i = u_d(x_i). \tag{B.13}$$

How do we now approximate the discrete function u_d in a neighborhood of some

point in the spatial domain? We are tempted to use a Taylor expansion again, but because our function is discrete, we cannot take analytical derivatives as we did before, and instead we must use a finite difference approximation. Let us then define a neighborhood around some point x_I as the region in the discrete spatial domain around which we wish to approximate our function. Clearly then, the value of the function at the point x_I is simply $u_I = u_d(x_I)$. Let us further temporarily assume that the data points are equidistant, such that $\Delta x = x_{I+1} - x_I$.

We are now almost ready to define our finite difference approximation, but first we must choose which discrete points in the neighborhood of x_I we will use to approximate the function. For example, if we choose to use the points (x_I, x_{I+1}, x_{I+2}), then the Newton interpolation polynomial of our discrete function is

$$\begin{aligned} u_d(x) = u_I + \frac{u_{I+1} - u_I}{\Delta x}\,(x - x_I) \\ + \frac{u_{I+2} - 2u_{I+1} + u_I}{2\Delta x^2}\,(x - x_I)\,(x - x_{I+1})\,. \end{aligned} \tag{B.14}$$

The coefficients of the second and third terms in Eq. (B.14) are simply the first- and second-order forward finite difference approximation to the first and second derivative of the function in the $\Delta x \to 0$ limit, namely

$$\begin{aligned} u'_d(x_I) &\equiv \lim_{\Delta x \to 0} \frac{u_d(x_I + \Delta x) - u_d(x_I)}{\Delta x}, \\ &= \frac{u_d(x_I + \Delta x) - u_d(x_I)}{\Delta x} + \mathcal{O}(\Delta x). \end{aligned} \tag{B.15}$$

and

$$\begin{aligned} &u''_d(x_I) \equiv \\ &\lim_{\Delta x \to 0} \frac{u_d(x_I + 2\Delta x) - 2u_d(x_I + \Delta x) + u_d(x_I)}{\Delta x^2}, \\ &= \frac{u_d(x_I + 2\Delta x) - 2u_d(x_I + \Delta x) + u_d(x_I)}{\Delta x^2} \\ &+ \mathcal{O}(\Delta x), \end{aligned} \tag{B.16}$$

respectively. Moreover, using that

$$(x - x_I)(x - x_{I+1}) = (x - x_I)^2 - \Delta x\,(x - x_I)\,, \tag{B.17}$$

we notice that the $(x - x_I)^2$ term is the same polynomial that appears in the Taylor expansion, and that the additional Δx term cancels with one of the Δx^2 in the denominator of Eq. (B.14). We can then combine this with the first-order term to

obtain

$$\begin{aligned} &u'_d(x_I) = \\ &\frac{-u_d(x_I + 2\Delta x) + 2u_d(x_I + \Delta x) - 3u_d(x_I)}{2\Delta x} \\ &+ \mathcal{O}(\Delta x^2). \end{aligned} \tag{B.18}$$

Let us now compare the above result to the first-order finite difference derivative in Eq. (B.15). First, the derivative now includes three points instead of two. Second, the accuracy has been increased to $\mathcal{O}(\Delta x^2)$. This suggests that as we add increasingly higher-order polynomials to our discrete representation, they will automatically include corrections to each of the previous lower-order polynomials. Thus, the Newton interpolation polynomial is simply a discrete analog to the Taylor series, and they are formally equivalent in the continuous limit.

The full construction of the Newton interpolation polynomial requires certain Newton basis polynomials and certain divided differences coefficients, which are a generalization of the finite difference coefficients of the above simple example. The choice of points to include leads to the distinction between a forward and a backward divided difference, and this influences the directional finite difference that reduces to the Taylor derivative in the continuum limit. As a simple example, consider again the approximation of a discrete function u_d in a neighbourhood around a point x_I but this time using the points immediately surrounding x_I: (x_I, x_{I+1}, x_{I-1}). Equation (B.14) then becomes

$$\begin{aligned} u_d(x) = u_I + \frac{u_{I+1} - u_I}{\Delta x}(x - x_I) \\ + \frac{u_{I+1} - 2u_I + u_{I-1}}{2\Delta x^2}(x - x_I)(x - x_{I+1}), \end{aligned} \tag{B.19}$$

which results in the first and second-order *central* finite difference equations in the continuum limit. Similarly if we use the points before x_I only, namely (x_I, x_{I-1}, x_{I-2}), we then obtain the *backwards* finite difference equations in the continuum limit. The accuracy of the central finite difference equations is improved by a factor of $\mathcal{O}(\Delta x)$ over the forward or backwards finite differences.

Let us generalize the systematic application of these choices through the introduction of a *stencil*, namely a Euclidean vector s_j whose elements are the labels of the points included in the evaluation of our Newton polynomial. For example, for a forward, central, and backwards Newton polynomial representation of a discrete function about a point x_I, the stencil $s_j = (I, I+1, I+2), (I, I+1, I-1)$, and $(I, I-1, I-2)$ respectively.

With this at hand we can write the general Newton interpolation polynomial of

a discrete function u_d about any point x in the spatial domain as

$$u_d(x) = \sum_{j=0}^{r} \sum_{i=0}^{j} u_{s_i} \, w_{s_i,s_j} \, P_{s_j}(x), \tag{B.20}$$

where recall that u_{s_i} is given by Eq. (B.13) using stencil notation, and where

$$w_{s_i,s_j} = \frac{1}{\prod\limits_{\substack{p=0 \\ p \neq i}}^{j} \left(x_{s_i} - x_{s_p}\right)}, \tag{B.21}$$

and $P_{s_j}(x)$ are the Newton basis polynomials, defined by

$$P_{s_j}(x) = \prod_{q=0}^{j-1} \left(x - x_{s_q}\right). \tag{B.22}$$

If the grid is uniform and $\Delta x = x_{I+1} - x_I$, one can check that this equation reduces to Eqs. (B.14) or (B.19) with the respective stencil.

The index r in Eq. (B.20) is the order of the Newton polynomial and it indicates how many grid points are used and the maximum finite difference derivative order. In practice, as the order r increases, we successively add points to either side of x_I to keep the coefficients as central as possible, so our stencil has the form $s_j = (I, I+1, I-1, I+2, I-2, \ldots)$ and s_j will have $r+1$ elements. For even r the stencil will be purely central, whereas for odd r the stencil will be slightly forward. On the boundary of our domain, we must add points in a one-sided manner (either forward or backwards), and we must add an extra point beyond the number of points we keep away from the boundaries, to keep the accuracy of the represetation comparable to the central differences. Note that the specific sequence of the elements of s_j does not change the resulting polynomial.

As an example of an application of this, let us calculate and compare the Newton interpolation polynomial representation and the comparable Taylor series expansion of a toy function

$$u(x) = 1/x, \tag{B.23}$$

on a uniform discretized grid where $\Delta x = 0.1$ around the point $x_I = 2$. With a maximum order $r = 4$, the centralized stencil is $s_j = (I, I+1, I-1, I+2, I-2)$. Figure B.1 shows the Taylor series expansion and the Newton polynomial representation of our toy function order by order. The first three terms are shown in Eqs. (B.12) and (B.19), from which we see the $r = 0$ order approximation in both cases is simply a constant $u_d(2) = 1/2$. The $r = 1$ order is a line whose slope is calculated by either the derivative of the function evaluated at $x_I = 2$, or the first-order finite difference evaluated at $x_I = 2$. Observe that the agreement between

the Newton interpolation polynomial representation of the discrete function and the Taylor series expansion of the continuous function is very close but the agreement is better for even-orders of r than for odd-orders. This is a result of the even-orders of r being purely central for example for $r = 2, s_j = (I, I+1, I-1)$ while the odd-orders are slightly forward for example $r = 3, s_j = (I, I+1, I-1, I+2)$ which diminishes the accuracy. It is for this reason that we will restrict our choice in r to be even.

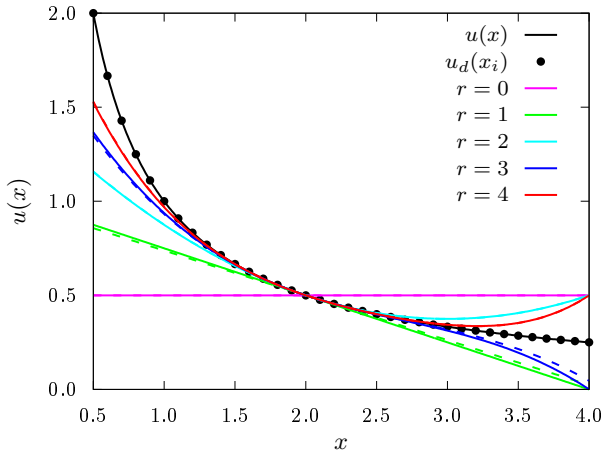

Figure B.1: (Color Online) Taylor series and Newton interpolation polynomial representation of the toy function $u(x) = 1/x$ around the point $x_I = 2$ on a uniform discretized grid order by order. The black solid line is the analytical function and the black dots are the discretized data points with $\Delta x = 0.1$. Solid lines indicate the Taylor series and dashed lines indicate the Newton polynomial, while the different colors indicate the polynomial order r. Observe the improved approximation for the even r orders compared to the odd-orders due to the slightly one-sided nature of the stencil for odd-orders.

Derivatives of Newton Polynomials and Discretization Error

One of the main advantages of using a Newton interpolation polynomial representation of a discrete function is that with it one can take *analytic* derivatives of the discrete function. For example, the derivatives $\partial_x u_d := du_d/dx$ can obtained by taking analytic derivatives of the basis functions P_j, which are the only x dependent terms in Eq. (B.20). The two relevant derivatives for second order equations are

$$\partial_x P_j(x) = \sum_{k=0}^{j-1} \prod_{\substack{i=0 \\ i \neq k}}^{j-1} (x - x_i)\,, \tag{B.24}$$

and

$$\partial_{xx} P_j(x) = \sum_{l=0}^{j-1} \sum_{\substack{k=0 \\ k\neq l}}^{j-1} \prod_{\substack{i=0 \\ i\neq k \\ i\neq l}}^{j-1} (x - x_i)\,, \tag{B.25}$$

as one can verify by direct differentiation.

This property of Newton interpolation polynomial representations allows us to replace the action of any differential operator on our fields at any grid point with a finite difference coefficient coupled to the r neighboring grid points, but this introduces some error. To quantify this error, let us introduce boldface vector notation to denote a *discretized vector*, i.e. the collection of data points of the Newton polynomial representation of a field evaluated on every point of the discretized grid. For example, for a given field $\boldsymbol{u}_d = [u_d(x_0), u_d(x_1), \ldots, u_d(x_N)]$. By construction, of course, the discretized field itself has no discretization error on any point of the discretized domain, but this is not the case for derivatives of the field. Let us then introduce the discretization error vector $\boldsymbol{e}_d$ and the discretization operator $\rightarrow$, such that

$$\begin{aligned} u &\rightarrow \boldsymbol{u}_d, \\ \partial_x u &\rightarrow \partial_x \boldsymbol{u}_d + \partial_x \boldsymbol{e}_d, \\ \partial_{xx} u &\rightarrow \partial_{xx} \boldsymbol{u}_d + \partial_{xx} \boldsymbol{e}_d, \end{aligned} \tag{B.26}$$

because by construction $\boldsymbol{e}_d(x_i) = 0$. These discretized errors will be incorporated into the Newton's method of Sec. B to maintain numerical accuracy.

Before moving on to the next subsection, let us here address some potential confusion due to the different choices of notation for a vector that we have employed. The boldface vector notation of the previous paragraph denotes a *discretized vector*, so its components are the values of the Newton polynomial representation of a function on each grid point of our spatial domain. The arrow vector notation of the previous section denotes a *generic field vector*, so its components are the different fields in the differential system. When we return to our general system of M differential equations, we must generate a Newton polynomial for each component of $\vec{u}$, and then, we must discretize each of these representations on N grid points. The quantity $\vec{\boldsymbol{u}}_d$ then becomes a 2-D matrix (see Eq. (B.27) below) with each element denoted as $u_{A,i}$.

As we will see later, we will have to *fold* every discretized vector in our system of equations so that we can take proper element by element partial derivatives. To do this, we introduce a new index $k = iN + A$ and fold the $\vec{\boldsymbol{u}}_d$ matrix into a single

vector where $k \in [0, (M-1)(N-1)]$, namely

$$\vec{u} = \begin{bmatrix} u_0 \\ \vdots \\ u_A \\ \vdots \\ u_{M-1} \end{bmatrix} \rightarrow \vec{\boldsymbol{u}}_d = \begin{bmatrix} \boldsymbol{u}_0 \\ \vdots \\ \boldsymbol{u}_A \\ \vdots \\ \boldsymbol{u}_{M-1} \end{bmatrix} = \begin{bmatrix} u_{0,0} & \dots & u_{0,i} & \dots & u_{0,N-1} \\ \vdots & & & & \\ u_{A,0} & \dots & u_{A,i} & \dots & u_{A,N-1} \\ \vdots & & & & \\ u_{M-1,0} & \dots & u_{M-1,i} & \dots & u_{M-1,N-1} \end{bmatrix},$$
$$= [u_{0,0}, \dots, u_{A,0}, \dots, u_{M-1,0}, \dots, u_{0,i}, \dots, u_{A,i}, \dots, u_{M-1,i}, \dots, u_{0,N-1}, \dots],$$
$$= \{u_k\}, \qquad k \in [0, (N-1)(M-1)]. \tag{B.27}$$

This folding replaces our system of M continuous differential equations with a linear system of $M \times N$ equations.

Minimization of the Discretization Error

Let us consider how the discretization error in the derivatives of the Newton polynomial representation of our discrete fields propagates into our system of M differential equations. For a generic vector $\vec{U}$, our discretized differential system becomes

$$\mathcal{D}\vec{U} = \vec{b}(\vec{U}) \rightarrow \boldsymbol{\mathcal{D}}\left(\vec{\boldsymbol{U}}_d + \vec{\boldsymbol{e}}_d\right) = \vec{\boldsymbol{b}}_d(\vec{\boldsymbol{U}}_d) + \tilde{\boldsymbol{\mathcal{D}}}\vec{\boldsymbol{e}}_d, \tag{B.28}$$

where $\tilde{\boldsymbol{\mathcal{D}}}$ is the linearized differential operator resulting from the expansion of $\mathcal{D}$. As before, let us choose our vector $\vec{u}$ to be close to the solution vector $\vec{u}^*$ up to a small correction vector $\Delta\vec{u}$. Discretizing these relations we then have that

$$\vec{u} = \vec{u}^* - \Delta\vec{u} \rightarrow \vec{\boldsymbol{u}}_d = \vec{\boldsymbol{u}}_d^* - \Delta\vec{\boldsymbol{u}}_d - \Delta\vec{\boldsymbol{u}}_e, \tag{B.29}$$

where we have included a new correction vector to attempt to also minimize the discretization error. As in Sec. B, we then Taylor expand Eq. (B.28) to find

$$\boldsymbol{\mathcal{J}}\left(\Delta\vec{\boldsymbol{u}}_d + \Delta\vec{\boldsymbol{u}}_e\right) = -\left(\vec{\boldsymbol{b}}_d + \vec{\boldsymbol{D}}_e\right), \tag{B.30}$$

where the discretized Jacobian is $\boldsymbol{\mathcal{J}} = \partial\vec{\boldsymbol{b}}_d/\partial\vec{\boldsymbol{u}}_d$ evaluated at $\vec{\boldsymbol{u}}_d$, and we have defined the *discretization error vector* $\vec{\boldsymbol{D}}_e \equiv \tilde{\boldsymbol{\mathcal{D}}}\vec{\boldsymbol{e}}_d$. The above equation can be satisfied by separately and simultaneously requiring that

$$\boldsymbol{\mathcal{J}}\Delta\vec{\boldsymbol{u}}_d = -\vec{\boldsymbol{b}}_d, \tag{B.31}$$

for the discretized correction vector $\Delta\vec{\boldsymbol{u}}_d$ and

$$\boldsymbol{\mathcal{J}}\Delta\vec{\boldsymbol{u}}_e = -\vec{\boldsymbol{D}}_e, \tag{B.32}$$

We recognize Eq. (B.31) as the discretized version of Eq. (B.7). By balancing both of these equations we can monitor the numerical accuracy of our discretization error.

The equation for the discretization error vector, Eq. (B.32), describes the change to our solution due to the discretized error vector $\vec{\boldsymbol{D}}_e$. To control the discretized error, we wish to require that the relative correction is below a specified tolerance. To solve Eq. (B.32), we first must calculate $\vec{\boldsymbol{D}}_e$ which was defined as the discretized differential operator acting on $\vec{\boldsymbol{e}}_d$:

$$\vec{\boldsymbol{D}}_e \equiv \tilde{\boldsymbol{\mathcal{D}}}\vec{\boldsymbol{e}}_d. \tag{B.33}$$

In practice, we will generally not have our system of nonlinear equations in operator form. For example, when calculating the Einstein field equations we will have the set of equations in the form of the residual vector $\vec{\boldsymbol{b}}(\vec{\boldsymbol{u}})$ as a functional of the fields themselves. If we wish to extract the linearized differential operator of Eq. (B.33) we must calculate it from the residual vector.

As a simple example, consider the following single continuous nonlinear differential equation in operator notation:

$$\mathcal{D}u = \left[\partial_{xx}u + (\partial_x u)^2\right]. \tag{B.34}$$

If we wish to calculate $u \to \vec{u}_d + \vec{e}_d$ we obtain,

$$\begin{aligned}\boldsymbol{\mathcal{D}}\left(\vec{u}_d + \vec{e}_d\right) = \partial_{xx}\vec{u}_d + \partial_{xx}\vec{e}_d + \left(\partial_x\vec{u}_d\right)^2 \\ +2\partial_x\vec{u}_d\partial_x\vec{e}_d + \left(\partial_x\vec{e}_d\right)^2.\end{aligned} \tag{B.35}$$

From this, we identify the linearized operator as

$$\tilde{\boldsymbol{\mathcal{D}}}\vec{e}_d = \partial_{xx}\vec{e}_d + 2\partial_x\vec{u}_d\partial_x\vec{e}_d, \tag{B.36}$$

and the general discretization error vector as

$$\vec{\boldsymbol{D}}_e = \frac{\partial\vec{\boldsymbol{b}}_d}{\partial\left(\partial_x\vec{\boldsymbol{u}}_d\right)}\partial_x\vec{\boldsymbol{e}}_d + \frac{\partial\vec{\boldsymbol{b}}_d}{\partial\left(\partial_{xx}\vec{\boldsymbol{u}}_d\right)}\partial_{xx}\vec{\boldsymbol{e}}_d, \tag{B.37}$$

where as before $\vec{\boldsymbol{e}}_d = 0$ due to the Newton polynomial construction.

The derivative error can then be computed from Eq. (B.26), namely via

$$\begin{aligned}\partial_x\vec{\boldsymbol{e}}_d &= \partial_x\vec{u} - \partial_x\vec{\boldsymbol{u}}_d, \\ \partial_{xx}\vec{\boldsymbol{e}}_d &= \partial_{xx}\vec{u} - \partial_{xx}\vec{\boldsymbol{u}}_d,\end{aligned} \tag{B.38}$$

but in general we do not know the analytical derivatives of any of the fields u. Following [83], we estimate the discrete derivative error from the difference between the discretized derivative at order r and that at order $r+2$. This is valid as long as the error decreases for increasing order, and if so, it provides a reasonable estimate

as demonstrated in [84]. With this approximation, our discretized derivative error is

$$\begin{aligned} \partial_x \vec{\boldsymbol{e}}_d &= \partial_x \vec{\boldsymbol{u}}_d^{(r+2)} - \partial_x \vec{\boldsymbol{u}}_d^{(r)}, \\ \partial_{xx} \vec{\boldsymbol{e}}_d &= \partial_{xx} \vec{\boldsymbol{u}}_d^{(r+2)} - \partial_{xx} \vec{\boldsymbol{u}}_d^{(r)}. \end{aligned} \tag{B.39}$$

Let us then describe the procedure we will follow to solve Eq. (B.30). First, before finding the field correction to the zeroth-iteration, we ensure the discretization error is under a specified tolerance by using Eq. (B.32) to determine the discretized grid size. This is achieved through a separate Newton-Raphson subroutine that we describe below. Once this is achieved, we then solve Eq. (B.31) to find the zeroth-iteration correction vector, which allows us to update the solution. This full procedure is then iterated, at each step ensuring that the discretization error is under control, until the residual in Eq. (B.31) is below a prescribed tolerance. We will detail this process in Sec. B.

Let us now describe the Newton-Raphson subroutine that we use to minimize the discretization error. First, we calculate $\vec{\boldsymbol{D}}_e$ from Eq. (B.37) using Eq. (B.39) for the discretization derivative error. We then find the correction to the solution $\Delta\vec{\boldsymbol{u}}_e$ by solving

$$\boldsymbol{\mathcal{J}} \Delta\vec{\boldsymbol{u}}_e = -\vec{\boldsymbol{D}}_e, \tag{B.40}$$

using one of the iterative methods in Sec. B. We stop the subroutine when the following condition is satisfied

$$\frac{\|\Delta\vec{\boldsymbol{u}}_e\|}{\|\vec{\boldsymbol{u}}_d\|} \leq \text{tol}, \tag{B.41}$$

where $\|\cdot\|$ is the maximum norm (also called infinity norm or supremum norm) among all fields and grid points. This condition forces the relative correction to the solution from the discretization error to be below some specified tolerance tol. In turn, this ensures that our final solution is within the discretized error tolerance.

If the above condition is not met for the chosen grid discretization, we adaptively adjust the grid step size until the relative discretization error correction is below the specified tolerance. To adjust the step size at each grid point i defined as Δx_i^{old}, we rescale the latter by the ratio of Eq. (B.41) with an additional "safety" factor of $1/3$, and relax the ratio by the Newton polynomial order r, such that

$$\Delta x_i^{\text{new}} = \left(\frac{\frac{1}{3} \|\vec{\boldsymbol{u}}_d\| \, \text{tol}}{|\Delta\vec{\boldsymbol{u}}_d|_i} \right)^{\frac{1}{r}} \Delta x_i^{\text{old}}, \tag{B.42}$$

where $|\cdot|_i$ is the maximum norm among all fields evaluated at grid index i.

Once the new step sizes are calculated, the entire grid must be adjusted and the condition in Eq. (B.41) must be rechecked. In the grid adjustment, we must ensure that the location of a new grid point remains within half an old step size of the old grid point. Then, each function is interpolated using the Newton polynomial representation calculated from the old grid point locations. From the new interpolated

solution, $\vec{\boldsymbol{D}}_e$ and $\Delta\vec{\boldsymbol{u}}_e$ are recalculated and the condition of Eq. (B.41) is rechecked. If the condition is not satisfied, the process using Eq. (B.42) is repeated until the step sizes on the grid become sufficiently small that the condition is satisfied. Once the discretization error is sufficiently under control we are ready to finally apply the Newton-Raphson iterations to the solution vector.

Minimization of the Residual Vector

As long as we can ensure our discretization error is under control, we can safely ignore their contributions to Eq. (B.30) and we are left with the equation

$$\boldsymbol{\mathcal{J}}\Delta\vec{\boldsymbol{u}}_d = -\vec{\boldsymbol{b}}_d\,, \tag{B.43}$$

which we can now solve following the same steps outlined in Sec. B.

The full algorithm is then as follows. Using the system at iteration n, $\vec{\boldsymbol{u}}_d^{(n)}$, we first find the discretized residual vector

$$\vec{\boldsymbol{b}}_d^{(n)} = \boldsymbol{\mathcal{D}}\vec{\boldsymbol{u}}_d^{(n)}, \tag{B.44}$$

and calculate the discretization error $\vec{\boldsymbol{D}}_d^{(n)}$. We then check Eq. (B.41) to determine if we need to adjust the step size according to Eq. (B.42). Once the step size is sufficient, we solve Eq. (B.43) for the correction vector $\Delta\vec{\boldsymbol{u}}_d^{(n)}$ and the generic vector is updated with a relaxation factor ω (initially $\omega = 1$) added

$$\vec{\boldsymbol{u}}_d^{(n+1)} = \vec{\boldsymbol{u}}_d^{(n)} + \omega\Delta\vec{\boldsymbol{u}}_d^{(n)}. \tag{B.45}$$

Before the new solution is accepted, the residual of the system is re-calculated to ensure convergence, i.e. that the new residual is smaller than the old residual:

$$\left\|\vec{\boldsymbol{b}}_d^{(n+1)}\right\| < \left\|\vec{\boldsymbol{b}}_d^{(n)}\right\|. \tag{B.46}$$

If the convergence condition of Eq. (B.46) does not hold then the relaxation factor is reduced by half,

$$\omega_{\text{new}} = \frac{1}{2}\omega_{\text{old}}, \tag{B.47}$$

and the new solution $\vec{\boldsymbol{u}}_d^{(n+1)}$ and residual $\vec{\boldsymbol{b}}_d^{(n+1)}$ is recalculated until Eq. (B.46) holds or until $\omega < 0.001$ at which point the algorithm terminates. If the convergence condition does hold then $\vec{\boldsymbol{u}}_d^{(n+1)}$ is accepted and the relaxation factor grows by,

$$\omega_{\text{new}} = \frac{3}{2}\omega_{\text{old}}. \tag{B.48}$$

Iterations are stopped when the maximum norm of the residual satisfies the condition,

$$\|\boldsymbol{b}_d\| < \text{tol} = 10^{-5}. \tag{B.49}$$

We analytically compute both the residual and the Jacobian from our set of field equations in the symbolic manipulation software `Maple 2018`, which are then automatically exported into the C programming language for evaluation by our algorithm. These are then used by an iterative linear solver described in the next section.

Linear System Solvers

The solution of linear systems of the form $\mathcal{A}\boldsymbol{x} = \boldsymbol{b}$ such as Eq. (B.43) is typically done by either direct or iterative methods. Direct methods find the solution through a finite number of steps. For example, LU decomposition uses gaussian elimination to decompose the matrix $\mathcal{A}$ into a product of lower and upper triangular matrices which simplifies the computation of the solution. Iterative methods, on the other hand, gradually approach the solution by recursively minimizing the estimated error between the current solution and the exact solution. For very large matrices, direct methods become unwieldy and can become computationally cumbersome so we use two iterative methods here.

The most common type of iterative method used today are Krylov subspace methods. These methods generate a sequence of approximate solutions from the Krylov subspace of $\mathcal{A}$ and the residual of the linear system defined as $\boldsymbol{r} = \boldsymbol{b} - \mathcal{A}\boldsymbol{x}$ such that the corresponding residuals converge to the zero vector. The two popular forms of this type of methods used here are the generalized minimal residual (GMRES) [80] and the biconjugate gradient stabilized (BiCGSTAB) [93] methods. The error tolerance of both iterative methods was chosen as $\mathrm{LS}_{\mathrm{tol}} = 10^{-12}$ which effectively places a lower bound on our numerical accuracy.

The GMRES method uses the Arnoldi method to create a Krylov subspace from the Gram-Schmidt process. The method then computes the upper triangular matrix representation of $\mathcal{A}$ in the Krylov basis. The solution is obtained from minimizing the norm of the residual of the system in this basis. BiCGSTAB is a modified variant of the conjugate gradient method which uses a method of gradient descent to find the minimum of the system of linear equations. BiCGSTAB is the generalized version of this method that applies to non-self-adjoint matrices and uses subroutine applications of GMRES to stabilize the conjugate gradient method.

APPENDIX C

SAMPLE FITTING COEFFICIENTS FOR SPHERICALLY SYMMETRIC SOLUTIONS

Here are a few fitting coefficients of Eq. (3.49). The full tables are available in `Mathematica`[1].

Table C.1: Fitting Coefficients for $a_{i,j}$

i	j	sGB	EdGB
0	2	0.0	$-4.082\,03 \times 10^{-4}$
1	2	0.0	$5.978\,31 \times 10^{-3}$
3	2	0.0	$-2.843\,05 \times 10^{-2}$
⋮	⋮	⋮	⋮
0	3	0.0	9.2781×10^{1}
⋮	⋮	⋮	⋮
0	4	-2.9618×10^{1}	$-7.973\,13 \times 10^{4}$
1	4	$6.006\,22 \times 10^{2}$	$6.276\,46 \times 10^{5}$
3	4	$6.345\,09 \times 10^{3}$	$-1.473\,52 \times 10^{6}$
⋮	⋮	⋮	⋮
0	6	$1.621\,76 \times 10^{6}$	$2.266\,74 \times 10^{10}$
⋮	⋮	⋮	⋮
13	12	$3.701\,17 \times 10^{17}$	$8.550\,71 \times 10^{21}$

[1]Source code and fitting coefficient `Mathematica` notebook are available at `https://github.com/sullivanandrew/XODES.git`

Table C.2: Fitting Coefficients for $b_{i,j}$

i	j	sGB	EdGB
0	2	0.0	$-3.258\,25 \times 10^{-1}$
1	2	0.0	$-2.534\,88 \times 10^{1}$
⋮	⋮	⋮	⋮
0	3	0.0	$-8.776\,88 \times 10^{2}$
⋮	⋮	⋮	⋮
0	4	$-3.963\,46 \times 10^{8}$	$-4.454\,46 \times 10^{5}$
1	4	$2.469\,21 \times 10^{4}$	$-3.759\,43 \times 10^{7}$
⋮	⋮	⋮	⋮
0	6	$1.447\,75 \times 10^{9}$	$1.020\,22 \times 10^{10}$
⋮	⋮	⋮	⋮
11	10	$2.165\,53 \times 10^{19}$	$-1.237\,41 \times 10^{21}$
⋮	⋮	⋮	⋮
11	12	$-1.980\,32 \times 10^{23}$	0.0

Table C.3: Fitting Coefficients for $c_{i,j}$

i	j	sGB	EdGB
0	1	0.0	$-3.198\,73 \times 10^{-4}$
1	1	0.0	$6.333\,99 \times 10^{-3}$
⋮	⋮	⋮	⋮
0	2	0.0	$4.317\,69 \times 10^{1}$
⋮	⋮	⋮	⋮
0	3	$1.209\,72 \times 10^{2}$	$-3.063\,23 \times 10^{1}$
1	3	$2.929\,29 \times 10^{1}$	$1.020\,85 \times 10^{4}$
⋮	⋮	⋮	⋮
0	5	$6.399\,37 \times 10^{5}$	$-3.763\,57 \times 10^{7}$
⋮	⋮	⋮	⋮
12	8	0.0	$3.029\,82 \times 10^{17}$
⋮	⋮	⋮	⋮
7	11	$-5.000\,65 \times 10^{18}$	0.0

APPENDIX D

SAMPLE FITTING COEFFICIENTS FOR AXIALLY SYMMETRIC SOLUTIONS

Here are a few fitting coefficients of Eq. (4.51). The full tables are available in `Mathematica`[1].

Table D.1: Fitting Coefficients for $a_{i,j}$

i	j	sGB	EdGB
0	0	$2.132\,61 \times 10^{-3}$	$1.625\,56 \times 10^{-3}$
⋮	⋮	⋮	⋮
12	0	$5.179\,226 \times 10^{1}$	$4.936\,694 \times 10^{1}$
⋮	⋮	⋮	⋮
0	6	$5.260\,29 \times 10^{-3}$	$1.623\,36 \times 10^{-3}$
0	7	$7.140\,71 \times 10^{-4}$	0.0
⋮	⋮	⋮	⋮
12	6	$2.459\,461\,3 \times 10^{2}$	$9.471\,161 \times 10^{1}$
12	7	$5.367\,143 \times 10^{1}$	0.0

[1]Source code and fitting coefficient `Mathematica` notebook are available at `https://github.com/sullivanandrew/XPDES.git`